POSITRON EMISION TOMOGRAPHY (PET) IN NON-MALIGNANT CHEST DISEASES

Shamsuddeen Ahmad Aliyu (MBBS, MSc.)

PhD Thesis

OCTOBER 27, 2019

THE UNIVERSITY OF HULL AND THE UNIVERSITY OF YORK
HULL YORK MEDICAL SCHOOL

Abstract

Molecular imaging is a functional imaging that identify disease in its earliest stages and determine the exact location of metabolically active tissue such as tumours. Often before symptoms occur or abnormalities can be detected with other diagnostic tests. Two simultaneous studies to explore the potentials of Positron Emission tomography (PET) have been conducted. In the first study, the role of PET in pulmonary drug deposition has been evaluated whereas in the second study, it's potential in monitoring disease progression and treatment response monitoring in IPF has been discovered.

Gamma imaging such as planer and Single Photon Emission computed tomography (SPECT) have been used for decades in the imaging of pulmonary drug deposition, despite numerous advantage of PET very few studies were found in the literature. Two studies were conducted using in-house developed lung surrogate phantom and Andersen cascade impactor to demonstrate PET role in pulmonary drug deposition. The lung surrogate phantom study is a ''proof of concept'' in which series of experiments was conducted leading to the development of a usable model. Each experimental procedure was conducted repeatedly over time to reduce the level of experimental errors. To my knowledge, this is the first phantom experiment quantifying the deposition pattern of aerosolized [18F]-FDG while mimicking human tidal breathing. In a separate experiment the Andersen cascade impactor (ACI) have been used to measure distribution of beclometasone dipropionate (BDP), formoterol fumarate dihydrate (FFA) as well as [18F]-2-fluorp-2-deoxy-D-glucose ([18F]-FDG) along the stages of ACI.

The overall activity deposition within the phantom; cylinder and the extra-pulmonary section of the tube were 8.07 ± 3.51MBq. The deposition within the cylinder (lung surrogate) was 6.27 ± 2.55MBq. The average total internal dose (phantom cylinders and the extra-pulmonary section of the tube was calculated to be 0.2mSv/PET scan. These results are expected in human clinical trial under similar experimental conditions.

The Aerodynamic particle size distribution (APSD) along the fractionating part of the AIM comprises of large particle mass (LPM) and small particle mass (SPM). The LPM is APSD >5µg deposited on stage 1 (representing to upper respiratory tract), whereas, the SPM comprised of the particle size 1-5 µg and < 1 µg deposited on stage 2 (representing the small airways and lung parenchyma) and an exhalation filter. In general, the deposition of the drugs and [18F]-FDG within the fractionating part of the impactor was predominantly within 1-5µg, which is a desirable fine particle fraction (FPF) of the active pharmaceutical ingredients (API) leading to pulmonary deposition.

The potentials of PET imaging in pulmonary drug deposition has been demonstrated in these experiments using lung surrogate phantom and cascade impactor. [18F]-FDG PET imaging has the potentials in providing better understanding of regional distribution of pulmonary drug deposition. Standardization of these methods will enable PET imaging to be used in pulmonary drug development.

In the second study, A retrospective studies using PET data was carried out to measure uptake of [18F]-FDG in the region of apparently normal lung in IPF. This was compared to normal control lung images to ascertain differences in their uptake value.

HRCT is the current gold standard imaging the diagnosis of IPF. Recently there is growing interest in exploring the potentials of PET imaging in the disease progression and treatment response monitoring in IPF.

Patients with IPF that had undergone PET-CT imaging for investigation of concomitant cancer diagnosis were identified retrospectively in a single interstitial lung disease (ILD) tertiary referral centre. Non IPF patients that had a PET-CT scan in the same centre for cancer diagnosis without non-malignant lung disease were identified to form two control groups: a lung cancer control group and a control group with no evidence of intra-thoracic disease (extra-thoracic malignancy controls). These two control groups were identified to allow assessment of whether the presence of thoracic malignancy

effected [18F]-FDG uptake. In the event of no effect being identified, a pooled analysis comparing IPF patients and all controls was planned.

No difference in standard uptake value (SUV) Maximum (Max) and SUV mean uptake was observed in the mean of 4 (Region of Interest) ROIs between lung cancer controls and extra-thoracic malignancy controls in all 3 normalizations (SUV Max body weight (BW), SUV body surface area (BSA) and SUV activity concentration (AC)) and therefore data from these groups were pooled for comparison with IPF patients. The SUV Max and SUV mean of radiologically normal lung in IPF patients was significantly higher than the normal lung in controls. However, the CT number/Hounsfield unit of the IPF patients and the control group are comparable. In addition, 20 textural features were identified in each ROI both in CT and PET data sets. Five out of the twenty CT textural features shows significant differences between the 2 controls as such, they were excluded. Fifteen were pooled together for comparison with IPF patients. Five out of the fifteen CT textural features shows significant differences when compared with IPF and all are consistent with five features that shows significant difference in PET dataset.

Increase [18F]-FDG PET signal within areas of areas of apparently normal lung parenchyma has been demonstrated using SUV with 3 different normalization methods as well as using textural feature analysis. These findings have shown the heterogeneous nature of the disease process indicating the possibility of the disease activity within the apparently normal lung CT lung images. These finding may provide insight into the pathogenesis of the disease and may be helpful in monitoring the disease progression and treatment response.

Acknowledgements

Firstly, I would like to express my sincere gratitude to my Supervisor Professor Alyn H. Morice for the continuous support throughout my PhD program. I thank him dearly for his patience, motivation and the partial sponsorship of this program. His guidance helped me in all the time of research and writing of this thesis. I could not have hoped for having a better advisor and mentor.

Besides my Supervisor, I would like to thank the rest of my thesis advisory panel: Professor Steve J. Archibald, Dr Simon Hart and Dr Chris Carthorne for their insightful comments and encouragement.

My sincere thanks also go to Dr Ged Avery, Dr Juozas Domarkas and Glenn Woolley for their technical support through my entire PhD research. Without their precious support, it would not have been possible to conduct this research. This is not complete without thanking the secretaries of the Centre for Cardiovascular and Metabolic Research of the Hull York Medical School and the entire staffs of The Jack Brignall PET-CT Centre Castle Hill Hospital for their incredible supports.

I will also like to thank my employer, Usmanu Dan Fodiyo University, Sokoto for the Academic fellowship to pursue this PhD program.

Last but not least, I would also like to thank my entire family and friends for their incredible support throughout this journey.

Contents

List of Abbreviations

ACI-Anderson Cascade Impactor

AIM-Abbreviated Impactor Measurement

APSD-aerodynamic particle size distribution

AC-Activity Concentration

API-Active Pharmaceutical Ingredient

BW-Body Weight

BSA-Body Surface Area

BDx- Mirada imaging software

Bq-Bacqrrel

BDP-Beclomethasone Dipropionate

CT- Computed Tomography

CECT- Contrast-Enhanced Computed Tomography

CPS- Count Per Second

CBM-Continuous Bed Motion

CPM-Coarse Particle Mass

CIs-Cascade impactor

GLUT-1-D-glucose transporter-1

DPIs-Dry Powder Inhalers

EPM-Extra-fine Particle Mass

FPM-Fine Particle Mass

FFD-Formoterol Fumarate Dihydrate

FOS-First Order Statistics

GLUT- Glucose Transport Proteins

GS- Gamma Scintigraphy

HRCT- High Resolution Computed Tomography

HU-Hounsfield Units

HPLC- High-Performance Liquid Chromatography

IIPs- Idiopathic Interstitial Pneumonias

ILD- Interstitial Lung Diseases

IPF- Idiopathic Pulmonary Fibrosis

IPAC-RS-International Pharmaceutical Aerosol Consortium on Regulation and Science

LoG-Laplacian of Gaussian

LPM- Large Particle Mass

MDIs- Metered dose inhalers

MRI-Magnetic resonance imaging

MSLI-Multi-Stage Liquid Impinger

MIP-Maximum Intensity Projection

MMAD-Mass Median Aerodynamic Diameter

MBP-Mediastinal Blood Pool

NGI-Next generation impactor

OIPs.-Orally Inhaled Products

OSEM-Ordered-Subsets Expectation Maximization

PET-Positron Emission Tomography

pMDI-Pressurized Metered Dose Inhaler

PPE- Personal Protective Equipment

PDA- Photo Diode Array

QC- Quality Control

RI-SUV -Standardized uptake value Retention index

ROI-Region of interest

SNR-Signal-to-noise Ratio

SPECT-single Photon Emission Computed Tomography

SFTPC- Mutation in Surfactant protein C

SFTPA2- Mutation in Surfactant protein A2

SUV-Standardized uptake value Retention index

SPM-Small Particle Mass

TGFβ1-Transforming Growth Factor β1

α-SMA -Smooth Muscle α-Actin

[18F]-FDG-18F-2-fluoro-2-deoxy-D-glucose

18F-FBEM-18F-4-fluorobenzamido-N-ethylamino-maleimide

[18F]-FTHA -18F-thia-fatty acids

List of Figures

List of Tables

Author's Declaration

I confirm that this work is original and that if any passage(s) or diagram(s) have been copied from academic papers, books, the internet, or any other sources these are clearly identified by the use of quotations marks and the reference(s) is fully cited. I certify that, other than where indicated, this is my own work and does not breach the regulations of HYMS, the University of Hull or the University of York regarding plagiarism or academic conduct in examinations. I have read the HYMS Code of Practice on Academic Misconduct, and state that this piece of work is my own and does not contains any unacknowledged work from any other sources. I confirm that any patient information obtained in the production of this piece of work has been appropriately anonymised.

Chapter 1 General Introduction

1.1 Lungs anatomy and physiology

The human respiratory system displays several level of complexity: the bronchial tree has a fractal structure with various degrees of self-similarity and the airflow dynamics inside exhibits chaos during rhythmic breathing [1]. Breathing is maintained and controlled by a network of neurons in the brainstem that generate respiratory rhythm while receiving regulatory inputs [2, 3]. There is a strong argument suggesting that the complexity of airflow in humans is an intrinsic property of central respiratory generators. In addition, both respiratory rhythm and airflow control have common genetic determinants [4]. However, the breathing is modulated by the state of the airways [5], by the chest wall [6], the lung, by chemical afferents sensitive to hypercapnia, hypoxia or acidosis [3] and by mechanical afferents from the airway, lung, chest wall, respiratory muscles as well as by supra-pontine commands. A previous study has shown that the structural and mechanical properties of the bronchial tree, lung and chest wall in humans are not sufficient to generate chaotic airflow in the absence of a central neural drive [7]. Nevertheless, it is still unclear in humans to what extent the complex dynamics of the respiratory centre contributes to airflow complexity.

Transportation of oxygen from the atmosphere to the body tissues and the release and transport of carbon dioxide from the body to the atmosphere are the main function of the human respiratory system [8, 9]. Other physiological functions such as; neural control, mechanics and non-respiratory functions are paramount to maintain normal body functions [10]. These functions are not carried out by the lung in isolation, however, the cardiovascular system plays a significant role in accomplishing the tasks [11]. Gas-exchange system that allows the uptake of oxygen from the atmosphere and the release of carbon dioxide to the atmosphere is carried out in the lungs whereas, transport of oxygen from the lungs to the body tissues and carbon dioxide from the body to the lung is carried out by the cardiovascular system [8, 9].

The respiratory system can be divided into upper respiratory tract (Nasal, oral cavities, pharynx, larynx, and trachea) and lower respiratory tract (bronchus and lung) [9, 12]. The function of the upper respiratory tract is to warm, moisture and filter the air making it suitable for exchange process [13].

The gas-exchange occurs within the lung which acts as a conduit for airflow (airways) and a surface for movement of oxygen into the blood and carbon dioxide out of the blood (alveolar-capillary membrane) [14]. The lung consists of airways, blood vessels, nerves and lymphatics. Surrounded and supported by parenchymal tissues [9].

The trachea divided into two left and right main bronchus within the thoracic cage. The two main bronchi divided into smaller units up to 23 generations until they reach the smallest airways units called the acini [8, 9, 15].

The gaseous exchange occurs within the acini which allowed the passage of oxygen from the lung to the blood and carbon dioxide from the blood to the lung [15, 16]. The gaseous exchange involved three key components; ventilation, perfusion and diffusion. These three processes prevent tissue hypoxia by optimizing the oxygen content of the arterial blood [9].

Ventilation is the movement of air in and out of the lung; determine by the respiratory rate and the volume of each breath (tidal breathing). The normal adult respiratory rate is 12-20 breath per minute with an average tidal volume of 500 mL. The body metabolic demands detect the change in ventilation which comes about either by altering the number of breath per minutes or by adjusting the amount of air entering the lungs per breath [8].

1.1.1 Ventilation-perfusion

Fresh gas and venous blood are delivered to and removed from the lung through the airway and vascular trees. The movement of air in and out of the lungs is due to differences between internal lung pressure and atmospheric pressures, as a result of the change in lung volumes [8, 14]. Lung expansion allows the air flow to the lung (high-pressure area) from the surrounding (low-pressure area), this act lowers the pressure within the lungs [8].

The two lungs sit on the diaphragm which is the main muscle of inspiration, the diaphragm is a dome-shaped muscle in a relaxing position, contacting the

diaphragm flattened the dome making the intrathoracic volume to increase [17]. The process of inspiration is supported by external intercostal muscles, which help by raising the ribcage. Accessory muscles also aided the process of ventilation in the case of increasing workload due to lungs and chest diseases [13].

Expiration is mainly passive due to recoil of the lung tissues, however, during force expiration such as during coughing, abdominal muscles participate by increasing intra-abdominal pressure pushing abdominal contents against the diaphragm forcing it to assume its' dome-shape [18].

The pulmonary trunk bifurcate given rise to left and right main pulmonary arteries which subsequently divides repeatedly into arterioles and capillaries that covers 85-95% of the alveolar surface [14].

The gas and blood compartment are separated by a thin alveolar membrane (1μm) allowing O2 and CO2 to diffuse rapidly between them. As a result of the large volume of blood within the capillaries, the flow of blood lowers to increase transit time allowing more time gaseous exchange [19, 20].

1.1.2 Diffusion

The transport of oxygen (O_2) and carbon dioxide (CO_2) across the blood-gas barrier occurs by simple diffusion [20]. During the gaseous exchange, oxygen and carbon dioxide molecules diffuse across the alveolar membrane along their partial pressure gradients. Oxygen accounts for 21% of the air in the atmosphere and therefore has 21% partial pressure measured in mmHg or kPa (PO2) [20]. The O_2 get moisturised along the upper respiratory tract, the O_2 in a liquid form diffused into the bloodstream at the alveolar-capillary membrane. Subsequently, the O_2 in combination with haemoglobin is transported to the heart via pulmonary veins [19].

1.2 Evaluation of Chest Imaging

Chest radiograph is the oldest and the most widely requested imaging technique in chest diseases [21, 22]. Over the years radiography has evolved significantly from film-screen radiography to digital radiography making it faster, more qualitative and eliminate the need for X-ray film storage and

repeat imaging [21, 23]. Despite the advancement in technology, the chest radiograph is not sensitive and specific in diagnosing some chest diseases such as detecting lung nodules in suspected lung cancer patients or diagnosing pulmonary interstitial lung diseases [21, 24]. There is a need for great accuracy in the interpretation of the Chest radiograph, which can be achieved by ensuring the quality of the radiograph patients' position, patients' respiration and correct film exposure.

Computed Tomography (CT) is the second most important imaging modality of the chest, it is more sensitive and specific than chest radiograph. Although it can be requested in the event of normal chest radiograph but mostly requested following inconclusive chest radiograph [21, 22, 24, 25]. Depending on the circumstances, different techniques of chest CT can be requested, Such as; High resolution computed tomography (HRCT), contrast-enhanced CT (CECT) or unenhanced CT [26, 27].

High resolution-CT (HRCT) or thin-section is a special acquisition technique that used 0.5-1-mm slice thickness and high-frequency reconstruction algorithms to produce highly detailed images [21, 28]. It is mostly used when lung parenchymal is required, such as in diffused parenchymal lung diseases. Although the downside of the HRCT is increasing the radiation dose to the patients. Lung parenchyma is very suitable for radiation dose reduction without significant reduction of image quality. As such, the used of low-dose CT in establishing lung diseases is yielding magnificent results.

Although CT is diagnostic in many lung diseases additional clinical and pathological information is highly needed in some other diseases[28]. Clinical information is ultimately needed in order to distinguish idiopathic pulmonary fibrosis (IPF) from other idiopathic interstitial pneumonias (IIPs) [29, 30]. In case of suspected lung cancer, surgical or image-guided lung biopsy is highly needed.

Nuclear Imaging play significant role in lung imaging such as; cancer imaging, and ventilation perfusion imaging and imaging of pulmonary drug deposition [31-36]. For decades, gamma scintigraphy played a measure role in imaging pulmonary drug deposition where is Positron Emission

Tomography is mostly used for staging lung cancer [37-39]. Total and regional respiratory tract deposition of pulmonary drug can be assessed in vivo by adding γ-emitting radionuclide to the drug formulation under analysis [40]. With 2D gamma imaging and SPECT the radiotracer is usually only physically associated with the drug, rather than chemically bound to it [40]. Therefore, after the deposition, the radiotracer may disassociate from the drug and cannot be used to track the deposition of the drug. However, this can be overcome by incorporation of a radiotracer directly into the drug molecule. By radiolabelling the drug with positron emitters such as 18fluorine it is possible to generate three-dimensional images of the drug in the lung using positron emission tomography (PET) scanning, which has a higher resolution and is more accurate than SPECT [35]. PET imaging provides improved image quality, greater interpretive certainty, higher diagnostic accuracy, lower patient dosimetry, and shorter imaging protocols as compared to SPECT and planer imaging [41, 42]. The lung surrogate phantom was the first of its kind as per as I know, as such, no literature was found to support our experiment. However, the sponges used was recommended by the commercial sponge manufacture (via phone call conversation) and was also used in ventilation/perfusion study by another group [43].

Chapter 2 Literature review

2.1 Macro- and Microstructure of the Airways for Drug Delivery

Understanding the anatomy and physiology of the airways are paramount in predicting the dynamics of the drug delivery system and the pattern of deposition of the orally inhaled products (OIPs).

The conducting airways composed of the upper portion of the airways, the airways bifurcate repeatedly up to about 17 times reaching deeper into the lung. This bifurcation provides increase surface area and reducing the air velocity [44]. No gaseous exchange happen within the conducting airways, the primary purpose is to moisture and transport to the respiratory zone. Other functions include humidifying and warming the air to ensure the air is identical to the pre-existing internal environment of the lung [45, 46]. Cold air and improper humidification of air may lead to dehydration and body weight loss, on the other hand, over humidification will lead to water intoxication (). In general, to ensure the efficiency of drug delivery, proper function of the conducting system needs to be maintained [45, 47].

The respiratory airways begin distal to terminal bronchioles of the conducting airways and consist of respiratory bronchioles, alveolar ducts and alveolar sack (). The main function of respiratory airways is the gaseous exchange [13]. Due to the large surface area (10^2 m^2), the thin layer of the epithelial lining (0.1–0.4-mm), as well as the tiny fluid layer at the cell surface (70 nm), makes respiratory airways suitable for this functions [48, 49]. The partial pressure of O2 within the alveolar is less than the partial pressure of CO2 rich blood within the pulmonary circulation. This pressure gradient and the characteristic of the alveolar membrane allowed oxygen to diffuse from alveolar into the blood and the carbon dioxide in the other direction [46, 50].

2.2 Aerosol Particle Deposition Mechanisms

The factors responsible for pulmonary drug deposition within the respiratory system can be divided into; the anatomy and physiology of the respiratory system, method of inhalation, particle characteristics as well as the delivery

system. Generally, there are 3 main accepted mechanisms for particle deposition within the respiratory system which includes; impaction, sedimentation, and diffusion [51, 52]. Particle size, density, and velocity influence the site of particle impaction within the respiratory system whereas, the particle mass influence sedimentation and gravitational force of the particle within the respiratory system [53].

2.3 Assessment of Pulmonary Drug Deposition

The quantification of lung deposition or lung dose of inhaled medicines is essential in establishing the effectiveness of the medication. The accuracy of the quantification method is critical for the development of new drugs and their delivery systems [34, 54, 55]. *Ex vitro*, *in vitro* as well as *in vive* methodologies for the assessment of pulmonary drug deposition exist [56]. As with nearly all measurement techniques, each of these has its advantages and disadvantages.

2.3.1 *In Vitro/Ex vivo* Performance Testing for Pulmonary Drug Delivery

Cascade impactor (CIs) is used as a lung surrogate device and is the mainstay *in vitro* device for the measurement of inhaler aerosol aerodynamic particle size distribution (APSD) (Fig 1). The CI operate based on the principle of inertial impaction [57, 58]. Multistage Andersen cascade impactor is used in pulmonary drug development and subsequent quality control (QC) of the products to understand the particle dispersion along the respiratory tract [59]. A pump generating air flow at fix flow rate is used to draw an aerosol through the orifices with a collecting plate place below the orifices at the right angle to the direction of flow (Fig 1, 2 and 3). The large particles with enough inertia will continue their journey along the original path and impact on the plate while the small particles with low inertia will stay within the air streamlines to the next stage until the last stage of the impactor [53, 60].

The particles sizes collected on each plate are successively smaller than the previous plates with the smallest particle sizes collected on the filter which follows the final stage of the impactor. Due to the decreasing size of the orifices in the succeeding stages of the CI, the linear velocity of the airstream increases in each successive stage of the impactor [61].

The operation standard of the CI depends on a number of geometric and operational factors including; linear velocity of the air flow; the aerosol particle shape; the particle size; the particle density and viscosity [58].

The practicality of this method is labour-intensive and require high degree of manual skills in order to achieve accurate results in comparison to human pulmonary distribution. A comprehensive guide for actualizing high accuracy in the performance of CI operation has been developed [62, 63]. Some of the factors to be considered are as follows;

a) Right collection solvent

b) Use of collection surface coating on the impactor plates to reduce particle bouncing

c) Adequate washing of the plates after use

d) Appropriate Environmental factors (barometric pressure, temperature, relative humidity).

e) Use of a backup filter

Abbreviated Impactor Measurement (AIM) has been developed to reduce the tedious nature of the operation and to reduce the results variability [62-64]. Other *in vitro* devices include; Next generation impactor (NGI) and Multi-Stage Liquid Impinger (MSLI) [65-67].

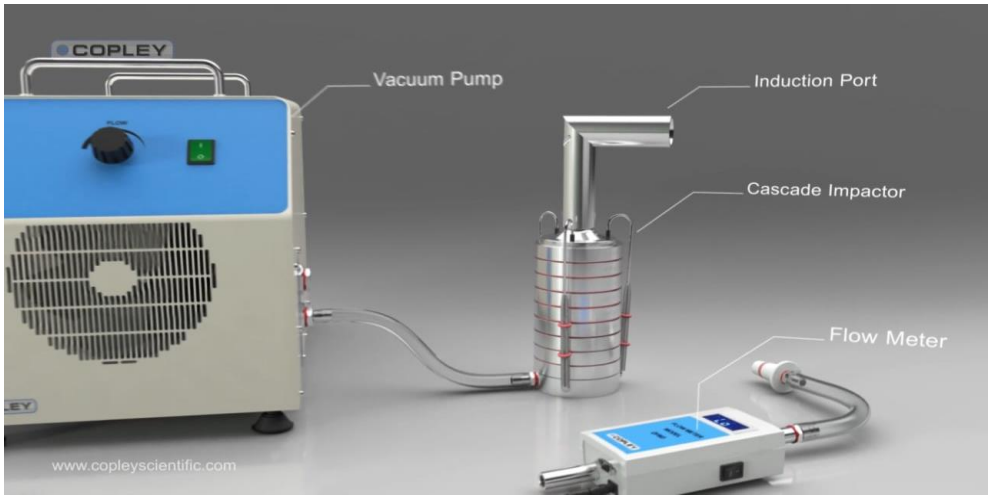

Fig 1: Multistage Anderson cascade impactor (Images obtained from Copley scientific)

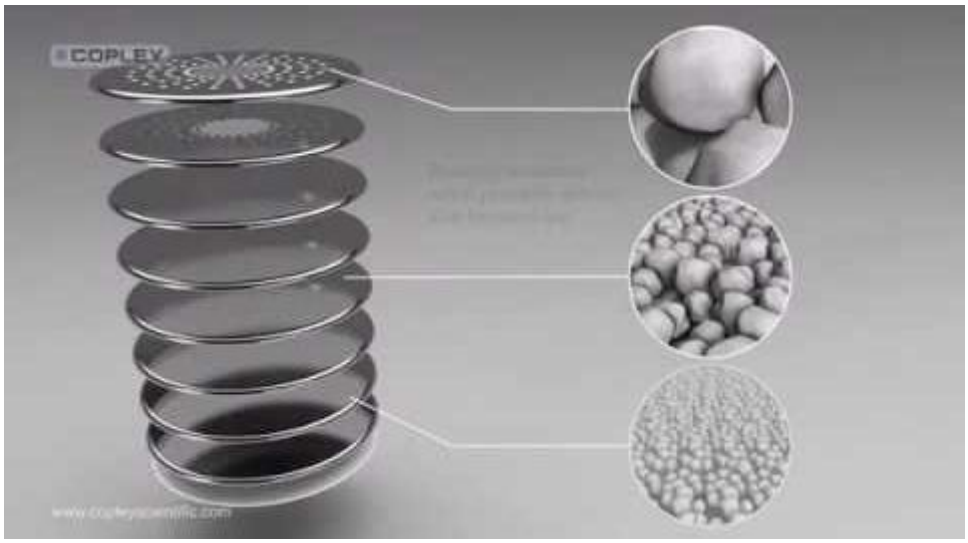

Fig 2: ACI plates placed beneath each stage of the impactor, each plate collect particles from the previous stage, the particle sizes collected on the plates reduces in descending order with respirable particles (< 1µm) impacting of the filter at the bottom of the impactor (Images obtained from Copley scientific).

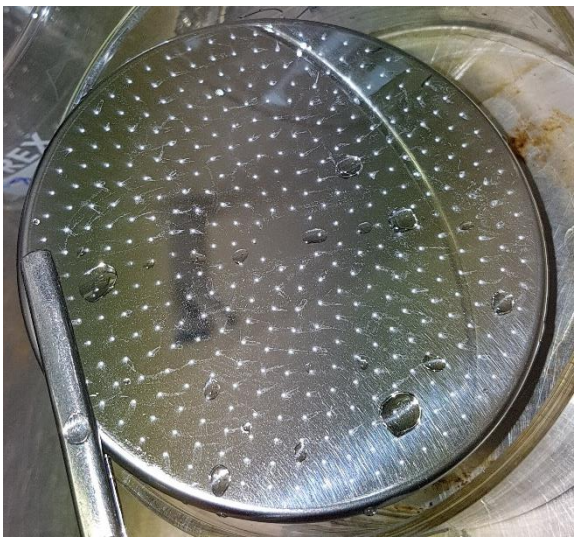

Fig 3: Anderson cascade impactor aerosols collecting plate, the aerosol particles with enough inertia impacted on the plate, while the rest of the particles continue their motion in the direction of flow.

Several *in vitro* respiratory epithelial models such as Primary Cell Cultures the of Tracheobronchial Epithelia; Primary Cell Cultures of Alveolar

Epithelia; Continuous Cell Cultures have been developed to study the pattern of pulmonary drug delivery using various tracheobronchial and alveolar mucosae (). These *in vitro* culture models involved obtaining cell culture from the lungs of many animal species as well as human, they are reported to be time-consuming as well as capital intensive with a variety of limitations. [68-70]. For instance, the dynamic change of surface within the respiratory tract has not been taken into account by any of the available *in vitro* models [71].

Ex vivo modelling technique such as isolation of perfused animal lung model is deployed in pulmonary drug development researches [72, 73]. These modelling have a number of advantages over cell culture modelling, such as; the preservation of the structure and function of the tissue. However, there are a number of limitations which include; short viable periods of 2–3 h for the tissue, less predictive of deposition of small molecules which may be attributed to the absence tracheobronchial circulation in the models [73, 74].

2.3.2 *In Vivo* Animal Models for Pulmonary Drug Delivery

Different species of small and large animals have been employed for the studies of pulmonary drug delivery [56, 75]. After selection of the appropriate animal, selection of the pulmonary administration of the drug is paramount. There are two methods of administration that include; passive inhalation or direct administration [76].

Nebulised drugs can be delivered to the conscious animal by passive inhalation via inhalation chambers [76, 77]. The inhalation chambers could be whole-body, mouth–only or head-only and the animal could be restrained or unrestrained depending on which chamber is used [76].

In the whole-body chamber, the whole animal will be inside the chamber as such there is no need for restraining. However, there is a possibility of inhalation by multiple routes such as oral, nasal as well as percutaneous, this makes the assessment of inhaled dose very difficult [77].

Nose-only and head-only chambers prevent the exposure to be limited to only one route, however, the animal may experience stress due to restraining [76].

Determination of the delivered dose in passive inhalation is quite challenging due to variability associated with; animal size, anatomy, and breathing

characteristics of the animal, as well as variability in drug formulation, the aerosol-generating device, and the efficiency of the exposure chamber [78].

Direct administration method includes spray installation, and dry-powder insufflation, in this method the trachea of the animal will be visualized by using laryngoscope and thin stainless-steel tube. This will be advanced into the trachea near the carina to administer the drug directly into the lung. This method is performed under anaesthesia or light sedation, the method has more accurate results than the passive inhalation with an added advantage of bypassing oropharyngeal or nasopharyngeal deposition [73, 79].

The lung deposition can be measured with invasive and non-invasive methods; lung imaging such as Gamma Scintigraphy, SPECT, and PET can be used to quantify the deposition of radiolabelled medication [80, 81]. Whereas, real-time in vivo fluorescence imaging can be used to quantify the drugs labelled with fluorophores. However, for the insoluble and inert particles where radiolabelling is impossible Broncho-alveolar lavage (BAL) can be used [56, 75, 82].

2.3.3 Imaging Testing in Pulmonary Drug Delivery

In recent years, Molecular imaging techniques have been applied in several stages of pulmonary drug development owing to their enormous advantages [36]. Particularly Nuclear Medicine/Functional Imaging such as; Gamma Scintigraphy, SPECT and PET imaging. Molecular imaging provide a unique opportunity for studying disease noninvasively along with providing the advantage of assessing disease progression and treatment response qualitatively as well as quantitatively [35, 83]. These methods have been applied both at preclinical and clinical stages of the drug developments. These techniques speed up the drug development processes as well as the drug development costs and provides assessment of certain parameters such as time on target as well as the quantitative biodistribution and the inherent kinetic data which will have been otherwise impossible without the use of the these imaging techniques [83].

2.3.3.1 Imaging biomarkers

Medical imaging has a significant role in the assessment of clinical decisions in many disease scenarios. Imaging biomarkers has transformed the

contribution of radiology within the healthcare cycle. Its role expanded from conventional inputs based on qualitative criteria and the experience of the radiologist to providing quantitative indicators of tissue and organ characteristics [84]. This is achieved through application of image processing tools and algorithms to medical images from modalities like X-ray (XR), magnetic resonance (MR) imaging, computed tomography (CT), ultrasound (US), positron emission tomography (PET), single-photon emission computed tomography (SPECT), among others [85]. Imaging biomarkers have the advantage of being non-invasive unlike the biomarkers obtained by gathering tissue sample from a patient [86].

Imaging biomarkers may have a variety of application such as a diagnostic tool for a symptomatic disease or a screening tool to identify the diseases that is not symptomatic or diagnostic tools or monitoring treatment response [87, 88]. Imaging biomarker may have the key role in the future, accelerating drug development and reducing the cost of drug development trials by eliminating poor drug candidates early in the development process [89, 90]. Radiolabelling of drug compound may allow not only the ability to visualize the drug pathways but will also allow the possibility of quantifying the drug [35]. Animal studies prior to the first human administration, will allow the prioritization of the candidate drug that will go forward to the clinical studies and also will provide the information regarding the dose range and regimen, or even to discontinue a research program if insufficient concentration of the drug accumulates in the desired target.

2.3.3.2 **Gamma Scintigraphy (GS)**

Gamma scintigraphy (planner imaging) has been continually advancing along with the field of nuclear medicine since the first gamma camera was produced in 1964 [91, 92]. A gamma camera is primarily composed of one (or multiple) radiation detectors or heads that are mounted on the gantry [39, 92]. The gantry of modern gamma cameras can be moved in a variety of different configurations for the acquisition of multiple different data sets [39].

The two primary types of image acquisitions that are conducted are 2D and 3D. Planar image acquisition, 2D, has been the historical standard for inhalation deposition analysis [39, 91, 92]. Planar image acquisition involves

the collection of anterior and posterior (typically at the same time with a multihead gantry) images. These images are the only representative of the location of the gamma emission in 2 dimensions and therefore do not reflect depth. These images provide a valid assessment of organ dose and total dose, however, they only provide limited information about the specific location of the deposition within an organ, e.g., lung [33, 93]. Planner imaging provides images of drug delivery as well the quantification of the whole lung deposition, however, it is limited in providing quantification of regional distribution of the drug [94].

The advantage of planar imaging is that the image acquisition time is faster than SPECT and can be conducted with a low amount of radioactivity [83, 95]. The planner and SPECT imaging mainly use Technetium-99 (99mTc) as the radiotracer, which is then incorporated onto a drug molecule. The radiolabelling involved a very complex radiochemistry. There are several methods of radiolabelling of a drug molecule. A typical method in dry powder inhaler, is to adsorbed 99mTc as sodium pertechnetate onto the surface of a drug molecules [96, 97] whereas, in nebuliser studies, 99mTc-diethylene triamine penta acetic acid is added onto the drug molecules [98]. Similar methods are also used in pressurized metered dose inhaler (pMDI) [99]. The advantage of this methods is there is no change in the structure of the drug molecules after the radiolabelling [100]. The disadvantage of planar imaging is that the organs being imaged are 3D and therefore complex analysis of regional deposition is not ideal. However, despite numerous disadvantages, GS has been considered the gold standard in assessing lung deposition from inhalation devices despite its inability to provide information regarding regional distribution within the lung [92, 95].

2.3.3.3 Single Photon Emission Computed Tomography (SPECT)

SPECT image acquisition is a more complex imaging method that requires the gantry to collect data from 360° around the patient [101]. Often dual-headed gantries are used so that each detector only has to rotate 180° to collect all 360° of data. The resultant images allow for a more accurate 3D reconstruction of the patient. The major advantage of SPECT is the increased information on regional deposition and clearance [39, 102-104]. However,

additional time (10 min or more) is required to collect 360° data, which is a disadvantage of SPECT imaging [39, 101]. Several techniques can be utilized to decrease the acquisition times including increasing the radioactivity used, development of a fast, dynamic SPECT imaging protocol using a three-headed camera [39, 105].

Often coupled to SPECT image acquisition is computed tomography (CT) [35]. Most new SPECT cameras are multifunction instruments that include a CT system. Collection of a CT image along with a SPECT image allows for specific anatomical identification and also valuable attenuation correction [106, 107]. Furthermore, it allows the exact outline of the lung to be defined during analysis.

2.3.3.4 Positron Emission Tomography

This is a powerful, quantitative, nuclear medicine tomographic imaging technique. Positron Emission Tomography (PET) can be used to measure physiological effects such as blood flow, metabolism, ventilation, receptor occupancy, regional dose delivery and pharmacokinetics of radiolabelled drugs [39, 40, 108, 109]. It combines principles of image reconstruction from projections with the use of specific biological molecules labelled with positron-emitting radioisotopes (11C, 18F, 15O, 13N) allowing regional measurements of dynamic processes to be taken [39, 102, 110, 111]. The major advantages of PET imaging are better image resolution. However, the disadvantages of PET are the high cost and complexity of image analysis [39].

Many studies have been done to assess pulmonary drug deposition using planer and SPECT imaging. However, very few studies have been done with PET imaging, despite enormous advantages of PET over SPECT imaging and Gamma Scintigraphy [107, 112, 113]. Even though, It has overcome the inherent limitation of producing a 2D image by gamma scintigraphy and by allowing the possibility to include the radiolabelled isotopes within the structure of the drug making it chemically and pharmacologically identical to the molecule before labelling [108]. Lack of many PET scintigraphy may not be unconnected to the lack of availability of the PET imaging modality in many centres.

18F-2-fluoro-2-deoxy-D-glucose ([18F]-FDG) is the major PET radiopharmaceutical mainly used in oncology and brain imaging to monitor the metabolic activity of cells in vivo and to detect tumours [39]. [18F]-FDG differs from glucose by the substitution of the hydroxyl group with a fluorine atom on the second carbon of the glucose [19] leading to intracellular trapping. When injected intravenously, [18F]-FDG rapidly diffuse into the extracellular spaces throughout the body [39, 111]. It is transported into living cells by the same mechanism as glucose, via the D-glucose transporter-1 (GLUT-1) and is phosphorylated by hexokinase to fluoro-deoxyglucose-6-phosphate [114]. The deoxy substitution at the second carbon position prevents further metabolism and the product accumulates in the cell at a rate that reflects glucose metabolism [108, 111]. The GLUT-1 catalyses facilitative diffusion of glucose into erythrocytes and is responsible for glucose supply to the brain and other organs [115]. Increased glucose consumption is assumed to lead to an increased rate of tracer uptake. The rate of accumulation of [^{18}F]-FDG in tissue after intravenous injection reflects the combined transport and hexokinase activity in the cells. However, PET studies of the inhaled [18F]-FDG are few compared to the number of oncological, neurological and cardiac studies. Measuring total and regional lung deposition using inhaled PET radiotracers has been done in the pass [40, 110, 116].

2.4 Positron Emission Tomography in Idiopathic Pulmonary Fibrosis (IPF)

2.4.1 Background

The idiopathic interstitial pneumonias (IIPs) otherwise called interstitial lung diseases (ILD) are a group of diffuse parenchymal lung diseases of unknown origin [117, 118]. The IIPs are heterogeneous non-neoplastic group of disorders with varying patterns of inflammation and fibrosis [119-121]. The interstitium includes the space between the epithelial and endothelial basement membranes and it is the primary site of injury in the IIPs [117, 122, 123]. However, the diseases may also involve airspaces, peripheral airways and pulmonary vasculature [117, 124]. IIPs can be distinguished from other forms of diffuse parenchymal lung disease clinic-radio-pathologically [125-127]. There is some controversy regarding their classifications due to the

inter-relationship between them and the confusion led to the subject being referred to as ‘’Alphabet soup’’ [128].

Idiopathic Pulmonary Fibrosis (IPF) is the most frequent and deadliest form of Idiopathic Interstitial Pneumonias (IIPs) [118, 121, 125, 129]. It is progressive and irreversible with the median life expectancy of 2-4 years after diagnosis [120, 125, 130]. Despite several studies on IPF, the aetiology is still not fully understood [[131, 132]. However, several factors such as genetics, environmental and viral infection have been associated with the incidence of IPF [129, 133], it is more predominant in males with an associated history of smoking [129]. It is common among elderly people (above 50 years), there is an incidence of about 100-fold higher in people above 75 years of age than in those below 50 years of age [129]. IPF has been shown to have a high mortality rate than some malignancies such as bladder cancer [133, 134]. UK has the highest incidence of IPF in Europe with 7.94/100,000, 3.4 in Norway, 3.0 in Spain, 2.17 in Denmark and 0.22 in Belgium [135-137].

2.4.2 Epidemiology and Risk Factors of IPF

IPF has the poorest prognosis among interstitial lung diseases, due to fewer effective treatment available [118, 133, 138]. There are many recognized risk factors but the aetiology of the disease remain unclear. The implication of genetic factors has been considered [133, 138]. Genetic factors has been implicated in the pathogenesis of IPF due the presence of familial IPF. Telomerase mutation has been associated with IPF and have been found more frequently in familial IPF than Sporadic IPF [129, 131, 138]. Alveolar epithelial cells injuries caused by environmental factors such as; smoking, inhalational agents, drugs, oxygen radicals, toxins, and viruses are thought to be the initial cause. Repeated alveolar injuries has also been suggested to be the primary site of the disease [124, 129, 131, 139, 140].

Mutation in Surfactant protein C (SFTPC) and A2 (SFTPA2) have been found in 10-15% of Familial IPF but not in Sporadic [129, 131, 141, 142]. Surfactant gene mutation resulted in impaired homeostasis which subsequently leads to failure of tissue repair leading to abnormal epithelial-mesenchymal interactions and finally results in pulmonary fibrosis [143]. Although the etiological factors or agents are numerous and not fully understood,

developing an effective treatment strategy for IPF will fully depend on the understanding of how these etiological agents trigger fibrosis, as well as, understanding the mechanisms of deregulated homeostasis after initial injury may lead to the development of effective treatment strategy against IPF [135, 136].

1.1.1. **Pathogenesis**

IPF is believed to be triggered by diffused alveolar epithelial injury which progresses to pulmonary fibrosis [78, 129, 135, 138, 144]. Although the pathway to this end stage involves endothelial and/or epithelial cell injury followed by an inflammatory response and later fibroblast stimulation. The factor(s) responsible for initiating excess fibroblast growth and collagen production is unknown [143]. Moreover, transforming growth factor β1 (TGFβ1) has been shown to irreversibly converts fibroblasts into pathological myofibroblasts, which express smooth muscle α-actin (α-SMA) and produce extracellular matrix proteins, such as procollagen I (α1) which subsequently differentiate to fibrosis [145-150]. Several studies suggest that oxidant-antioxidant imbalances in the lower respiratory tract play a significant role in the pathogenesis of IPF. High oxygen tension in the lungs from exogenous and endogenous oxidants predisposed lung to high oxidative stress leading to activation of inflammatory cells to generate free radicals [151, 152]. Modulation of protease-antiprotease imbalance by reactive oxygen species (ROS) has been found to promote profibrogenic environment in the lungs [150]. Several cytokines and growth factors have been reported to mediate the pathogenesis of pulmonary fibrosis [152]. Apart from directly injuring lung cells and matrix, oxidants have also been implicated in the development of pulmonary fibrosis by their direct effects on cytokines and growth factors [152]. The mediators such as; transforming growth factor (TGF-β), is a key regulator of both normal wound repair and the aberrant repair mechanisms characteristic of many fibrotic diseases, including pulmonary fibrosis [152]. TGF-β released early following lung injury act as a pro-inflammatory molecule. Later, its' function switch to resolution of inflammation and initiation of repair [152]. It has been hypothesised that unabated continuation of repair after resolution of inflammation results into chronic pulmonary

fibrosis [129, 150]. TGF-β, therefore, may be an important mediator of chronic but abnormal repair.

2.4.3 Diagnosis

Non-productive cough exacerbated dyspnoea is the typical presentation of IPF, thus patients are more often evaluated and treated for other diseases such as; bronchitis, asthma or heart failure before establishing the diagnosis [118, 129]. A detailed occupational history needs to be requested to rule out other possible causes of the symptoms and fibrosis [118].

Non-invasive biomarkers, in early diagnosis, differential diagnosis, prognosis and prediction of therapeutic response are needed in the management of IPF. Serum biomarkers are important diagnostic tools, they are both less invasive and reproducible. However, there are no universally accepted biomarkers for IPF [153, 154]. Biomarkers are categorized according to the pathways involved in the pathogenesis of the disease. Biomarkers associated with alveolar epithelial cell dysfunction; biomarkers associated with extracellular matrix remodelling and fibroproliferation; as well as biomarkers related to immune dysfunction [155].

Surfactant protein (SP)-A, SP-D, and KL-6 are commonly used as serum markers of interstitial pneumonia, including IPF, they have been shown to function as host defence lectins in the lung [153, 155]. These carbohydrate-binding proteins are mainly synthesized by alveolar type II cells. The probable mechanism for the increased level of these proteins in IPF patients may be a combination of a loss of epithelial integrity due to injury and an increased mass of type II cells due to hyperplasia [153]. It has been revealed that these proteins are useful for monitoring the clinical course and predicting prognosis as well as for the diagnosis of IPF [153, 155].

Mucin 5B (MUC5B) is involved in the protection and lubrication of respiratory, gastrointestinal and reproductive tracts [155]. MUC5B dysfunction has been extensively studied in the pathogenesis of obstructive airway disease [156]. MUC5B producing cells have been found in the pseudostratified epithelium of honeycomb cysts in IPF [156]. Increased expression of MUC5B in IPF have been linked to the present of single

nucleotide polymorphism (SNP) of the MUC5B promoter on chromosome 11 (rs35705950) [157-159]. Cleaved cytokeratin 18 (cCK-18) serum level are also reported to have increased in patients with IPF, but not in other interstitial lung diseases. However, it has not been associated with the disease severity or the outcome of IPF [160]. Numerous degenerative disorder have been associated with telomerase mutations [161]. Mutations in TERT and TERC and consequent abnormal telomere shortening have been found in 8-15% of familial pulmonary fibrosis and 3% sporadic cases of IPF [162].

Additionally, the bacterial burden in IPF lungs, as shown from microbial analyses, as well as mitochondrial DNA seem to have promising roles as biomarkers [163, 164]. Using a combination of multiple biomarkers for the (early) diagnosis, prognosis and prediction of therapeutic response has the potentials in the management of IPF patients.

Histological appearance of usual interstitial pneumonia is the gold standard in the diagnosis of IPF [122, 165]. However, due to the invasive nature of the biopsy, coupled with the advanced age of the patients (mostly above 70), clinical and radiological information is heavily relied on. According to ATS/ERS [122] guidelines, the biopsy should only be done when clinical and radiological information is unclear.

2.4.4 Clinical Imaging of IPF

The typical chest radiographic findings in IPF includes; bilateral reticular opacities predominantly at the periphery of the lungs and most commonly in the lower lobes [125]. Progressive lungs fibrosis may lead to cystic dilatation of the distal air spaces, which is viewed as peripheral ‘’honeycombing’’. Moreover, traction bronchitis may develop as a result of reduced parenchymal compliance, which is visible as thicken and dilated airways [125]. However, biopsy-proven IPF with normal chest radiograph has been reported [122]. A Molecular Magnetic Resonance Imaging (MMRI) with a probe targeted to type I collagen may be a potential method in assessment of pulmonary fibrosis [166].

High-Resolution Computed Tomography (HRCT) is the mainstay imaging modality in the diagnosis of IPF [26, 167-169]. It provides higher-level spatial

resolution enabling visualisation of the lungs parenchyma up to the level of pulmonary lobules [170]. The typical HRCT features of IPF includes; patchy peripheral reticular abnormalities with interlobular linear opacities, irregular septal thickening, subpleural honeycombing typical of Usual Interstitial Pneumonia [171] pattern, and traction bronchiectasis [[131, 168, 170, 172]. HRCT help physicians' in reaching a confident diagnosis in about 80% of cases without the needs for biopsy [30, 125, 168].

The clinical course of IPF is unpredictable due to acute exacerbation (AE-IPF) of the disease in some patients [120, 144]. The factors responsible for acute exacerbation (AE) are not well understood [144]. Acute exacerbated IPF (AE-IPF) is an important determinant in the prognosis of the disease and is associated with over 70% mortality rate [144]. There are currently no prognostic measures to assess the likelihood of disease progression [125, 173]. Subtle changes in the volume and character of abnormalities can be difficult to assess with HRCT [130, 169]. Positron emission tomography (PET) imaging has the potential in monitoring the progressive changes of the disease [130, 173].

[^{18}F]-FDG has shown to have high target-to-background ratio (TBR) pulmonary uptake in areas of lung parenchymal abnormality of HRCT in patients with Interstitial fibrosis [[174]. The uptake correspond more to the areas of honey combing than areas of ground glass. [175]. Other studies evaluating somatostatin analogues (^{68}Ga-DOTATATE and ^{68}Ga-DOTANOC) PET/CT in patients with IPF and nonspecific interstitial pneumonia (NSIP) has been conducted. In IPF, somatostatin analogues uptake was peripheral, subpleural, and directly correlated with pathologic areas on HRCT (subpleural/reticular fibrosis, honeycombing). However, a very low tracer uptake was observed in NSIP patients corresponding to HRCT areas of ground-glass opacity [174].

Normal-appearing lung on HRCT in IPF has demonstrated significant high [18F]-FDG uptake in comparison to patients with known pulmonary disease [130]. These findings may be as a result of abnormal parenchymal changes undetectable on HRCT. Increased [^{18}F]-FDG uptake could also be due high

sensitivity of [^{18}F]-FDG -PET in the detection of early pulmonary disease in IPF than HRCT [176]. Leucocytes has been suggested to be the cell type responsible for the increase [^{18}F]-FDG uptake in early stage (Inflammatory phase) of fibrosis [173]. These findings has implication for the in vivo pathogenesis of IPF, it may provide a possibility of earlier detection of subtle changes in disease activity and this will help in prediction of disease exacerbation [175].

Standardized uptake value Retention index (RI-SUV) was considered useful for determining disease activity as a predictor of disease progression in idiopathic interstitial pneumonia (IIP) after 12 month of follow up [177]. Dual PET-CT imaging after intravenous injection [^{18}F]-FDG was conducted in patients with IIP. The images were taken one hour and 3 hours after injection of [^{18}F]-FDG. Standardized uptake value (SUV) from the ROIs around normal appearing lung parenchyma in the both images were calculated. RI-SUV between the early (1hr) and the delay (3hr) images was determined. In this study, Low early SUV level (< 1.5) and positive RI- SUV (> 0%) was suggested to predict progressive IPF and NSIP patients and Low early SUV level (< 1.5) and negative RI-SUV (< 0%) was suggested to predict stable IPF and NSIP patients.

2.4.5 Preclinical IPF Imaging Model

PET/CT with [^{18}F]-FDG– and ^{18}F-4-fluorobenzamido-N-ethylamino-maleimide (^{18}F-FBEM)–labelled leukocyte for metabolic activity and leukocyte recruitment monitoring in a Mouse model of Pulmonary Fibrosis has been developed [173]. In this model, pulmonary fibrosis has been induced by treating mice with bleomycin. Increased [^{18}F]-FDG uptake at the inflammatory and fibrotic phase of the disease has been recorded. The [^{18}F]-FDG uptake begins at day 7 of the experiment and remains high up to 30 days after installation of bleomycin. However, in [^{18}F]-FBEM–radiolabelled leukocyte pulmonary uptake was also notice in early stage, however, drastically reduced after 14 days of bleomycin administration and completely disappeared at day 23 [173]. This confirm the extent of inflammatory cells (macrophages, neutrophils, and lymphocytes) involvement at the early stage of the disease process. The persistent increase [^{18}F]-FDG in the late fibrosis

phase is not explained by an active recruitment of leukocytes, therefore, may be due to fibrotic processes.

It has been hypothesised that the late [^{18}F]-FDG uptake probably results from a high glucose consumption in proliferating fibroblasts or collagen-producing myofibroblasts due to oxidative stress [173]. Similar condition seen in tumour-associated fibroblasts, with an increase in hydrogen peroxide concentration in the tumour microenvironment driving the enhanced glucose uptake by fibroblasts under oxidative stress [178, 179]. Increased [18F]-FDG uptake in IPF has also been suggested to be due to the relative increase in pulmonary blood volume, as erythrocytes express glucose transporter type 1 [180]. Conversely, the above hypothesis is unlikely as increased [^{18}F]-FDG was clearly demonstrated in autoradiographic images of exsanguinated lungs in bleomycin-treated mouse [173].

The positive influence of somatostatin receptor (SSTR) expression on fibroblasts has been suggested [181]. In another study, longer survival of mice with fibrotic lungs treated with agents blocking SSTR has been observed [182]. This supports the hypothesis of imaging fibroblast activity in vivo by visualization of SSTR with ^{68}Ga-DOTANOC and ^{68}Ga-DOTATATE PET/CT [174].

The potential of PET-CT for becoming a promising imaging tool to select patients for therapeutic interventions and to assess response to therapy is undeniable. In addition, there is strong need to further characterize the biology underlying PET Tracers uptake in lung fibrosis.

2.5 Aim and objective

- Prediction of drug delivery performance in the human lung is most often based on observations in commonly used laboratory animals and lung surrogate devices such as cascade impactor. Even though these methods are useful but the complexity and numerous biological interactions of a drug and delivery system can only be accurately evaluated in vivo. Gamma imaging is considered the gold standard imaging modality for the quantification of lung deposition or lung dose of inhaled therapeutics, however, this imaging modality has

number of limitation such as; being a two dimensional images producing images with poor accuracy, moreover, regarding regional deposition of the drugs cannot be ascertain using Gamma imaging. The aim of this experiment is to explore the use of PET imaging which is more sophisticated, highly sensitive and 3 dimensional imaging modality to visualised and quantify the lung deposition and distribution of [^{18}F]-FDG and orally inhaled products (OIPs) using in-house made lung surrogate phantom and cascade inhaler.

- High resolution Computed Tomography (HRCT) is the gold standard imaging modality for the diagnosis of Idiopathic Pulmonary Fibrosis. It provide radiological features consistent with UIP with complement pathological diagnosis of the disease. However, HRCT is unable to differentiate active from non-active fibrosis or to inform which patient is likely to progress to exacerbated IPF. Positron Emission Tomography (PET) is a molecular imaging that provide information from cellular and molecular level. High uptake of [18F]-FDG PET in areas of apparently normal lung parenchyma in IPF has been reported in the literature. The experiments was conducted using semi-quantitative method of measuring PET data called standard uptake value (SUV). The aim of this experiment is to explore other method of measuring PET data such as different SUV normalisation and textural features analysis.

Chapter 3 Positron Emission Tomography (PET) for Assessing Aerosol Deposition of Orally Inhaled Drug Products: Pre-clinical Study

3.1 Background

"The quantification of lung deposition or lung dose of inhaled medicines is problematic but of vital importance in the development of new inhaler technologies [54, 55]. The solution to this problem of quantification has typically included three primary techniques, systemic pharmacokinetic analysis, in vitro measurement techniques (cascade impactors analysis), and deposition imaging [183]. As with nearly all measurement techniques, each of these has its advantages and disadvantages. However, Gamma scintigraphy has been dubbed an "industry standard" for assessing deposition from inhalation devices this can be explained by its' unsophisticated nature in both data acquisition and analysis [184]." However, the quality of regional Lung deposition data obtained by gamma scintigraphy is relatively poor [184]. Many studies have been done to assess pulmonary drug deposition using planner and SPECT imaging. However, very few studies have been done with PET imaging, despite the enormous advantages of PET over SPECT imaging and Gamma Scintigraphy [106, 107, 110, 185]. Even though, It has overcome the inherent limitation of producing a 2D image by gamma Scintigraphy and by allowing the possibility to include the radiolabelled within the structure of the drug making it chemically and pharmacologically identical to the molecule before labelling [108, 186]. PET has been considered to be the most accurate of the three imaging methods for quantifying lung deposition and was even claimed as ‘'the only generally reliable quantification in Nuclear Medicine".

The phantom design was my idea and it was constructed at the university of Hull Chemistry workshop where individual pieces of the items where gathered and put together. The phantom experiment was an attempt to promote the use of an alternative methods of carrying out preclinical research other than using animal. As at the time of this experiment, there was no available literature on inhalational PET studies to quantify lung deposition of [1^{8}F]-FDG/aerosolised drug in humans. Using phantom as a lung surrogate to

understand the amount of radioactivity required, duration of the inhalational procedure as well the risk of radiation air borne contamination was sensible. Gamma imaging has been used extensible to determine deposition pattern of inhalational drugs [83]. Looking at the better sensitivity and resolution of PET, I believe PET will hold more advantages over Gamma imaging in deposition scintigraphy. I initially designed an experiment using a nebuliser attached to a pump and the filters (fig 4) to quantify the rate of aerosol depositions. To better understand the pattern a 1.5 litres phantom cylinder (the size of an adult human lung) was designed. No similar experiment have been found in the literature.

This is a ‘'proof of concept" study to determine the quantification of lung deposition or lung dose of [18F]-FDG, using Positron Emission Tomography-Computed Tomography (PET-CT) scanner. This study could be used in testing inhalational devices and could be utilized to establish dosing for new medications and it may inform inhalation as a better way of delivering [18F]-FDG into the lungs for diagnostic and treatment purposes.

3.1.1 Aims

- The aim of this experiment is to explore the use of PET imaging which is more sophisticated, highly sensitive and 3 dimensional imaging modality to visualised and quantify the lung deposition and distribution of [^{18}F]-FDG and OIPs using in-house made lung surrogate phantom.
- To investigate potential radiation risk of the inhalation of the radioactivity to the patient and operator

3.2 Materials and Method

This study is ‘’proof of concept’’ with limited literature, series of experiments was conducted with each experiment expected to lead and guide the successive experiment. Each experimental procedure was conducted repeatedly over a certain period to reduce the level of experimental errors. To our knowledge, this is the first phantom experiment quantifying the deposition pattern of aerosolized [^{18}F]-FDG while mimicking human tidal breathing. The phantom used in this experiment was built in-house for the purpose of this experiment only. The procedure was conducted at University

PET Centre as well as The Jack Brignall PET-CT Centre, Castle Hill Hospital with the help of the radiochemists and the radio physicists working in the Centres.

3.2.1 Phantom design Material

The choice of sponge to be used as a lung surrogate was based on its similarity in density with the lung using CT number, -987HU and -1000HU for sponge and lung respectively. The phantom was designed using; 500mL pump, corrugated tubes, nebuliser, filter pads as well as 2 filter covers. 3 litres Perspex cylinders (30×10cm) were created along with a 30mm lead castle. A sponge with similar density as lung was purchased to fit in the 3 litres Perspex cylinders. These materials were used to develop to different phantoms for different experimental purposes.

3.2.2 Assessment of nebuliser output

3.2.2.1 Overview

Another phantom model was designed to assess the consistency of the nebuliser output. The amount of aerosol nebulised depends heavily on the efficiency and consistency of the nebuliser. This experiment was meant to assess the volume lost from the nebuliser after one-minute nebulisation and to ascertain the time taken by the nebuliser to completely nebulise 2 mls of 0.9% saline under the same operation condition. Knowing the volume loss will help in determining the amount of radioactivity nebulised per unit volume in Becquerel/millilitre This is achieved by weighing the filters before and after each nebulisation procedure until no aerosol is observed coming from the nebuliser. The volume loss from the nebuliser will be calculated by weighing the nebuliser pre and post nebulisation. In this experiment, the phantom cylinders containing the sponges was removed and replaced by a filter cover containing 2 set of filters.

3.2.2.2 Materials and Methods

An experimental model was developed by attaching the nebuliser to the exhaust filter cover and a pump via a three-way connecting tube. There was another filter cover (inhalation filter cover) placed between the connecting tube and the 500mls pump acting as lung surrogate. This set up allows the ventilation procedure to be carried out by drawing the pump handle back and

forth with users mimicking their tidal breathing of 16-18 breaths per minute (Fig 4).

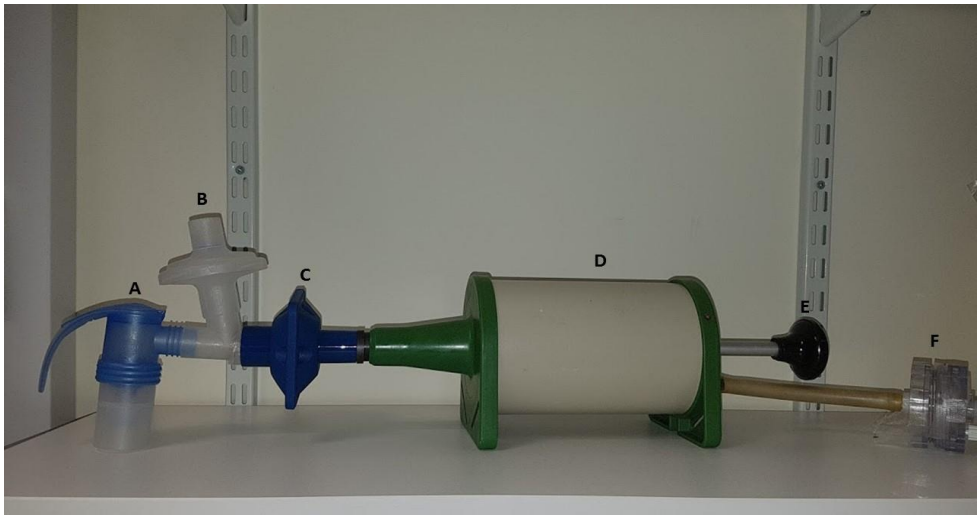

Fig 4: a lung model consisting of a nebuliser (A), connected to two (2) filter covers exhaust filter cover (B) and inhalation filter cover (C) which save as a lung surrogate, each filter cover have to set of filters., using a pump (D) to draw out the aerosol, the pump handle (E) was drawn back and forth. In case of any aerosol escaping through the pump, and additional filter cover (F) was put in place behind the pump. The operator mimic their tidal breathing while drawing the pump handle.

A cold experiment was conducted by dispensing 2mLs of 0.9% saline into the nebuliser. The nebuliser was weighed pre and post nebulisation to ascertain the nebuliser volume loss and the linearity of the nebuliser output. The procedure was conducted 8 times, each time the ventilation was conducted for 1, 2, 4, 8 and 10 minutes. At the end of each time point, the nebuliser was disconnected and a four decimal sensitivity weighing scale was used to calculate the nebuliser volume loss (Fig 5 and 6). The filters were weighed pre and post one-minute nebulisation to ascertain the deposition.

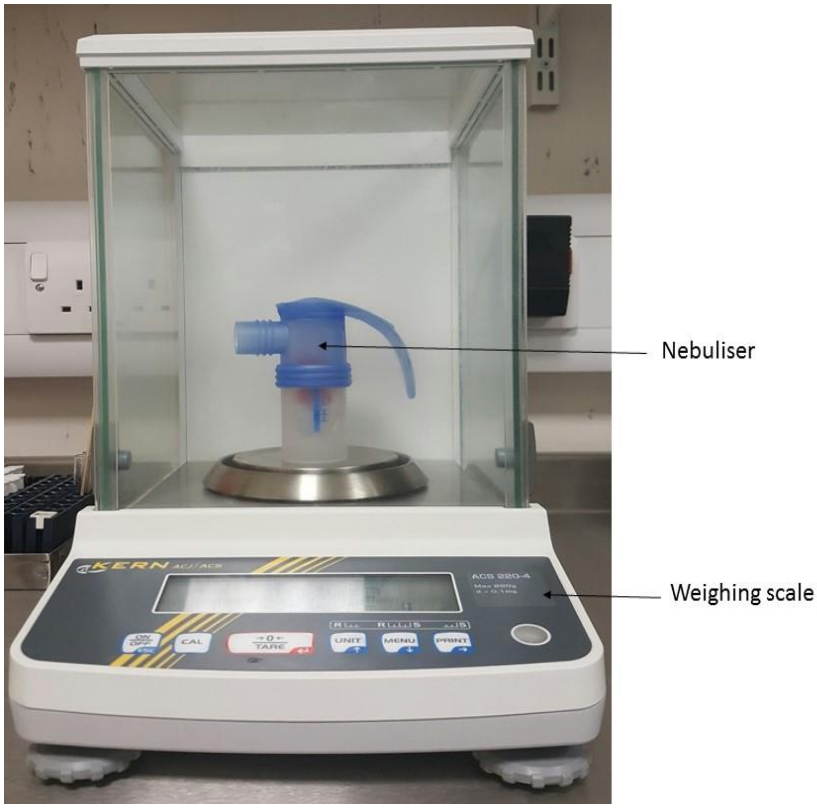

Fig 5: Kern ACS 80-4 Analytical Balance Scales. At the end of each time point, the nebuliser was disconnected and weighed to determine the volume lost due to the aerosol formed during the nebulisation procedure.

3.2.2.3 Results

The main purpose of this experiment was to ascertain the volume nebulised at the end of one minute and to establish the linearity of the nebuliser out. The nebuliser output was recorded to be linear until the nebuliser reaches sputtering at 10:46/m:s ± 0.24s (Fig 3 Table 1). The average nebuliser output at the end of one-minute nebulisation procedure was 0.21 ± 0.01µg.

Measurement of Nebuliser Output											
Nebulization Time (min)	Amount of 0.9% saline nebulised (µg)								Mean	SD	SE
1	0.22	0.22	0.22	0.21	0.21	0.2	0.21	0.2	0.21	0.01	0.002
2	0.41	0.42	0.4	0.41	0.41	0.42	0.41	0.42	0.41	0.01	0.003
4	0.17	0.84	0.77	0.64	0.61	0.81	0.82	0.77	0.68	0.22	0.003
8	1.52	1.58	1.47	1.32	1.27	1.62	1.65	1.51	1.49	0.14	0.05
10	1.85	1.91	1.69	1.68	1.73	1.9	1.91	1.83	1.81	0.10	0.04

Table 1: the nebuliser was filled with 2 mL of 0.9% saline, after one-minute nebulisation procedure, the nebuliser was disconnected and weighed. The nebuliser was filled in again with 2mLs before the repeat (2, 4, 8 and 10 minutes). Each time-point was repeated 9 times.

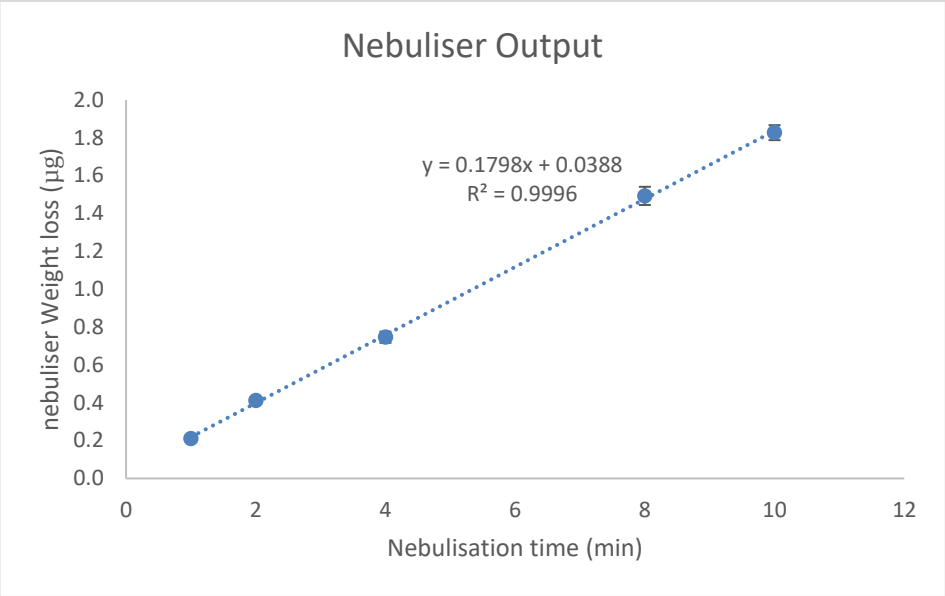

Fig 6: This experiment was to establish the efficiency and consistency of nebuliser output. Nebuliser weighted before dispensing 2mls of 0.9% saline and weighted after each minute until sputtering. Each experiment was conducted 8 times.

3.2.2.4 Discussion

The time-point nebuliser volume loss was consistent and increases progressively as the time of nebulisation procedure increases. These suggested linearity in the nebuliser output. The nebuliser reaches sputtering after 10 minutes nebulisation.

3.2.2.5 Conclusion

In this experiment, the linearity of nebuliser output was assessed and appeared to be linear. Furthermore, the decision to nebulised for one-minute was made, with the expectation of nebulising 0.21 ± 0.01µg of saline.

3.2.3 Assessment of 3M Filtrete™ medium (GS-GBS-type) efficiency

3.2.3.1 Overview

In this experiment, a 3M Filtrete filter medium is used in the nebuliser exhaust and the pump exhaust to capture the aerosols. Subtracting the aerosol deposition on the filters will provide an idea of the mist. This information will

be useful in estimating the risk of inhalation of radioactive substances and the calculation of radiation dose to the patient. The 3M FiltreteTM medium (GS-GBS-type) is made from polypropylene (pp). The filter fibres are electrically charged, designed to capture airborne particles. The filters were reported to have 98% efficiency in capturing airborne particles based on the manufacturers' (PARI) TSI 8110 automatic filter Tester (AFT) for efficiency and pressure dropping, using NaCl as the test aerosol with the mean particle size of 0.1µm (Appendix 1). The filter pads are popularly used with nebulisers to reduce the amount of aerosol medications escaping to the surrounding environment. We hope these filters will be efficient enough to capture radio-aerosols from escaping to the surrounding environment.

3.2.3.2 Method

Two separate experiments were conducted (cold and hot experiments). The cold experiment involved the use of two (2) sets of filter pads inserted into the exhaust filter cover and 2 were inserted into the inhalation filter cover (Fig 4). The idea of having two sets of filters was to be able to capture any mist that escapes the first filter. The nebulisation procedure was carried out for one minute. In the hot experiment, four (4) sets of filter pads were used as explained above. The nebulisation period was one-minute in both experiments. The hot experiment was conducted in the scanner with an operator (radio physicist) using the necessary personal protective equipment including a 3M FFP3 face mask. The nebuliser was shielded with 30mm of lead. About 2.1mls containing 4.22MBq of [18F]-FDG was dispensed into the nebuliser. Nebulisation procedure was conducted for one-minute as described above. At the end of the hot experiment, the filters were removed using a tong and placed in separate resealable bags and measured using Berthold LB124 contamination monitor. The top of the exhaust filter cover, inside the filter cover, inside the nebuliser outlet as well as inside the lead castle were swabbed to account of the activity deposition. The count-rate was converted to activity by dripping a known amount of activity on to the filter and measured using Berthold LB124 contamination monitor at a different time interval. The decay corrected activity was correlated with the count per second (CPS) to derive a factor used in calculating the activity (Fig 7).

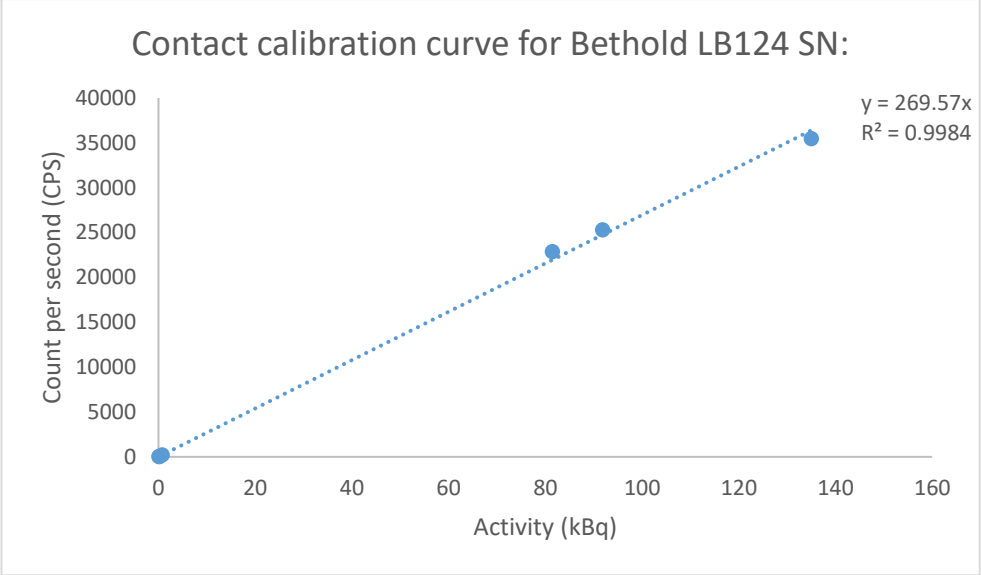

Fig 7: Correlation graph demonstrating the relationship between count-rate (CPS) and activity (kBq)

3.2.3.3 Results

At the end of one (1) minute nebulisation for the cold experiment; the first exhaust and lung surrogate filters captured (Mean and SD) 0.055 ± 0.006 and 0.054 ± 0.010µg respectively. Whereas, the second filters in both sets captured 0.003µg ± 0.004µg and 0.004 µg ± 0.006µg respectively. An attempt was also made to swab the mist on the exhaust and lung surrogate filter covers which gave 0.011 ± 0.008 and 0.041 ± 0.0201µg respectively. The total aerosol capture on the 2 exhaust filters and 2 lung surrogate filters, as well as the filter cover, was 0.17 ± 0.05µg. The deposition of the 0.9% saline aerosol on the filters was calculated by weighing the filters pre and post nebulisation. At the end of the hot experiment; the radio-activity captured on the first nebuliser exhaust filter (the inner filter) was 8.96 ± 1.49kBq, the amount captured on the second filter was 2.75 ± 0.38kBq while the third and fourth filters have 0.80 ± 0.15kBq and 0.31 ± 0.151.80kBq respectively. The pump filters, however, has no significant depositions, with the inner and most external filters have 0.03 ± 0.02 and 0.03 ± 0.01kBq respectively. Inside the lead castle 0.03 ± 0.02kBq, inside the filter cover 33.13 ± 4.28kBq, on the exhaust filter cover outlet 0.25 ±0.05kBq and inside the nebuliser outlet 4.49 ± 0.87kBq.

3.2.3.4 Discussion

At the end of the cold experiment, a significant amount of aerosol was captured by the first exhaust and lung surrogate filters. The aerosols captured on the second filters may indicate that not all the aerosol was captured by the first filters and may also suggest the likelihood of mist escaping to the environment. However, the total amount of aerosol captured on both sets of filters was 0.04µg less than the total amount of loss from the nebuliser after one-minute nebulisation. These findings suggested the possibility of mist escaping to the surrounding environment. As such, an addition of 2 more filters in the hot experiment to increase the safety of the procedure was made. After the hot experiment, the first exhaust filter (inner) has the highest uptake than the rest of the four filters. The fourth (outermost) filter has the least uptake (<1kBq). The swabs of the of the exhaust filter outlet produce very little activity (0.25kbq), this may suggest some trace of activity escaping to the environment or may be a result of contamination. This may also be a result of measurement errors. In case of escape of activity to the environment, this may be clear when the initial activity in the nebuliser increases from 4.22MBq to clinical level (>100MBq) in future experiment.

3.2.3.5 Conclusion

The 3M FiltreteTM medium (GS-GBS-type) is tested to be highly efficient in capturing aerosol following nebulisation procedure. The deposition on the second filters in the cold experiment suggested the addition of 2 other filters in the hot experiment to further reduce the risk of inhalation of radioactive substance. The small amount of activity captured on the fourth filter has given a variety of possibilities. This will be further investigated in the future experiments when the initial activity in the nebuliser has increased.

3.2.4 Radiation safety assessment

3.2.4.1 Overview

After successful cold experiments, other experiments were designed to accurately measure the amount of radioactivity lost from the nebuliser and to prevent the escape of activity into the atmosphere following a nebulisation procedure. In these experiments, a new lung surrogate phantom was designed, for better representation of human lungs.

3.2.4.2 Method

The phantom consists of two cylinders made of Perspex measuring 30 cm long and 10 cm in diameter (Fig 8). There are two corrugated tubes connecting the phantom to the nebuliser and pump. Each tube has two separate parts; A curved part connecting the two cylinders together and the other longitudinal part connecting the phantom to either the nebuliser or the pump.

Reticulated sponge (TR22/10BU) with about the same density as human lungs was used as a lung substitute. These form were used by another group to test for simultaneous dual isotopes SPECT V/Q imaging. This sponge allow absorption of Tc-99m liquid tracer and Kr-81m gas diffusion similar to human lungs [187].

The phantom setup was placed on the scanner table enclosed in a bag. The nebuliser was shielded with 30mm of lead. About 2.1mls containing 477.34MBq of [18F]-FDG was dispensed into the nebuliser. Nebulisation procedure was conducted for one minute as described above.

Four (4) filter pad was inserted into the exhaust filter cover to prevent risk of inhalation of radiation. At the end of the nebulisation procedure, the filter pads were removed and radiation level was measured using Berthold LB124 contamination monitor. The count-rate was converted into activity as explained in the previous section.

The operator used personal protective equipment (PPE), which include; full body gowns, overshoes, gloves and tongs. 3M FFP3 face mask was also used to further prevent the risk of inhalation or ingestion.

These masks are designed for use in infectious aerosol-generating procedures and were fit tested by all staff working within the area before the nebulisation procedure.

At the end of the imaging experiment, the filters were removed from the exhaust filter covers, each individual filter was placed in a resealable bag and quantified using contamination monitor. All calculations were made after decay correction to the nebulisation time.

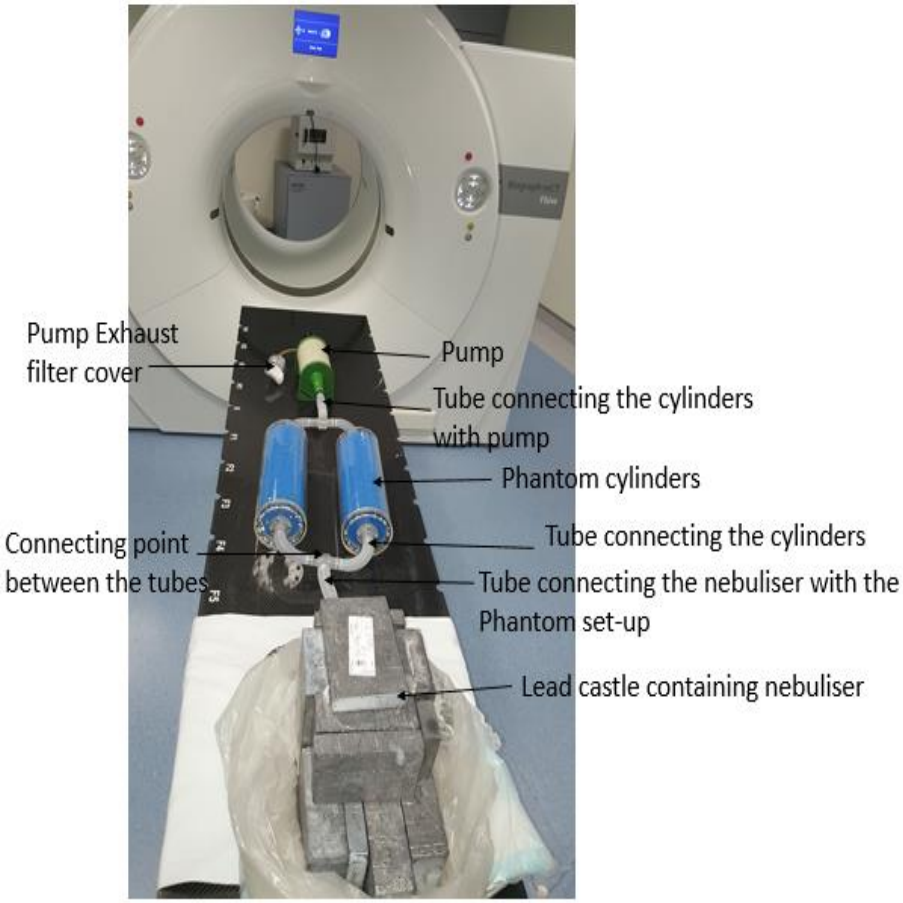

Fig 8: The phantom set-up consisting of castle, which houses the nebuliser, connecting tubes, lung phantom cylinders and pump

3.2.4.3 Results

At the end of the nebulisation procedure, the filters were taken out for measurements. The [18F]-FGD uptake on the first (inner) filter uptake was 178.41kBq, however, the fourth (outmost) filter has 2.3kBq. The uptake on the fourth (outermost) pump filter was 0.2kBq. There was no evidence of any radiation contamination in the room above background radiation level. Images of the phantom (Fig 9) shows neither uptake within the bag (outside the phantom cylinder or the tubes) no was there any uptake at the pump side of the phantom cylinder.

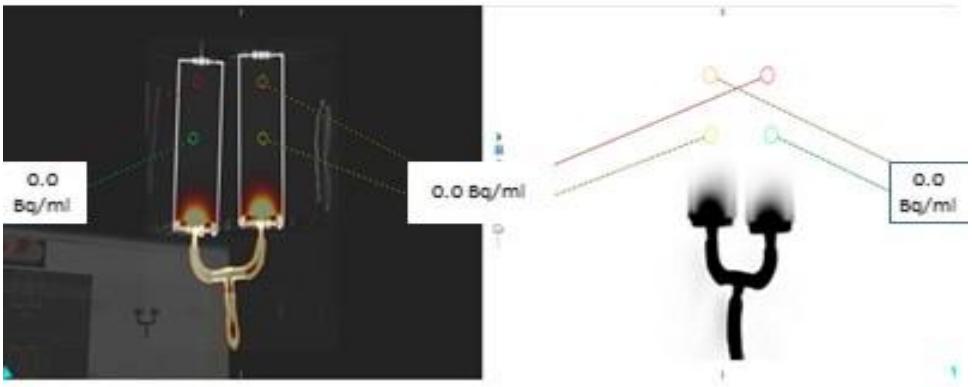

Fig 9: Sagittal and Maximum intensity projection (MIP) of the phantom images demonstrating the radioactivity distribution following the nebulisation procedure. The part of the phantom cylinder closer to the pump was not considered for quantification.

3.2.4.4 Discussion

Several experiments was conducted using polystyrene balls as well as different types of foams to fill in the phantom cylinders. There was no homogeneity in distribution of the radioactivity within the phantom cylinders using polystyrene balls and all of the foams used in this experiment except one sponge (TR22/10BU) sponges. This sponge was found to have similar density as the normal lung, this has been validated by comparing the CT number as well as the SUV of the sponge and the lung. The CT number of the aerated lung is -1000HU whereas the CT number of the sponge was -987HU, moreover the average SUV (BW) of the normal lung is 1.5 Bq/ml and that of the sponge was 1.4Bq/ml. A research group from Royal Brompton and Harefield have compared the uptake of radioactivity within different sponges using dual isotope (Tc-99m liquid tracer and Kr-81m gas). In all of their experiment TR22/10BU proved to have the highest homogeneous signal.

A significant amount of activity was stopped from getting out of the nebuliser by the first (inner) nebuliser exhaust filter, and only 2.3kBq was captured by the fourth (outermost filter). In comparison to the previous experiments, this

is in line with the previous experiment, when the initial activity in the nebuliser was 4.22MBq, only 0.31kBq was captured on the fourth (outermost) filter. In this experiment, the initial activity in the nebuliser was 477.45MBq, with only 2.3kBq captured on the outermost filter. Moreover, the pump filters captured very little activity, which came as no surprise as the ROIs drawn around the pump end of the phantom cylinders has no activity uptake (Fig 9). It is evident from this experiment that, the [18F]-FDG nebulisation procedure is a safe procedure with no inhalation risk to the operators. In the human pilot study, the phantom will be replaced by with the nebuliser mouth peace with a nose clamp to prevent the escape of activity to the surrounding environment. The filters in the exhaust filter cover will capture the exhaled activity progressively. The operator will be responsible for turning the nebuliser on and off after the nebulisation procedure prior to the imaging procedure.

3.2.4.5 Conclusion

The Phantom set up was proven to be airtight when using a low amount of activity (4.22MBq) and does not the posed any risk of airborne radiation exposure. This is supported by having no contamination within the bag or the scanner room. Although, this experiment may have proven the feasibility of radioactive inhalation procedure. However, as the amount of radioactivity in the nebuliser increases so does the activity deposition on the filters and probably will pose the risk of airborne contamination. Further testing with more relevant clinical radio-activity dose to ensure that there is no radiation hazard to the operator will be conducted.

3.2.5 Determination of activity concentration

3.2.5.1 Overview

It is not understood whether [18F]-FDG is nebulised the same way as the water molecules or they both nebulised at a different rate. The aim of this experiment was to investigate any change in [18F]-FDG activity concentration after the experiment. This will provide a better understanding of the behaviour of [18F]-FDG in aerosol form. Knowing the change in activity concentration will help to accurately calculate the amount of activity nebulised after the nebulisation procedure.

3.2.5.2 Method

About 0.5mL from the residual activity (from the order vial before nebulisation) and 0.5mL from the nebuliser after nebulisation procedure were collected immediately after the nebulisation procedure. These 2 pre and post nebulisation samples were analysed to ascertain the change in activity concentration. Sample counter was used to analyse these sample using 18F window repeatedly for about 10 hours. The area within the linear regions was used to derive the change in activity concentration. 4.22MBq of [18F]-FDG was used in the initial experiment. The same procedure was repeated in all of the experiments to ascertain the change in activity concentration in each nebulisation procedure. However, the amount of activity increases to 800-1200MBq in all of the subsequent nebulisation procedures. As a result of high amount of activity involved (800-1200MBq), the samples were kept for 24 hours after the nebulisation procedure before the analysis to allow significant decay of activity. Count-rate was correlated with activity at the time of count-rate analysis by using the activity in the nebuliser at the time of nebulisation procedure and the activity expected in the counter-tube at the time of the count-rate analysis. All activities were decay corrected to the nebulisation time. Activity concentration was calculated by dividing the activity dispensed into the nebuliser with its volume. To calculate the activity nebulised after one-minute; activity concentration (AC) was multiplied by the change in activity concentration (ΔAC) in the nebuliser after nebulisation procedure, multiplied by one minus volume loss (1-Vol loss) after one-minute nebulisation procedure [(AC*ΔAC) * (1-Vol lost)].

$A = (\mathrm{AC} * \Delta\mathrm{AC}) * (1 - \mathrm{VL})$ ……Equation 1

A=Activity Nebulised after one-minute nebulisation

AC=Activity Concentration

ΔAC= Change in Activity Concentration

VL= Volume lost

The volume lost from the nebuliser was calculated by weighing the nebuliser before and after the nebulisation procedure. The final nebuliser volume was subtracted from the initial volume.

3.2.5.3 Results

The pre and post-nebulisation samples results from the initial experiment produced linear regions with activity <200KBq) (Fig 10 and Table 2). The regions above 200KBq do not appear to fit in the linear trend line. One region within the linear regions was taken as a reference point for comparison between the 2 samples (pre and post nebulisation samples). The same procedure was repeated in each experiment to identify the average change in activity concentrations. The average increase in activity concentration in 10 experiment was calculated to be 14% ± 11%.

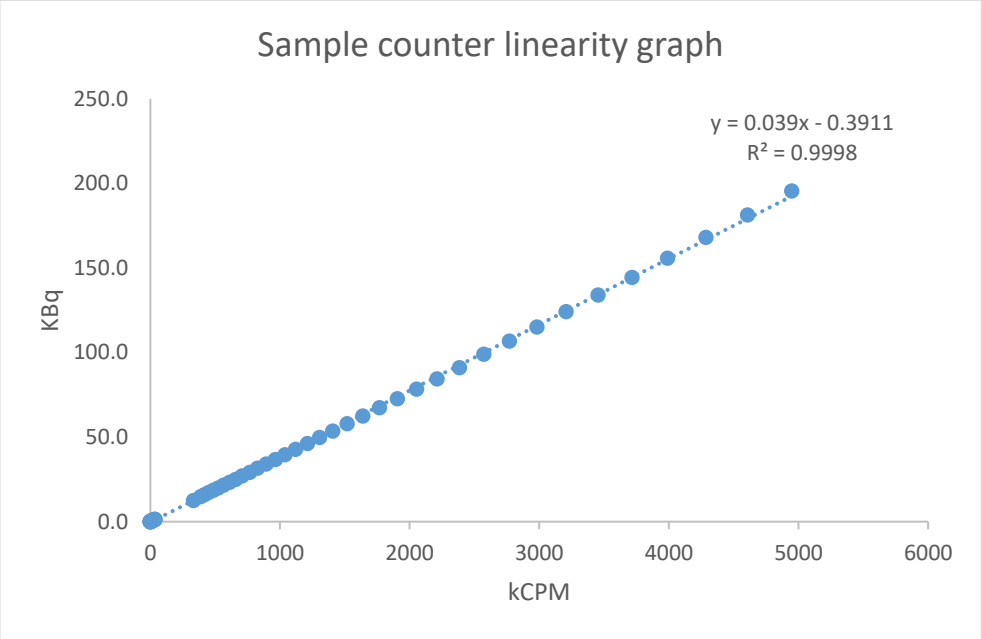

Fig 10: Two samples of activity (18F-FDG) 1 mL each was taken before and after nebulisation procedure. The samples was counted using gamma counter in order to calculate change in activity concentration. The change in activity concentration was plotted in kilo Becquerel (kBq) against kilo count per minute (kCPM).

Experiment	**Amount in the nebuliser (MBq)**	**Change in AC**	**Amount nebulised (MBq)**	**Volume dispensed into the nebuliser (ml)**
EXP1	477.31	0.02	48.75	2.1

EXP2	662.46	0.21	59	1.93
EXP3	722.18	0.21	62.41	1.99
EXP4	1180.44	0.24	92.66	2.11
EXP5	1009.89	0.14	89.81	2.1
EXP6	909.96	0.02	97.44	2
EXP7	937.95	0.20	82.27	2.1
EXP8	1052.81	0.07	108.09	1.97
EXP9	1000.28	0.33	73.43	2
EXP10	925.66	0.01	98.47	2.02
Mean	**887.894**	**0.14**	**81.233**	**2.03**

Investment	₦ 60,000,000.00			
Revenue per month	₦ 6,000,000.00			
Runing cost	₦ 1,500,000.00	₦4,500,000.00		
Hospital	30%	₦1,350,000.00	₦16,200,000.00	
Investor	45%	₦2,025,000.00	₦24,300,000.00	
Foresight	15%	₦675,000.00	₦8,100,000.00	₦81,000,000.00
Maintainance	10%	₦450,000.00	₦5,400,000.00	
	100%			

Table 2: This is showing the initial amount of activity dispensed with the corresponding volume into the nebulisation and the amount nebulised after 1-minute nebulisation procedure and change in activity concentration (AC) at the end of the nebulisation procedure. From our cold experiment, we know the volume nebulised in 1 minute is 0.21mL.

3.2.5.4 Discussion

There is massive variability in the change in activity concentration between the experiments, there are many variables to explain the variability such as; variation in venting the pump; quantification method, the initial activity and

volume dispensed into the nebuliser. The operator mimics his tidal breathing while venting the pump, the ventilation was between 16-18 ventilation per minutes depending on how fast the operator breathes and how quick and hard the pump is drawn. There were no standard tools to draw Region of interest (ROIs) within the phantom; ROIs were drawn manually on the phantom images. The amount of [18F]-FDG and the volume dispensed is different in each experiment.

3.2.5.5 Conclusion

Using the several parameters such as; activity concentration at the time of nebulisation, change in activity concentration after the nebulisation procedure and volume loss after one-minute nebulisation has provided the idea of the amount of activity nebulised after one-minute nebulisation. This gives an idea of the amount delivered to the patients.

3.2.6 Determination of PET-CT Scanner Sensitivity

3.2.6.1 Overview

Although, the department perform quality control of the scanner as a routine procedure. For the purpose of this experiment, several images of the phantom were conducted to select the best quality image, keeping the procedure under ALARP (As Low As Reasonably Practicable) principle.

3.2.6.2 Method

The lung phantom (Fig 7) was used for this experiment. 3 sequential images of the phantom were taken, starting with topogram; 35mA, 120kV, 10.4 second scan time, 0.9 mm slice thickness and 2 second delay time. Followed by an attenuation correction CT WB 3.0 HD_FoV; 45 Eff mAs, CARE Dose4D, 120kV, 18.56s scan time, 2s delay with 3mm slice thickness. The emission PET images were carried out following the completion of the CT in list mood. The images were reconstructed for 1 to 20 minutes in the interval of 1 minute to quantify the level of noise (standard deviation) per bedtime. The images were reconstructed using ordered-subsets expectation maximization (OSEM) algorithm with 2 iterations and 21 subsets whilst PSF + time-of-flight was enabled and Gaussian filter 6.0 mm were used. Both attenuation and scatter correction was incorporated in the reconstruction protocol. All the images were quantified by drawing a propagated ROI around

the total area of uptake to produce a VOI along the trans-axial plane. The standard deviation of the activity concentration (kBq/ml) against reconstructed scan time was plotted to ascertain the level of noise.

3.2.6.3 Results

No significant difference in image noise was found between the range of scanning time used in this experiment (i.e 1- to 20 minutes scan time per PET bed) (Fig 11).

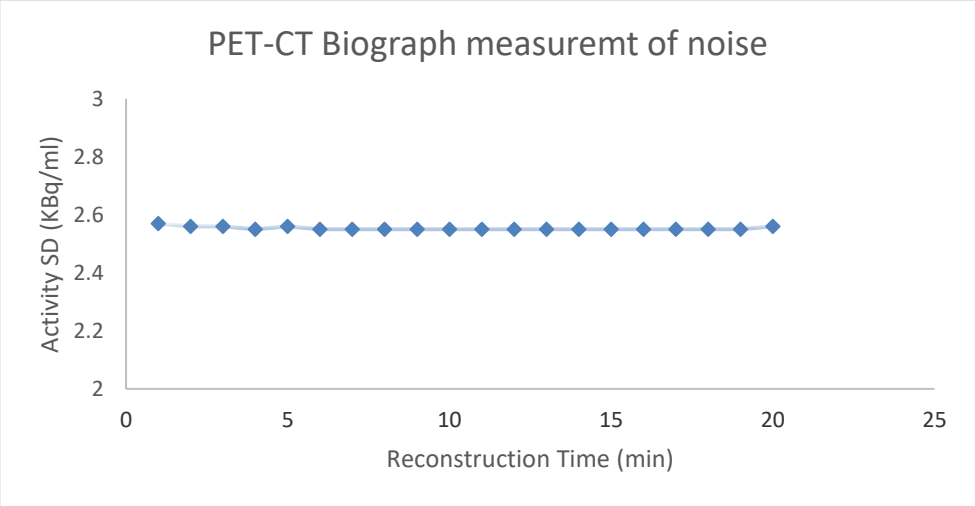

Fig 11: Image reconstruction data demonstrating the level of noise. This indicate that scanning for shorter or longer time does not add any benefit, as such, the scan time was restricted to 4 minute to avoid going faster acceptable clinical time of 0.5 seconds per bed position.

3.2.6.4 Discussion

The level of noise appeared to be quite similar between 1 and 20 minutes' reconstruction time. The imaging for a long duration of time adds no benefit to the patients in terms of noise reduction. Therefore, the phantom imaging time, as well as the lung section of the human volunteer for the clinical pilot study, was restricted to 4 minutes. The choice of 4 minutes was made to avoid going faster than the normal clinical speed of 0.5 seconds per bed position.

3.2.6.5 Conclusion

The longer reconstruction time does not add any advantage to the imaging quality. Therefore, the reconstruction of the phantom images was restricted to the normal clinical speed of 0.5 seconds per bed position and as such; it

took 4 minutes reconstruction time to go through the phantom in 4 minutes (the phantom length is 8 bed position).

3.2.7 Quantification of lung Phantom PET-CT Imaging

3.2.7.1 Overview

Previous experiments lead to a better understanding of the behaviour of the aerosolised [18F]-FDG and provided a way of quantifying the aerosol deposition within the phantom. More experiments with the same phantom setup were conducted in order to calculate the activity distribution within different section of the phantom. The phantom was built in such a way that it can represent the human lung in terms of volume and density. The total volume of each Perspex cylinder was 3L and the sponges were tested to have similar density as the lung tissue with similar uptake of Tc-99m liquid tracer and Kr-81m gas from the previous experiment [43]. The sponge was expected to behave the same way with aerosolised [18F]-FDG.

3.2.7.2 Method

The empty syringe was weighed using Kern ACS 80-4 Analytical Balance Scales (Fig 5) before and after dispensing activity into it, to calculate the volume of activity dispensed. The syringe was also weighed after dispensing the activity into the nebuliser to measure the residual. The activity dispensed into the nebuliser was 2mL ± 0.07; the nebuliser contained a range of activity from 679.3 to 1096.5MBq with an average of 887.9MBq of activity. The remainder of the activity was kept in the vial for about 24 hours after the imaging procedure to allow radiation decay. The sample was collected from the residual to measure the changes in activity concentration. One-minute nebulisation procedure was conducted as described above and the imaging procedure was conducted using the imaging protocol below. At the end of each of these experiments, filters were removed to ascertain the level of deposition. The image quality was assessed qualitatively by 2 experienced radiologists who ae not part of the study.

3.2.7.2.1 Image acquisition protocol

Images were acquired a few minutes after the nebulisation procedure on a dedicated combined PET/CT scanner (Biograph mCT PET-CT Flow technology). In total 3 sequential images of the phantom was taken, starting

with topogram; 35mA, 120kV, 10.4 second scan time, 0.9 mm slice thickness, 2 second delay time and 500 FoV. Followed by an attenuation correction CT WB 3.0 HD_FoV; 45 Eff mAs, CARE Dose4D, 120kV, 18.56s scan time, 2s delay with 3mm slice thickness. The PET images were acquired in a 3-dimensional mode using Continuous Bed Motion (CBM) with speed of 0.5mm/second over the phantom region (equivalence to 4 minutes per bed position). The images were reconstructed using ordered-subsets expectation maximization (OSEM) algorithm with 2 iterations and 21 subsets whilst trueX + time-of-flight was enabled and Gaussian filter 6.0 mm were used. Both attenuation and scatter correction was incorporated in the reconstruction protocol.

3.2.7.2.2 Image Analysis

The region of interests (ROIs) were drawn throughout the entire length of the tubes connecting the nebuliser to the phantom and the nebuliser end of the phantom (Fig 12). Using Mirada imaging software (BDx). The image of the entire phantom set-up has revealed no uptake from the distal end of the phantom cylinders and the pump (Fig 13).

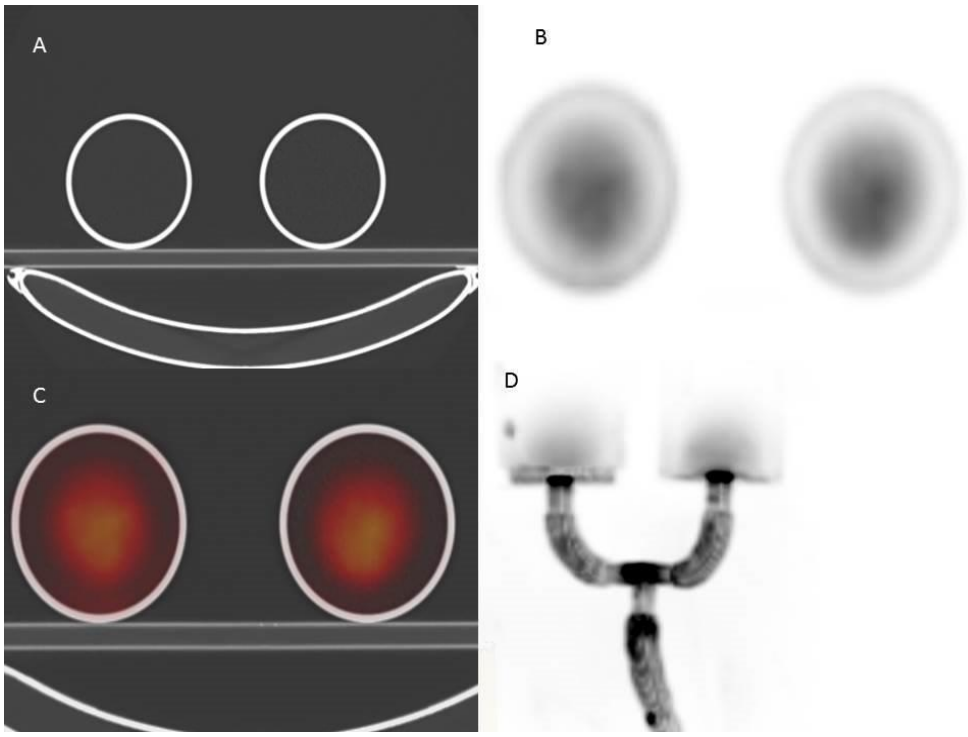

Fig 12: Axial slices CT (A), PET (B), Fused PET-CT (C) and MIP (D), the slices demonstrated the Deposition of radioactivity within the phantom

cylinders, along the tubes. The side of the phantom cylinder closer to the pump was not considered for quantification as no deposition of activity was found to the end of the cylinder.

3.2.7.2.3 Defining ROIs within the lung

The phantom cylinder is 10cm in diameter and the tube is 3cm in diameter. Manual ROIs covering the whole of the phantom and tubes' diameter was drawn slice by slice to generate one volume of interest (VOI) covering the part of the phantom with radio-activity uptake.

3.2.7.2.4 Quantifying radioactivity in the defined lung ROIs

The entire diameter of the trans-axial slice of the phantom cylinder on the CT images was considered as a Volume of interest (VOI), Manual ROIs were drawn throughout the regions of the cylinder with 18F-FDG uptake (Fig 15). The region of the phantom with [^{18}F]-FDG uptake was isolated by drawing a 10cm axial ROIs covering the entire diameter of the cylinder. The section of the cylinder with no uptake (Fig 9) was identified. Region less than 0.1Bq/ml was excluded. Total mean activity concentration (Bq/ml) was taken from each phantom region (cylinders and tubes). Consequently, the activity in Becquerel was determined by multiplying the average activity concentration per Volume of interest [188].

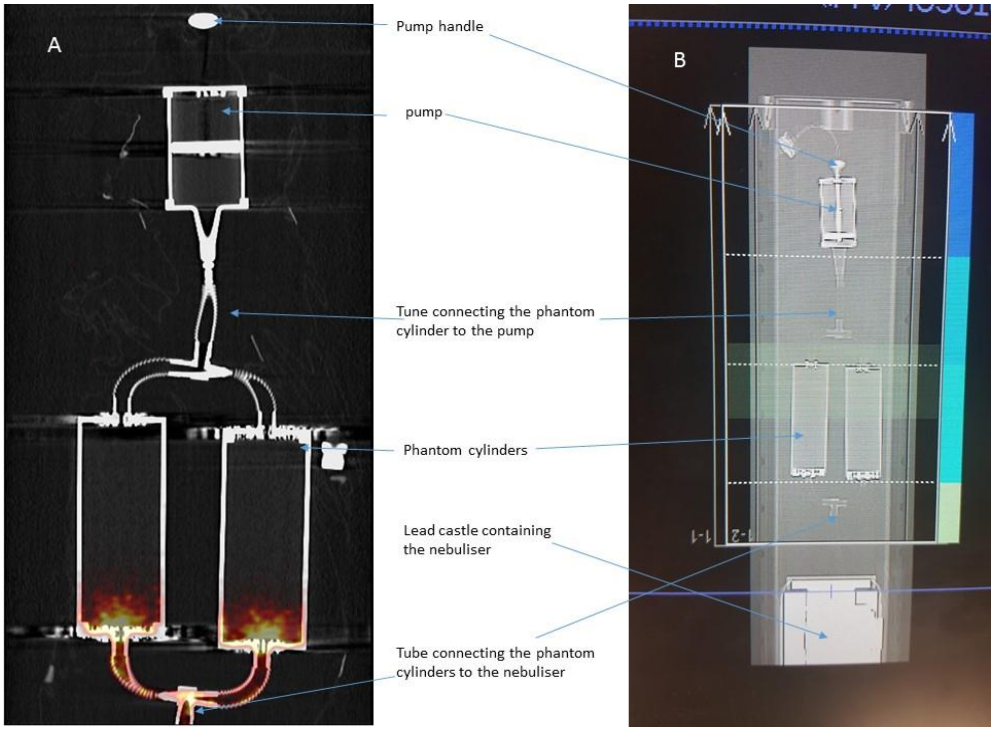

Fig 13: The image of the entire set-up (A) demonstrating uptake at the nebuliser end of the phantom cylinders and the tube connecting the nebuliser to the cylinders. The phantom set-up during the PET imaging (B).

3.2.8 Dosimetry and risk calculation

3.2.8.1 Radiation Dosimetry for a CT scan

Acquisition of a low-dose CT scan from the CT in a hybrid PET-CT scanner will result in additional radiation exposure to the subject. A typical effective dose from a low-dose CT scan of the chest acquired using tube current settings between 30 and 50mAs ranges from 1.1 to 1.8 mSv (3) compared with the average routine adult chest CT dose of 5.5-7.8 mSv, taken at a setting of 168mAs. The CT and PET doses are additive. The risk to the subject from these combined procedures may still fall within the LOW-risk category.

3.2.8.2 Radiation Dosimetry for PET Scans using inhaled 18F-FDG.

The calculation used in Dolovich and Bailey [110] was adopted for this experiment. The formula is stated below;

Dose = $1.443 \times S \times A \times t_{1/2} \times 10^3$ mSv

where S = dose constant (MIRD pamphlets[a]), Sv/MBq-hr

A= radionuclide amount in MBq

$1/t_{1/2eff}$ = effective half-life = $1/t_{1/2physical} + 1/t_{1/2biological}$, hr

1.443= ‘‘mean life’’ for exponential decay

10^3 = conversion factor to mSv

For Effective Dose radiation calculation with lung as source of radioactivity and ^{18}F as the radionuclide: $S_{\text{Whole Body}}$ (SWB)= 1.8×10^{-5} Sv/MBq-hr

A= 8.31 MBq (0.22 mCi) inhaled

$t_{1/2eff}$ = 0.9 hr, assuming biological half-life =physical half-life

Radiation Dose per PET scan with inhaled 18FDG

$D_{eff} = 1.443 \times 1.8 \times 10^{-5} \times 8.31 \times 0.9 \times 10^3$

= 0.2mSv/PET scan

3.2.8.3 Results

The radioactive nebuliser output of [18F]-FDG was found to increase as the initial activity in the nebuliser increases. In another word, the higher the activity in the nebuliser before the inhalation procedure, the higher the

deposition within the phantom. These findings were similar in the cold experiments (Fig 14).

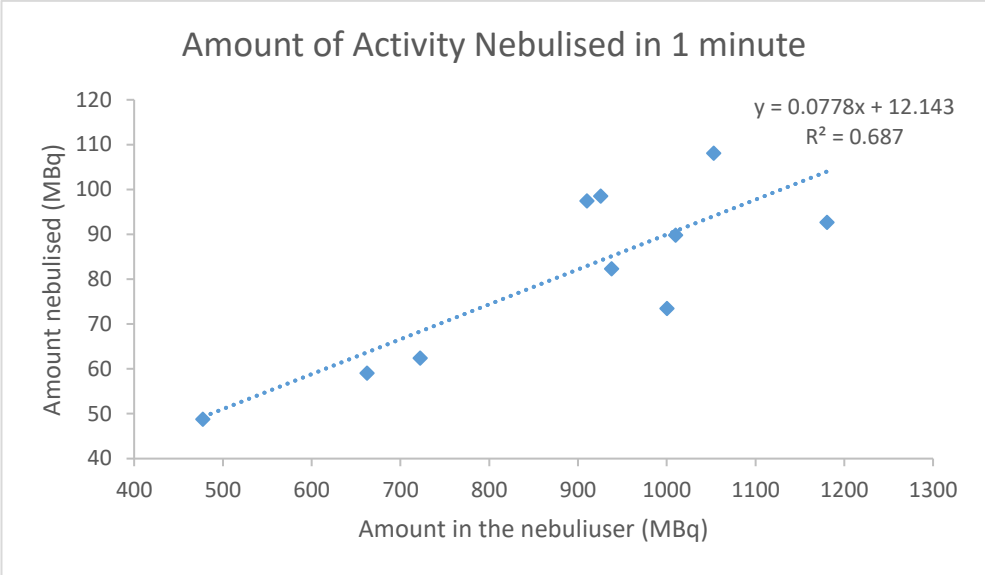

Fig 14: The deposition of radioactivity within the phantom set up versus the activity dispensed into the nebuliser before the experiment. This demonstrates the efficiency of the nebuliser.

The radioactivity was not homogenously distributed within the phantom, due to the short period of nebulisation procedure and pump volume capacity (Fig 13). The maximum pump capacity is 500ml (equivalent to human tidal volume)

The overall activity deposition within the phantom; cylinder and the extra-pulmonary section of the tube were 8.31 ± 4.04MBq. The deposition within the cylinder (lung surrogate) was 6.45 ± 2.97MBq. The average total internal radiation dose (phantom cylinders and the extra-pulmonary section of the tube) see section 3.2.3 (Dosimetry and risk calculation) was 0.2mSv (Tab 3, Fig 15).

The activity captured on the first nebuliser exhaust filter (the inner filter) was 275.59 ± 72.19KBq, the amount captured on the second filter was 60.93 ± 50.75kBq while the third and fourth filters have 15.24 ± 22.37kBq and 3.05 ± 1.80kBq respectively. The pump filters, however, has no significant depositions, with the inner and most external filters have 0.24 ± 0.20 and 0.20 ± 0.15kBq respectively (Tab 4). The experiment was also conducted within a

bag with no contamination detected within the confine of the bag (Fig 16). The quality of the images was assessed qualitatively by 2 experienced radiologists within the department who are not part of this study.

Amount of Activity in the nebuliser and tube after 1 minute nebulisation				
EXP No.	**Amount nebulised (MBq)**	**Phantom Cylinder (MBq)**	**Ext Pulmonary Tube (MBq)**	**Cylinder and Tube (MBq)**
EXP 1	48.75	4.23	0.61	4.84
EXP 2	59.00	5.65	0.99	6.64
EXP 3	62.41	4.83	1.03	5.86
EXP 4	92.66	13.83	4.13	17.96
EXP 5	89.81	4.53	1.33	5.86
EXP 6	97.44	9.25	3.14	12.39
EXP 7	82.27	5.52	2.24	7.77
EXP 8	108.09	4.83	1.19	6.02
EXP 9	73.43	6.70	2.59	9.29
EXP 10	98.47	5.12	1.32	6.44
Mean	**81.23**	**6.45**	**1.86**	**8.31**
SD	**19.58**	**2.97**	**1.13**	**4.04**

Table 3: the quantification of the activity deposited within the phantom Cylinders and the tube, showing around 11% of the activity being nebulised after one minute nebulisation.

Deposition of radio-activity on various filters (kBq)									
Amount of activity	**Neb F1**	**Neb F2**	**Neb F3**	**Neb F4**	**Pump F**	**Pump 1**	**Pump 2**	**Pump 3**	**Pump 4**
EXP1	178.4	1.32	2.83	2.31	0.24	0.08	0.17	0.15	0.15
EXP2	212.9	1.55	3.27	2.64	0.28	0.21	0.20	0.18	0.17

EXP 3	189.35	3.68	3.59	3.75	0.38	0.32	0.34	0.36	0.34
EXP 4	342.57	156.36	3.49	1.16	0.77	0.71	0.73	0.71	0.63
EXP5	399.7	19.77	2.86	4.16	0.16	0.12	0.08	0.03	0.04
EXP6	314.2	108.8	61.36	4.05	0.06	0.05	0.04	0.04	0.05
EXP7	271.3	93.99	52.98	3.47	0.05	0.05	0.04	0.04	0.04
EXP8	279.9	111.0	9.56	1.65	0.04	0.03	0.04	0.04	0.04
EXP9	236.1	18.20	2.31	0.56	0.01	0.01	0.02	0.02	0.02
EXP 10	331.36	94.48	10.11	6.78	0.00	0.00	0.00	0.00	0.00
Mean	**275.5**	**60.93**	**15.24**	**3.05**	**0.20**	**0.16**	**0.17**	**0.16**	**0.15**
SD	**72.1**	**57.7**	**22.3**	**1.80**	**0.24**	**0.22**	**0.22**	**0.22**	**0.20**

Tab 4: the deposition of the aerosolized radio-activity on the nebuliser exhaust filters and pump filters. This has provided an indication that the system is air tight.

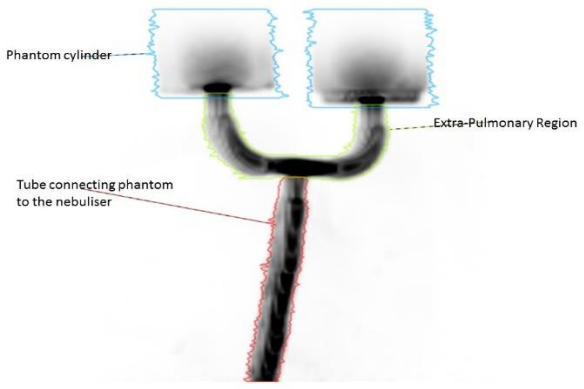

Fig 15: Manual axial ROIs covering the tube connecting the nebuliser to the cylinders and the nebuliser end of the cylinder evident to have uptake of activity.

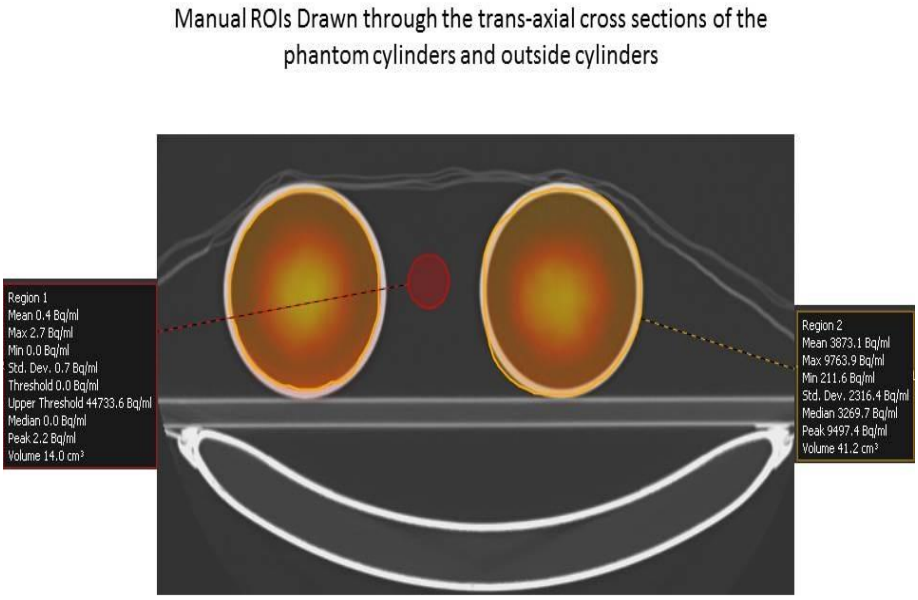

Fig 16: Manual ROIs drawn through a trans-axial slice of the phantom cylinders with another ROI drawn outside the cylinder but within the bag indicating no radiation contamination within the bag even when using high amount of activity

3.2.8.4 Discussion

The nebuliser output has consistently been confirmed to be linear using cold as well as the experiments. The deposition pattern within the phantom was found to be within the proximal one-third of the phantom cylinders and more intense at the centre of the cylinders (Fig 16). It is expected that the distal part of the phantom cylinders to be void of the deposition due to the nature of the experiment. These experiments were based on human tidal volume, which in a healthy adult only allowed entry of 500mLs of aerosol into the lungs. The phantom cylinders are 1.5Ls each connected to a 500ml pump and tidal breathing only allow 250mLs of each phantom cylinders.

Although it was not practical to measure the amount of activity in the nebuliser after the nebulisation procedure. The amount of activity dispensed was calculated by measuring the volume lost when the radioactivity decayed.

The average percentage nebulised radio-activity was calculated to be 9% [(81.23/887.89)*100] (Tab 3) which means about 90% of the activity remained in the nebuliser after one-minute nebulisation procedure. By quantifying the deposition within the phantom and filters, an average of 9.2% of [^{18}F]-FDG was found to be deposited into the phantom system.

Although the amount of activity (887.9MBq) dispensed during this experiment was much higher than the activity used in the initial experiment (4.22MBq), despite the increase in the amount of radio-activity in the nebuliser, no radiation contamination was detected within the scanner room or the pump filters after the one-minute nebulisation procedure. This is a strong indication that the safety of this procedure, moreover, the average amount of activity nebulised after one-minute nebulisation was less than 10 MBq far less than the recommended intravenous radio-activity administered in routine clinical procedures (125-740MBq) [189]. The internal dose to the patients for having the combine PET-CT procedure is estimated to be 2mSv which is below the internal dose for having a routine Chest CT scan of 5.5-7.8 mSv depending on the weight of the patient and is also below the annual radiation dose limit of 2.7 mSv in the UK.

3.2.8.5 Conclusion

This experiment has successfully provided the valuable clue to the human clinical trial. The nebulisation time, amount to be dispensed into the nebuliser as well as the patient internal dose were all provided.

3.3 General discussion

Following inhalation therapy, only a fraction of the dose reaches the expected target area. Knowledge of the amount of drug actually deposited within the lung parenchyma is essential in designing the delivery system or devices to optimize the delivery efficiency to the targeted region of the respiratory tract. This knowledge is essential in developing a dosing regimen to deliver the required amount of active compound to the patient.

Mechanism of aerosol deposition and distribution depends on many factors, such as; macro- and microstructure of the airways, breathing patterns,

aerodynamic particle size distribution and inhalation drug delivery devices technology [190-192]. Pulmonary drug delivery can be tested by in vitro, ex vitro lung tissue models as well as in vivo models, the in vitro models includes; Multistage cascade impactors, Cell Culture Models as well animal models whereas in vivo models includes; imaging and small animal models methodologies [56]. Despite the advantages of imaging modalities, invasive in vivo approaches in small animal remains the gold standard by acquiring direct pharmacokinetic data [78].

Each of the models is not without any limitation, the pharmacokinetic analysis measured drug deposition outside its primary deposition location. It is a measurement of drug that has undergone diffusion, absorption and mucociliary clearance. On the other hand, Cascade impactor method is not truly representative of patient inhalation conditions [53, 193].

Radionuclide imaging techniques provide a direct measurement of in vivo deposition [35, 39, 55]. Planner and SPECT imaging have been used for many years to study the mechanism of drug delivery in the lung. Technetium metastable (^{99m}Tc), Iodine (^{123}I) and Indium (^{111}In) are the radio-isotope use in the planner and SPECT imaging and radiolabelling those isotopes are straightforward and have long half-lives to allow for the quantification imaging [32, 83, 102, 194]. However, gamma scintigraphy are inherently busy images and like all 2D imaging suffer superimposition of the images, as such; it is difficult to quantify the regional distribution of the drugs [83]. SPECT imaging, on the other hand, is 3D imaging and has added the advantage of providing increased information on the regional distribution of the drug. However, the imaging technique requires longer acquisition time than planer imaging [39, 83].

PET isotopes, unlike SPECT isotopes, are biologically active molecules and PET imaging demonstrate increased accuracy and improved sensitivity compared to SPECT imaging [39]. It is faster and has better attenuation correction measures. Despite the enormous advantage of PET-CT imaging over gamma scintigraphy and SPECT, PET imaging has rarely been explored for pulmonary drug development [116, 195]. This could be due to lack of

availability of the PET scanner in many centres. The PET imaging will provide the opportunity to quantify regional distribution with better accuracy that SPECT imaging and allow examination of drug distribution as a function of time [110, 116]. In this study, we employ the use of [^{18}F]-FDG in the aerosol form by using the nebuliser. Other PET tracers such as 11C Triamcinolone Acetonide, ^{68}Ga Aerosol (Galligas), ^{68}Ga-Labeled Macroaggregated Albumin as well as [^{18}F]-Fluticasone propionate has been used in the pass [196-198].

To our knowledge, this is the first phantom imaging experiment done to study the feasibility of inhalation of [^{18}F]-FDG to investigate the mechanisms of pulmonary drug delivery and distribution.

Radiation safety, radiation dose as well as the acquisition time for the human studies have been established by this phantom experiment. The amount of aerosolised [^{18}F]-FDG required in the lung to produce a clinical level PET imaging is far less than the amount used in standard clinical imaging [189]. For a patient to undergo a standard clinical PET imaging an average of 3·7MBq per kg bodyweight of [^{18}F]-FDG will be injected intravenously. In other words, a 70kg person required an average of 256MBq of intravenous [^{18}F]-FDG to perform a clinical procedure. Although the amount of radioactivity dispensed into the nebuliser was between 800-1200MBq only about 10MBq is nebulised after one minute. The total internal dose to the phantom was about 8MBq, which is far less than the 256MBq in clinical imaging. After repeated experiments, this dose (8MBq) is believed to be enough to produce PET images with a good signal-to-noise ratio (SNR).

Although the phantom images were not designed to quantify the regional distribution, it was meant to provide an understanding of the overall deposition. The distribution of the [^{18}F]-FDG within the phantom was observed to be more central than the periphery of the phantom; this is probably due to inertial impaction which is the predominant mechanism of deposition along the upper respiratory tract [191].

There was significant [^{18}F]-FDG uptake on the tube connecting the 2 phantom cylinders, this was not unexpected as high uptake was recorded previously in

the oral cavity and upper respiratory tract [102, 199]. The sponge does not equate to human lung due to lack of other anatomical structures and physiological functions. Apart from the particle size distribution of the drug molecules and the functions of the aerosol delivery devices, the physiology and the anatomy of the lung play significant role in drug distribution within the lung. Lack of physiological functions in the sponge is the biggest limitation of this experiment, moreover, the sponge and the lung varies structurally which may have implication in the pattern of distribution between the two. The distribution of the activity within the sponge is based on the principle of inertial impaction which allow the particle with enough inertia to impact on the surface whereas the smaller particles continue to move in the direction of the follow of the streamlines.

It is not surprising that the distribution pattern of the activity within the sponge was more in the centre of sponge than the periphery. This is expected because the direction of the flow of the streamline was to the centre of the phantom. The mechanism of the distribution of the activity towards the periphery of the sponge is highly unlikely to be due to inertia but very likely to be as a result of simple diffusion. As compared to human lung, the distribution of aerosol is based on inertial impaction, diffusion and sedimentation [191]

The phantom studies could not account for the complex physiological factors responsible for aerosol depositions along the airways. However, it helps in understanding the administered dose for one-minute nebulisation procedure and to designing a standard protocol for the subsequent human pilot study.

The guidelines for using PET to determine the quantity and distribution of inhaled therapeutics are produced recommended 800-2500MBq of activity into the nebuliser before the venting procedure [108]. These were aimed to deliver 10-50MBq into the lung within one to one and a half minutes nebulisation procedures. In this experiment, the nebulisation procedure was conducted in one-minute with the initial activity ranging from 679.3 to 1096.5MBq inside the nebuliser. The average initial activity in the nebuliser before the nebulisation procedure was 887.9MBq with the average lung

(phantom cylinder) deposition of 6.45MBq. Increasing the initial activity in the nebuliser to 2500MBq may result in delivering of about 18MBq into the lung surrogate. To deliver the minimum 10MBq of activity into the lung as suggested by the guideline [108], the initial activity in the nebuliser needs to be 1400MBq. This was predicted by our phantom experiment (Fig 6 and 14). Although the guideline was based on the human lung deposition with different scatter characteristics to the phantom, attenuation correction will account for the differences. These experiments were designed to provide a rough idea on the feasibility and the safety of the inhalational procedure and to also understand the topical distribution of inhaled therapies in the lung using radionuclides and imaging and also to estimate patient internal dose. These experiment will pave the way to gaining approval from Administration of Radioactive Substances Advisory Committee (ARSAC) to conduct a human clinical trial in the UK as this procedure has not been done in the UK before and it has also not been standardized in human.

The particle sizes produced in this experiment are likely to be within adequate mass median aerodynamic diameter (MMAD) capable of penetrating the lower respiratory tract [200]. However, the deposition within the phantom is likely to be due to inertial impaction rather than sedimentation and diffusion. According to the nebuliser manufacturers, PARI LC nebuliser produces the total Output Rate (TOR) of 500 mg/min with MMD of 3.5 µm and Percentage Respirable Fraction (%RF) of 68 %. The advancement in nebuliser and imaging technology could mean achieving a high image quality with a low amount of activity delivered into the lung at a shortest possible time.

There was no much difference between the activity on the 4th exhaust filters when the initial nebuliser activity was 4.22MBq and when it was it was 887.89MBq (0.31 ± 0.151.80kBq and 3.05 ± 1.80kBq). These indicate no further risk of inhalation risk to the operator and the bystanders when the activity in the reservoir (nebuliser) increased prior to the nebulisation procedure. Moreover, there was no any contamination detected in the scanner room to suggest escape of activity to the surrounding in all of the experiments.

Although in the human pilot study, the 30cm tube connecting the nebuliser to the phantom cylinders will be connected to the mouthpiece and attached directly to the subjects' mouth, nose clip will be provided to prevent escape activity through the nostrils. The exhaled activity will be captured by a set of filter pad within the exhaust filter cover allowing only the air to escape to the surrounding environment.

As the average amount activity deposited in the tubes and phantom cylinders was calculated to be 8.31 MBq (0.22 mCi) at the effective half-life ($t_{1/2}$eff) of 0.9 hr (assuming biological half-life =physical half-life). The patient internal radiation dose is calculated to be 0.2mSv/PET scan. For comparison purposes, the dose from a single abdominal X-ray projection is 0.7 mSv [201] and the average annual radiation dose in the UK from background radiation is approximately 2.7 mSv [202]

3.4 Limitation

The sponges used in the phantom is only representative of density, presenting similar uptake of [18F-FDG as seen in the lung. However, it was unable to mimic other physiological activities within the lung. The quality of images in the phantom does not take into account the image quality degradation due to tissue and motion artefacts.

3.5 Conclusion

The overall experimental procedures have provided a better understanding of the behaviour of aerosolized [^{18}F]-FDG. This understanding is essential in planning human pilot study. The understanding of the duration of the nebulisation procedure, the amount of activity required to conduct the procedure, the amount of radio-activity coming out of the nebuliser after one-minute nebulization as well as the radiation safety of conducting the procedure. The idea of the patient internal dose has also been establish in this experiment. Although the phantom cannot be an absolute replica of human lung, this experiment has provided us with the basic understanding of the behaviour of [^{18}F]-FDG in aerosolized form. It has paved the way for our human pilot study.

Chapter 4 Radiolabelling of the Fostair p MDI with positron emitting radionuclide (Fluorine-18 or Gallium-68) for inhaled drug particle lung deposition study by using Anderson cascade impactor

4.1 Background

Conventional gamma camera images of lung deposition are familiar tools for the visualisation of drug delivery of inhaled medication. Such images are "fuzzy" and lack the clarity necessary for quantification. These limitations are inherent in the physical attributes of the technology. Recently an alternative methodology has been introduced into clinical practice known as Positron Emission Tomography. This provides precise localisation of the radioactive source and when coupled with contemporaneously acquired CT scan images provide a precise graphic image of the distribution of the radiolabel. PET imaging is widely for localisation of the tumours, but rarely used in lung deposition studies despite its' enormous potentials [39, 83, 116].

The key advantages of PET over SPECT/ gamma scintigraphy are the potential for quantitation and the high sensitivity [35, 102, 116]. From a technical perspective, these properties are due to the positron annihilation generating 2 gamma photons that can be correlated and paired, hence the lack of requirement for collimation. Time of flight analysis is also possible in clinical PET- this cannot be done with SPECT [110]. A further major advantage is that we have a range of PET isotopes with different half-lives (i.e. gallium-68, half-life 68 minutes; fluorine-18, half-life 110 minutes; copper-64, half-life 12.7 hours) which could allow different imaging protocols with the pMDI and NEXThaler products [39, 197].

4.2 Aims and Objectives

The aim of this study is to demonstrate the ability of PET/CT in quantifying lung deposition of inhaled drug particles, enable the precise localization of that deposition within the airways, and to provide information on the kinetics

of drug transport within the airways. The study is categorized in 3 stages: radiolabelling; validation of the radiolabelling and animal inhalation procedure.

4.3 Materials and Methods

4.3.1 Instrumentation

4.3.1.1 Cascade impactor

The cascade impactor is a device developed for aerodynamic size distribution measurements of aerosols. Cascade impactor consist of an aluminium device with 7-8 successive stages and the inlet, with a metal collection plate in-between the stages, airflow meter and a suction pump. Each stage of the impactor has round holes or rectangular slits orifices and the size of the orifices reduces in descending order until the final stage [58]. Airflow meter is used to measure the flow rate within the impactor, whereas the pump is used to draw the aerosol through the impactor at a particular pressure. The aerosol passes into the impactor through a series of orifices with a collection surface placed perpendicular to the direction of flow.

In order to get to the next stage of the cascade impactor, the particles must remain in the direction of follow of the air streamline. As the airflow approach the collection plate the flow bend at right angle to the collection plate. Larger particle are unable to follow the direction of the air streamline, as such impacted on the collection plate. Due to the decreasing size of the orifices, the speed of the air stream increases as the aerosol progress to the last stage of the impactor, the average size of particles collected on each stage are smaller than the preceding stage. The end stage of the cascade impactor usually has an efficient filter to collect all the smaller particles. At the end of the experiment, the collected particles are washed off for quantification.

The collection efficiency of each stage of the impactor depends on the number of geometric and operational factors, such as; (a) the linear velocities of the air streams (usually described by a hypothetical average, U_o, equal to the volumetric flow rate divided by the area of the opening); (b) the jet opening

shape and size (conveniently described by the jet width for slits or the jet diameter for holes, either of which may be called W); (c) the aerosol particle shape; (d) the particle size (diameter, D, if the particle is spherical); (e) the particle density, p; (f) the slip correction, C(D) (important for smaller particles); (g) the air viscosity, ŋ; (h) the jet-to-collector separation distance, S; (i) the jet throat length, T; and the character of the jet airflow as can be conveniently described by the Reynolds number, N_{Re}.

Andersen cascade impactor (ACI) is one of the commonest cascade impactor model for characterizing the particles emitted from inhalable drug devices (Fig 2). The Andersen cascade impactor differs from many other impactors in that each of its stages has multiple orifices [61]. The flow of air and particles through 1 orifice may affect the flow through an adjacent orifice. Moreover, the previous models of cascade impactors have not considered the performance of the preseparator (inlet/Throat). The aerosol passes through the throat undergo a complex transition from turbulent to laminar conditions, before entering the first stage in an Andersen impactor. This complex transition has not been modelled in the other previous cascade impactors. The typical flow rate use in cascade impactor studies is 60 L/min in dry powder inhalers [6,7], at this rate the effective cut-off diameter for the throat was reported to be 8.7 µm [203]. A conventional ACI like other cascade impactors has multiple stages between 7 and 8 stages, each stage with a target cut-off diameter from 1-8 µm, the procedure is lengthy and tedious. In this experiment, we consider using an abbreviated version of ACI in which some stages are combined to make the operation faster and simpler. Unlike the multistage ACI, the abbreviated ACI consist of only 3 stages, 8-6 µm, 1-5 µm and a filter which is meant to collect particles below 1 µm. the particle between 1 and 5µm are believe to be the particle sizes entering lung parenchyma contain fine particle fraction of the active pharmaceutical products.

There is some evidence to suggest that abbreviated versions of multistage ACI can be used to broadly indicate in vivo lung deposition based on two or three size bands (or fractions):

1. Coarse Particle Mass (CPM) –That portion of the aerosol considered to be too large to be inhaled (usually considered to be >5 microns).
2. Fine Particle Mass (FPM) – That portion between 5 and 1 micron, usually considered likely to deposit deep into the lung and hence be therapeutically effective.
3. Extra-fine Particle Mass (EPM) – That portion below 1 micron, usually considered to be too small to deposit in the lung and therefore exhaled.

4.3.1.2 Gamma counter

Gamma counters are usually scintillation counters. In a typical system, a number of samples are placed in sealed vials or test tubes, and moved along a track. One at a time, they move down inside a shielded detector, set to measure specific energy windows characteristic of the particular isotope. Within this shielded detector, there is a scintillation crystal that surrounds the radioactive sample. Gamma rays emitted from the radioactive sample interact with the crystal, are absorbed, and light is emitted. A detector, such as a photomultiplier tube converts the visible light to an electrical signal. Depending on the half-life and concentration of the sample, measurement times may vary from 0.02 minutes to several hours.

4.3.1.3 Capintec Reader

The capintec dose calibrator is a device that Converts the ionisation current produced by a given radionuclide into current. The capintec reader is capable of measuring a dose as high as 6 Ci (250 GBq) with high accuracy.

4.3.2 Chemicals

4.3.2.1 Beclomethasone Dipropionate

Beclomethasone 17, 21-dipropionate (BDP) is a topically active corticosteroid used in the treatment of asthma and rhinitis. It was first available in 1972 in a pMDI and later in a dry powder inhaler and an aqueous

nasal spray. BDP is actually a pro-drug with weak glucocorticoid receptor binding affinity, that is hydrolysed via esterase enzymes to an active metabolite beclomethasone 17-monopropionate (B-17-MP). Minor inactive metabolites, beclomethasone 21-monopropionate (B-21-MP) and beclomethasone [171], are also formed Rohdewald, Mollman [204], [205]. The chemical structures and relative receptor affinities for BDP and its main metabolites are shown in (Fig 17).

The anti-inflammatory effects of BDP in asthma include modulation of cytokine and chemokine production; inhibition of eicosanoid synthesis; marked inhibition of accumulation of basophils, eosinophils and other leukocytes in lung tissue; and decreased vascular permeability [206].

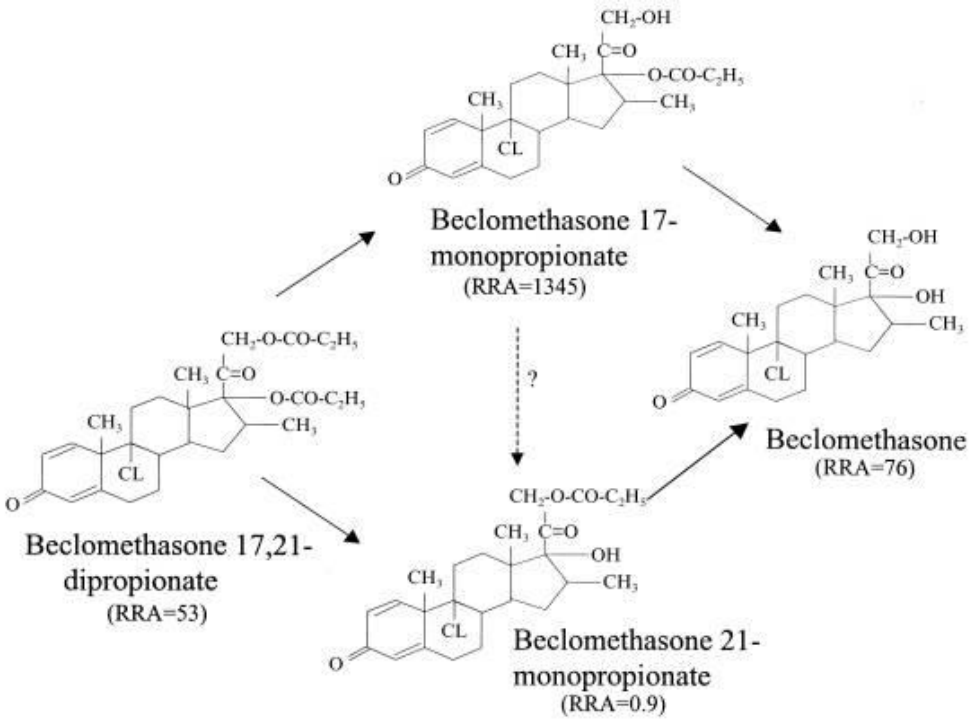

Fig 17: Chemical structures, major in vivo degradation pathway and glucocorticoid receptor affinities relative to dexamethasone (RAA = 100) [207] for BDP and its main metabolites.

4.3.2.2 Formoterol Fumarate Dihydrate

FFD, (RS)-2'-hydroxy-5'-[(RS)-1-hydroxy-2 [[(RS) ρ-methoxy-α-methylphenethyl] amino]ethyl] formanilide (Fig 18), is a long-acting b2-agonist. It is used in the management of asthma and/or COPD [206]. Inhaled formoterol works like other β2-agonists, causing bronchodilatation by relaxing the smooth muscle in the airway so as to treat the exacerbation of asthma [208].

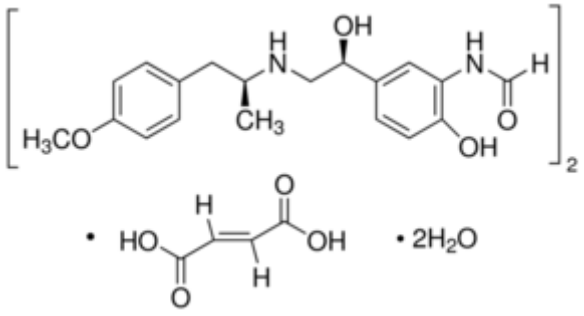

Fig 18: Chemical structure of Formoterol Fumarate Dihydrate

4.3.2.3 Fostair Inhaler

Each metered dose (ex-valve) contains 100 micrograms of beclomethasone dipropionate and 6 micrograms of formoterol fumarate dihydrate. This is equivalent to a delivered dose (ex-actuator) of 84.6 micrograms of beclometasone dipropionate and 5.0 micrograms of formoterol fumarate dihydrate. The dry powder of individual drugs (BDP and FFD) was supplied by Chiesi Pharmaceuticals supplied the dry powder of BDP and FFD as well as the Fostair inhaler (contained BDP/FFD). The drug substances were said to be 99.89% (w/w) purity for BDP and 99.20% (w/w) purity for FFD on dried basis.

4.3.2.4 [18F]-Flourodeoxyglucose (FDG)

[^{18}F] -FDG is a glucose analog with replacement of the oxygen in C-2 position with 18-fluorine. Though it behaves as glucose in many situations, there are some important differences that should be understood.

Just as glucose, FDG is actively transported into the cell mediated by a group of structurally related glucose transport proteins (GLUT). Once intracellular,

glucose and FDG are phosphorylated by hexokinase as the first step toward glycolysis. Normally, once phosphorylated glucose continues along the glycolytic pathway for energy production. [18F]-FDG however cannot enter glycolysis and becomes effectively trapped intracellularly as FDG-6-Phosphate. Tumour cells display increased number of glucose transporters, particularly GLUT-1 and GLUT-3, as well as higher levels of hexokinase, isoforms type I and II. Tumour cells are highly metabolically active (high mitotic rates), and favour the more inefficient anaerobic pathway adding to the already increased glucose demands. These combined mechanisms allow for tumour cells to uptake and retain higher levels of FDG when compared to normal tissues.

[^{18}F-FDG is not cancer specific and will accumulate in areas with high levels of metabolism and glycolysis. Therefore, increased uptake can be expected in sites of hyperactivity (muscular, nervous); active inflammation (infection, sarcoid, arthritis, etc.); tissue repair, etc.

4.3.3 HPLC Methods

HPLC methods has been developed to separate the two drugs; beclomethasone dipropionate (BDP) and formoterol fumarate dihydrate (FFD) on a reversed phase Enable HPLC Analytical C18 G 120A˚ (250 34.6 mm, 5 mm) column at ambient temperature using a mobile phase consisting of methanol:acetonitrile:phosphate buffer adjusted to pH 3.6 using orthophosphoric acid (65:25:10, v/v/v). Samples were analysed using the following parameters: flow rate, 1.0 mL/min; injection volume, 20 mL; run time, 6 min; temperature, 27+28C; detection wavelength, 220 nm.

4.3.3.1 Preparation of stock solution

Accurately weighed 1.2 mg of BDP was transferred to 10mL volumetric flask, dissolved and diluted with 3 mL of methanol to get BDP stock solution containing 400 µg/mL of BDP. Accurately weighed 0.3mg of FFD was transferred to 10 mL volumetric flask, dissolved and diluted with 7.5 mL of methanol to get FFD stock solution containing 20 µg/mL of FFD.

4.3.3.2 Preparation of HPLC calibration curve

Aliquots (0.1, 0.2. 0.4, 0.5 and 1.0 mL) from stock solution of BDP (400 µg/mL) and aliquots (0.1, 0.24, 0.3, 0.6 and 1.0 mL) from stock solution of FFD (20 µg/mL) were diluted up to 1mL with mobile phase to prepare mixture of calibration standard solutions corresponding to 40, 80, 160, 200 and 400 µg/mL of BDP and 2.4, 4.8, 6.0, 12, and 20 µg/mL of FFD. The calibration standard solutions were analysed by the method is section 3.3 above. Calibration curve was prepared by plotting peak area of BDP and FFD against their respective concentration.

4.3.3.3 Inhaler Sample preparation

The inhaler contained a mixture of both BDP and FFD in 100/6 µg/mL concentration as stated by the manufacturer. 10 puffs of the inhaler content were fired into the ACI at 28.3 flow pressure with 10 second interval between each actuation and 30 second waiting time at the end of the last actuation. 100mLs of methanol was used to wash off the drug samples from the actuator, cap, ACI throat and the plates on each stage of the ACI. The filter on the last stage of the ACI was sucked into the beaker containing 100mL of methanol. Each sample was dried off and rinsed with 5mLs of ethanol. 1 mL was taken out of each 5mLs rinsed solution for HPLC analysis.

4.3.3.4 HPLC Analysis of unlabelled drug

The chromatograms of standard solution (from dry powder of the two drugs) and inhaler solutions containing BDP and FFD were compared to determine the specificity of the HPLC method. The retention time of BDP and FFD was found to check selectivity of the method. The PDA (photo diode array) spectrum of drug peak obtained from sample and standard solutions were compared. Peak purity analysis was performed using Agilent HPLC software. The specificity was further determined by the complete separation of BDP and FFD along with other parameters like retention time (R_t), capacity factor (k), tailing or asymmetrical factor (T) 9this are parameters analysed with HPLC)

4.3.4 Radiolabelling

A known amount (~100-700MBq) of radioactive materials (Gallium-68, 18F-FDG and ^{18}F-thia-fatty acids ([^{18}F]-FTHA)) was dried and suspended in 500µl of ethanol.* 100µl containing a known amount of activity was added to the contents of a frozen. The inhaler was frozen using liquid nitrogen, the liquid nitrogen was poured onto the inhaler mounted upside down on an Eisco Retort Clamp over a ball and the content of the inhaler was allowed to freeze before drilling the hole into the inhaler. The hole was then resealed with a rivet. The inhaler was brought up to room temperature and then actuated into the impactor and plastic bags, the experiment was performed inside the fume hood to prevent airborne contamination. After actuating, the bag was removed from the fume hood to measure the activity by using capintec reader. The actuator, ACI throat and plates were washed and activity determined via gamma counting. Repeated experiment were conducted with different radioisotopes (as mentioned above) to determine dose/delivered activity curve in the bags and along the stages of ACI.

4.3.5 HPLC analysis of the radiolabelled drug

For the experiment with the high amount of activity, the ACI was left for some hours to allow radioactivity decay. When the ACI was less hot, the individual plates were removed for washing, 50mL of water and 50mL of methanol was used to wash the drugs and the [^{18}F]-FDG from the plates at each stage of ACI stage (making each sample to be 100 mL).

1 mL from each sample was taken for radioactivity determination using a gamma counter. The remaining 99mL of the sample from each plate was dried off and rinsed with 5mLs of methanol, 1mL from each sample were dispensed into the HPLC vials for HPLC analysis.

4.3.6 Calibration of the capintec dose calibrator

Before analysing the radioactive content of the bags and stages of the ACI, the equipment was calibrated in order to understand the geometric variability of the results, the capintec reader is very sensitive and the geometry and the position of the sample within the capintec reader determine the results. After

actuation into the bag, the bag will be squeezed and inserted into the capintec reader, the position of the bag within the capintec reader could change from one experiment to the other which may affect the result. A vial containing a known amount of activity was placed inside the capintec dose calibrator chamber (Fig 19) at different distances from the bottom of the reader to the top using equally sized polystyrene box (1×1×1inch). One box containing the vial was first placed at the bottom of the reader and the measurement of the activity was taken, followed by adding more boxes underneath the vial containing box in an incremental way until the vial reaches the top of the reader. Change of activity detection was recorded for the accuracy of the reading.

Fig 19: A vial containing certain amount of 18F-FDG inserted within 1×1×1inch polystyrene box. The first measurement was taken with the vial touching the bottom of the capentec dose calibrator, subsequently the box was lifted by inserting another 1×1×1inch box beneath it until the vial containing box reaches the top of the calibrator

4.4 Results

The aliquots from the samples of dry powder drugs were used to construct the calibration curve which appears to be linear in both FFA and BDP (Fig 20 and 21). The retention time (Time taken for the HPLC machine to detect and retain the sample) for both drugs from the dry powder inhaler are 3:11 mm:ss

and 3:50 mm:ss for FFA and BDP respectively. Moreover, the retention time for both drugs and unlabelled Fostair inhaler are closer together; 3:22-3:45 *mm:ss* for FFA and 3:47-4:20 *mm:ss* for BDP respectively (Fig 22, 23 and 24). In radiolabelled inhaler however, the retention time in both drugs appears to be far apart from each other 2:28-2:58 mm:ss for FFA and 4:09-4:32 mm:ss for BDP (Fig 25). The Abbreviated impactor measurement (AIM) concept is is short form of multi-stage cascade impactor with only 2 stages and filter. Due to its advantages over the multi-stage impactor measurement I used this impactor in this experiment. It is less time consuming, more precise, reduce chance of operation related errors and require less solvent for the recovery of the active pharmaceutical ingredient (API) [64, 209]. Characterization of active pharmaceutical ingredient (API) of orally inhaled products (OIPs) in non-fractionating part of the impactor (Throat of the ACI) is not well established [62]. As such, quantification in this experiment exclude the non-fractionating part. The Aerodynamic particle size distribution (APSD) along the fractionating part of the AIM comprises of large particle mass (LPM) and small particle mass (SPM). The LPM is APSD >5µg deposited on stage 1, whereas, the SPM comprised of the particle size deposited on stage 2 and the filter ≤5 µg. The large particle mass (LPM)/small particle mass (SPM) ratio of the unlabelled inhaler experiment was 0.5:1 and 0.2:1 in FFD and BDP respectively (Fig 26 and 27). The LPM to SPM ratio of FFD in the radiolabelled inhaler is similar to that found in an unlabelled inhaler. However, the ratio of the BDP found in the radiolabelled inhaler was 0.6:1 much higher than the unlabelled inhaler (0.2:1). Generally, FFD and BDP in an unlabelled inhaler are found to be more in SPM with very small respirable fractions (Fig 28, 29, 30 and 31). The [^{18}F]-FDG ratio between LPM and SPM was 05:1. As with the drugs, more [^{18}F]-FDG was found to deposit on the lung section of the impactor (stage 2). However, there are huge deposition of drugs and [^{18}F]-FDG along non-fractionating part of the impactors in all of the experiments. In general, although there was high deposition of both drugs (FFD and BDP) and [^{18}F]-FDG on the non-fractionating part of the impactor, the deposition

within the fractionating was predominantly within 1-5µg which is a desirable fine particle fraction (FPF) of the API leading to pulmonary deposition (fig 31).

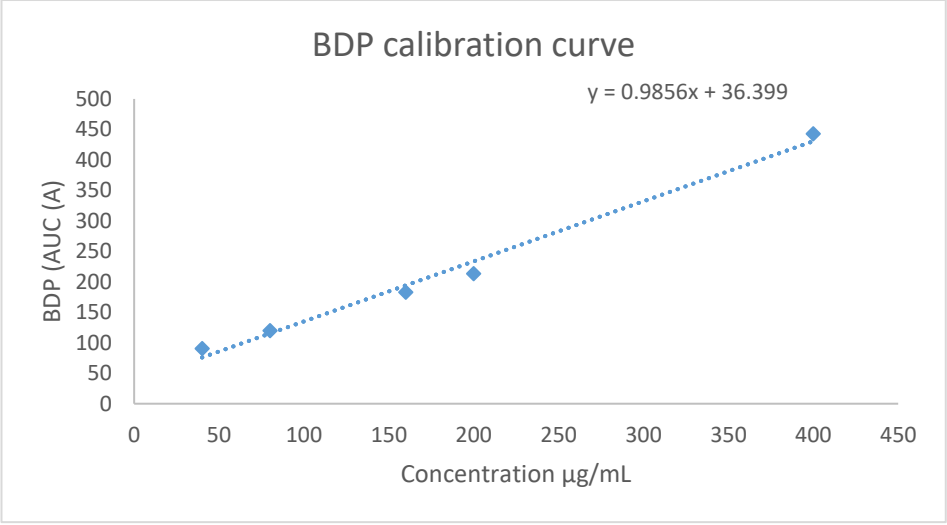

Fig 20: the relationship between the concentration of BDP sample and the chromatogram AUC

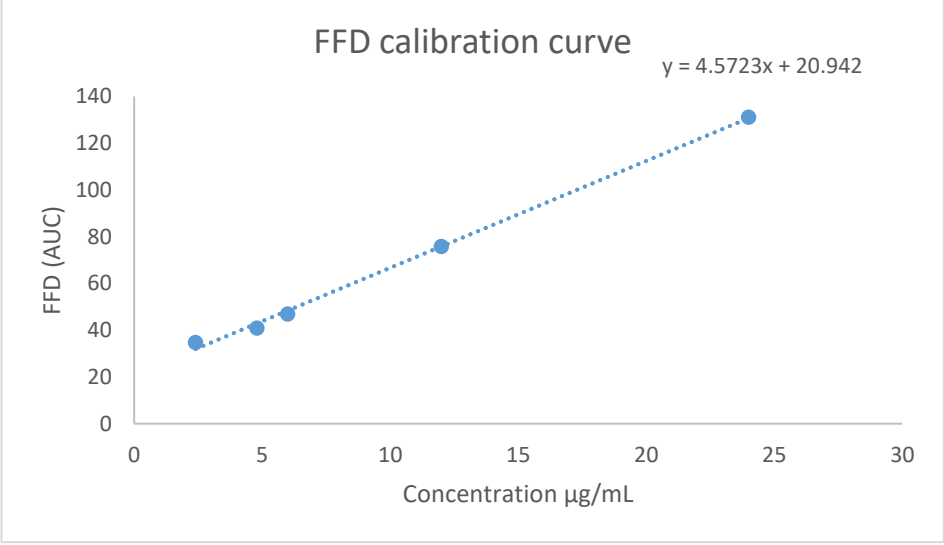

Fig 21: the relationship between the concentration of FFA sample and the chromatogram AUC

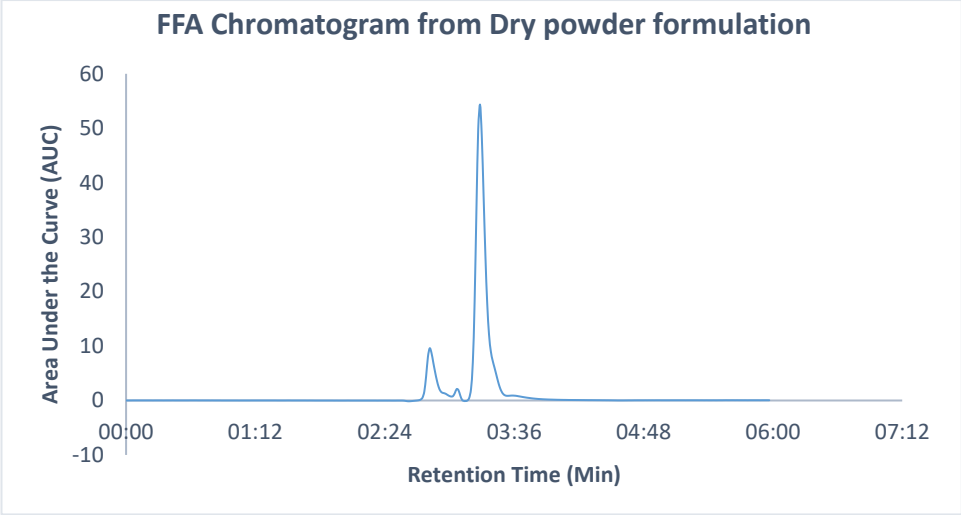

Fig 22: The FFA Chromatogram appearance, when 20µl from a vial containing 1mL of 20 µg/mL of BDP was injected. The retention time was 3:17 mm:ss

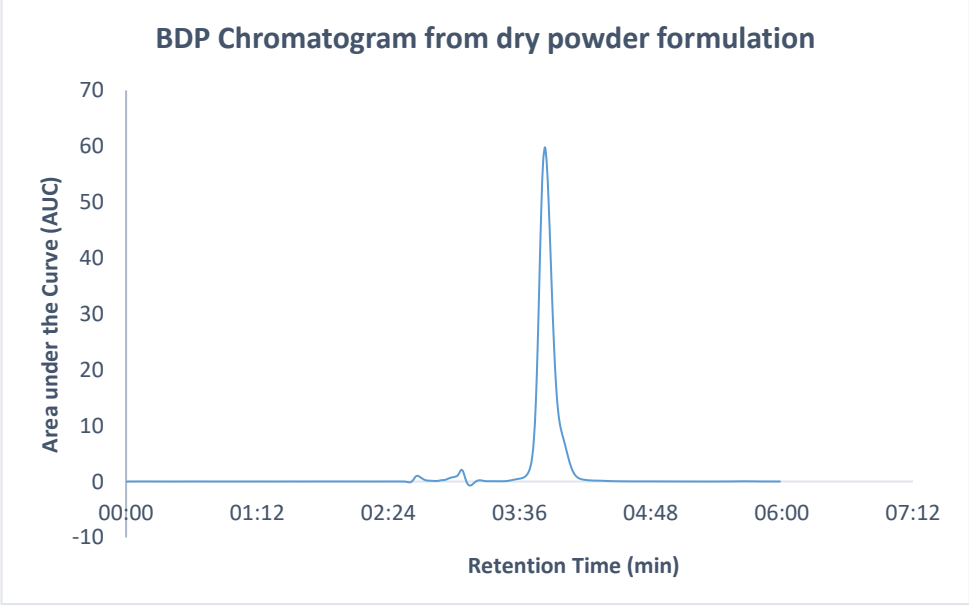

Fig 23: The BDP Chromatogram appearance, when 20µl from a vial containing 1mL of 400 µg/mL of BDP was injected. The retention time was 3:50 mm:ss

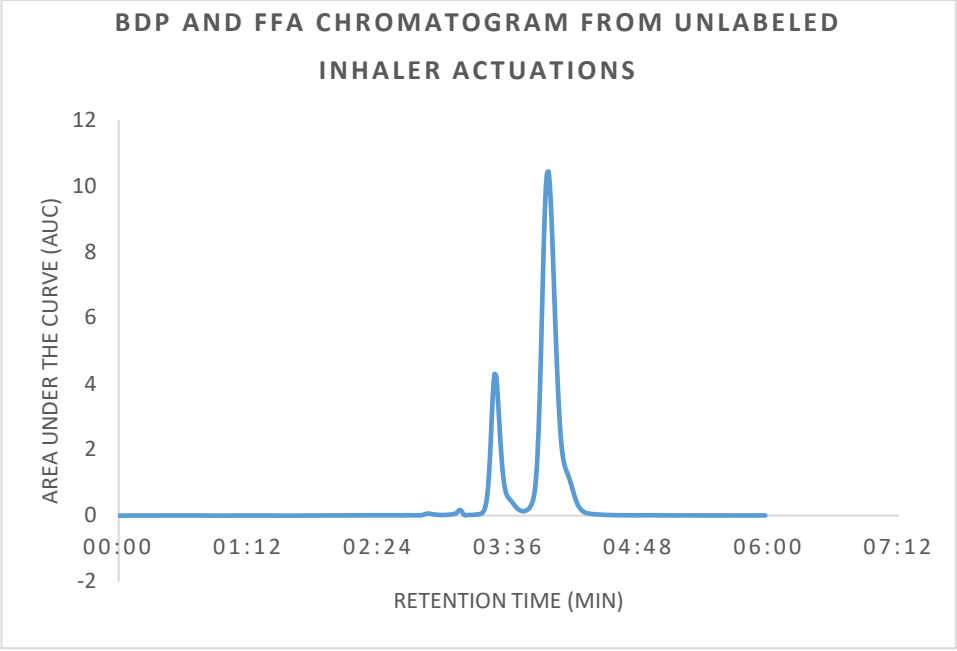

Fig 24: The Chromatogram from washing the ACI plate at lung level (1-5µg). The retention time of BDP and FFA are 3.32 and 3.56 mm:ss

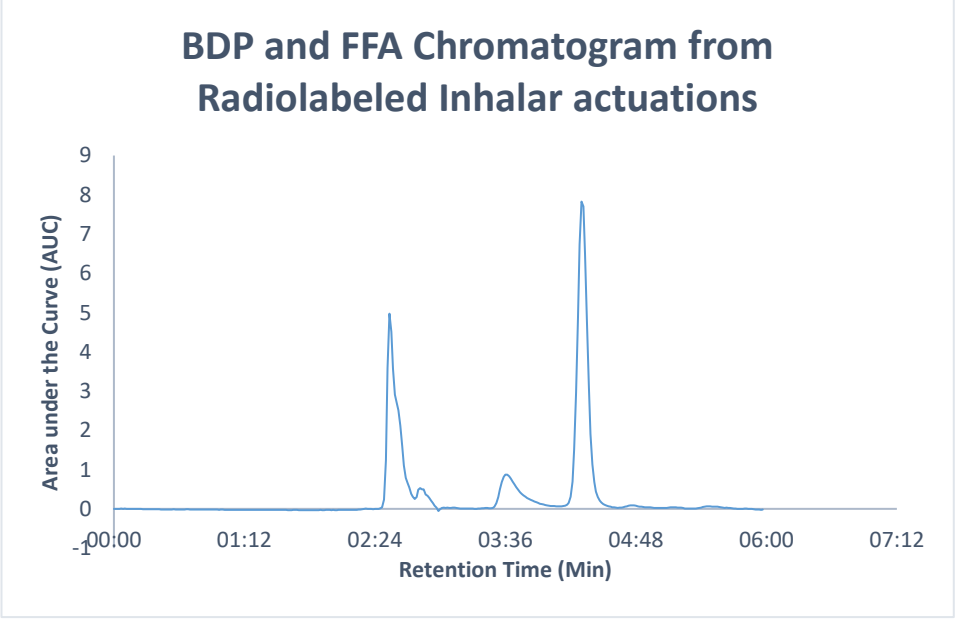

Fig 25: The Chromatogram from washing the ACI plate at lung level (1-5µg). The retention time of BDP and FFA are 2.32 and 4.18 mm:ss

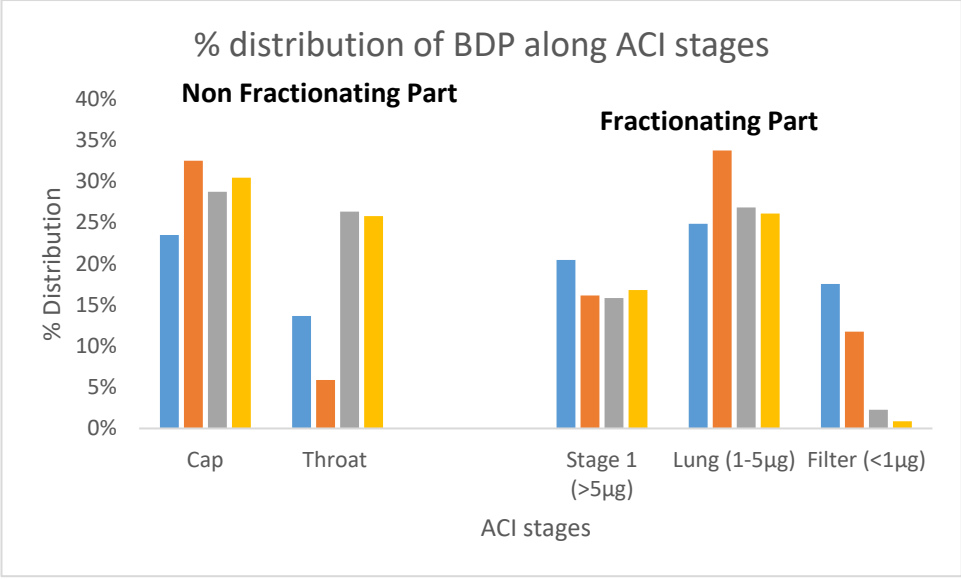

Fig 26: % distribution of unlabelled BDP in 4 different experiments (LPM:SPM=0.2:1). The deposition on the cap and throat (preseparator) is considered to be the transition part of the impactor, it was expected to have a cut-off particle sizes of 8.7 µm. The deposition on stage 1 has the cut-off particle sizes above 5 µm which mimic deposition on upper respiratory tract, whereas the deposition on lung stage has the cut-off particle sizes between 1 and 5 µm mimic deposition within the lower respiratory tract. The particle deposited on the filter are considered to be too small to deposit in the lung and therefore exhaled.

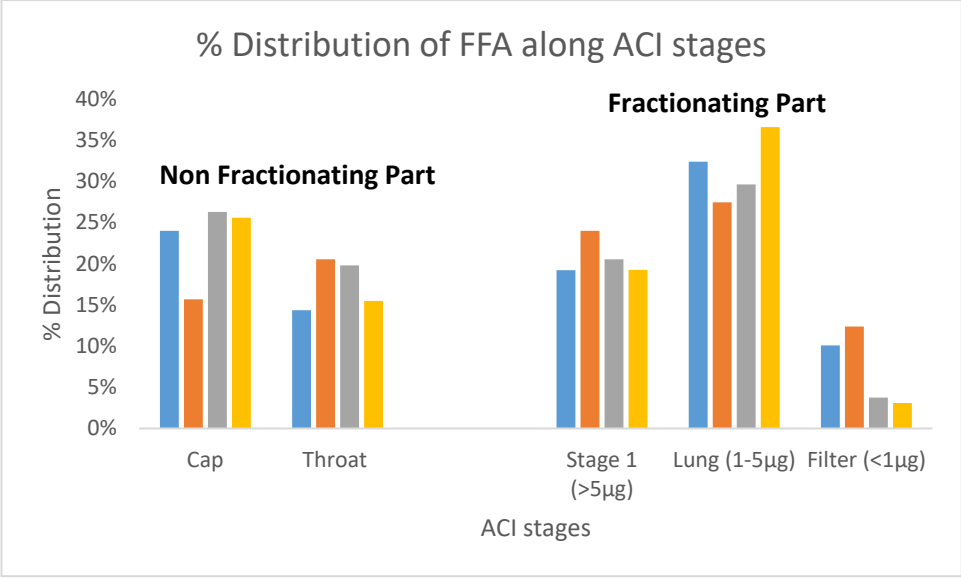

Fig 27: % distribution of unlabelled FFD in 4 different experiments (LPM:SPM=0.5:1). The deposition on the cap and throat (preseparator) is considered to be the transition part of the impactor, it was expected to have a cut-off particle sizes of 8.7 µm. The deposition on stage 1 has the cut-off particle sizes above 5 µm which mimic deposition on upper respiratory tract, whereas the deposition on lung stage has the cut-off particle sizes between 1 and 5 µm mimic deposition within the lower respiratory tract. The particle deposited on the filter are considered to be too small to deposit in the lung and therefore exhaled.

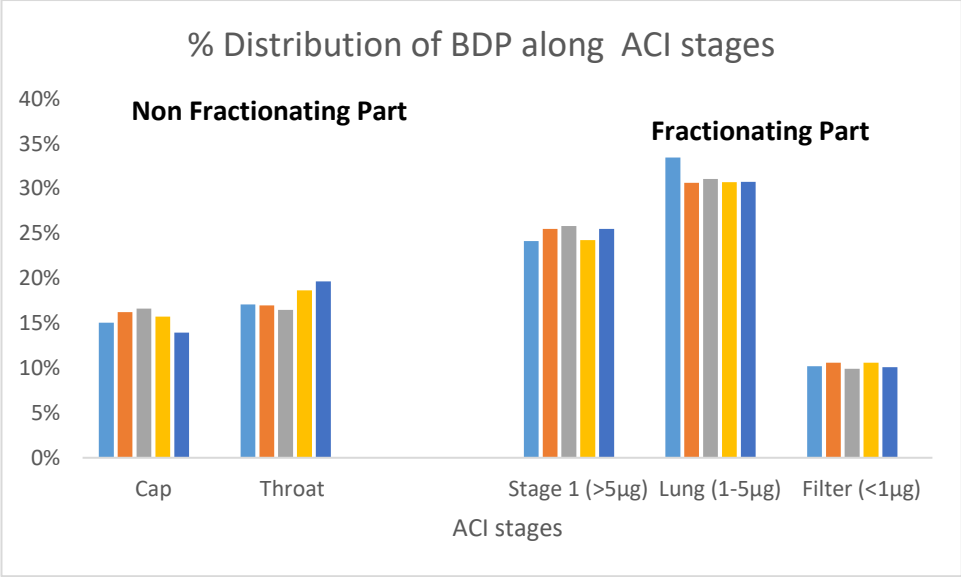

Fig 28: % distribution of radiolabelled BDP in 5 different experiments (LPM:SPM=0.6:1). The deposition on the cap and throat (preseparator) is considered to be the transition part of the impactor,, it was expected to have a cut-off particle sizes of 8.7 µm. The deposition on stage 1 has the cut-off particle sizes above 5 µm which mimic deposition on upper respiratory tract, whereas the deposition on lung stage has the cut-off particle sizes between 1 and 5 µm mimic deposition within the lower respiratory tract. The particle deposited on the filter are considered to be too small to deposit in the lung and therefore exhaled.

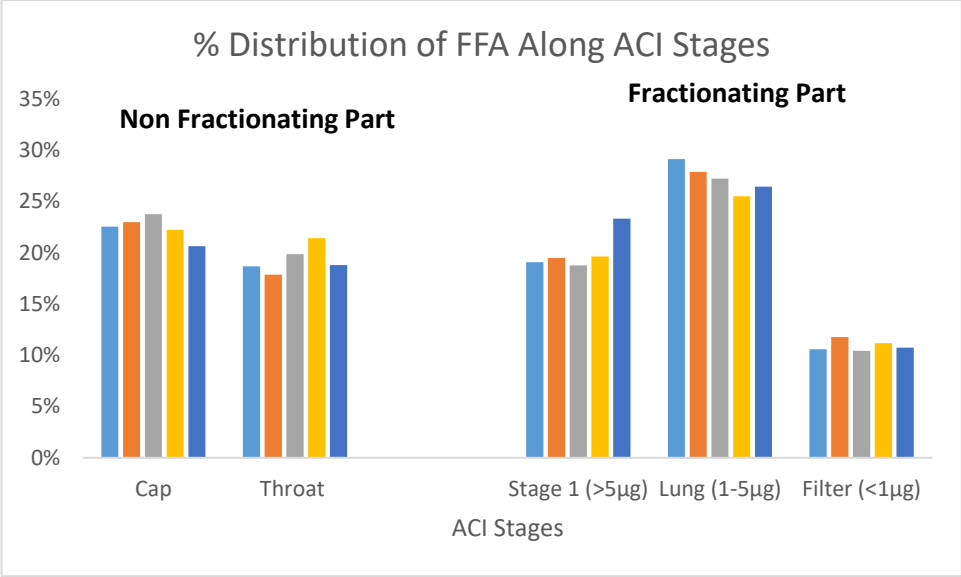

Fig 29: % Distribution of radiolabelled FFA along ACI stages in 5 different experiments (LPM:SPM=0.5:1). The deposition on the cap and throat (preseparator) is considered to be the transition part of the impactor,, it was expected to have a cut-off particle sizes of 8.7 µm. The deposition on stage 1 has the cut-off particle sizes above 5 µm which mimic deposition on upper respiratory tract, whereas the deposition on lung stage has the cut-off particle sizes between 1 and 5 µm mimic deposition within the lower respiratory tract. The particle deposited on the filter are considered to be too small to deposit in the lung and therefore exhaled.

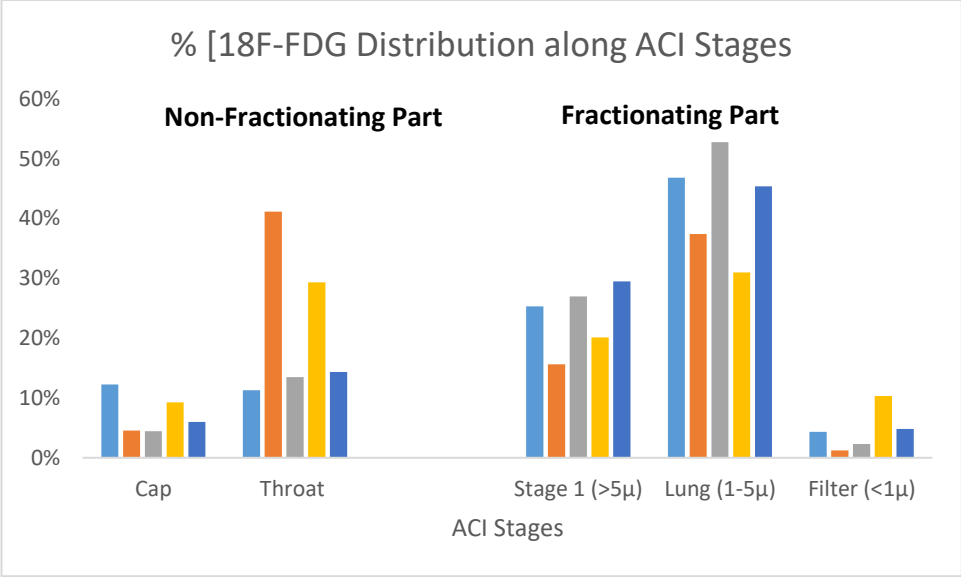

Fig 30: % distribution of activity along the ACI stages from different experiments. The deposition on the cap and throat (preseparator) is considered to be the transition part of the impactor,, it was expected to have a cut-off particle sizes of 8.7 µm. The deposition on stage 1 has the cut-off particle sizes above 5 µm which mimic deposition on upper respiratory tract, whereas the deposition on lung stage has the cut-off particle sizes between 1 and 5 µm mimic deposition within the lower respiratory tract. The particle deposited on the filter are considered to be too small to deposit in the lung and therefore exhaled.

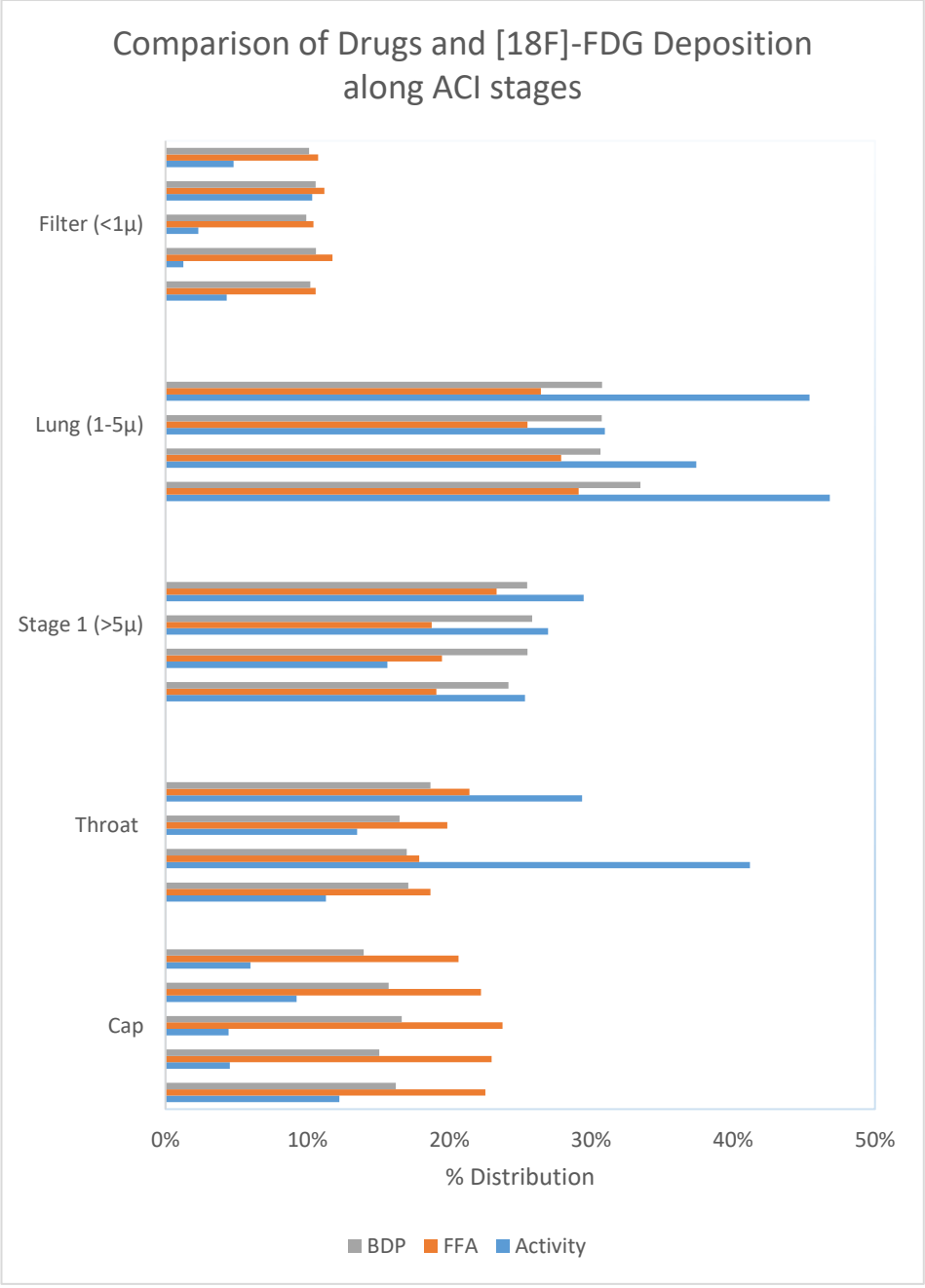

Fig 31: % distribution of drugs and activity along the ACI stages from different experiments (from all the experiments). The deposition on the cap and throat (preseparator) is considered to be the transition part of the impactor, it was expected to have a cut-off particle sizes of 8.7 µm. The deposition on stage 1 has the cut-off particle sizes above 5 µm which mimic deposition on upper respiratory tract, whereas the deposition on lung stage has the cut-off particle sizes between 1 and 5 µm mimic deposition within the

lower respiratory tract. The particle deposited on the filter are considered to be too small to deposit in the lung and therefore exhaled.

4.4.1 Dose/Delivery curve

To determine the amount of activity actuated from the inhaler, 5 actuation were made into a reseal able bags and measured using capintec dose calibrator. 2.3% ± 0.4% of activity in the canister is realised by actuating the inhaler 5 times into the bags (Fig 32). About 5% of the content of the inhaler was expected to be actuated after 10 actuations of the inhaler without any significant variability. This experiment help in designing the dose/activity curve.

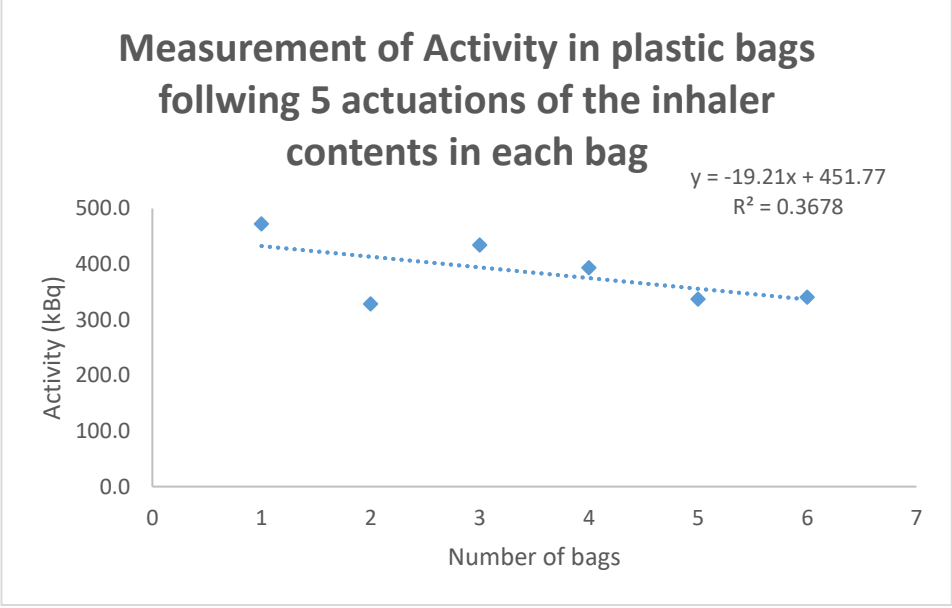

Fig 32: 16.70MBq of activity was in the inhaler at the beginning of actuation. 5 actuations of the inhaled were made into each plastic bag with mean and SD of 384.54 ± 59.26KBq. This amount to 2.3% ± 0.4 of the initial activity. From the graph, there is no significant variation in the results regardless of the position of the vial within the capintec reader.

4.4.2 Measurement of Bags in Capintec Dose calibrator

The bag get different geometry each time it's been squeezed into the capintec reader. The effect of the change in geometry of the bags to the amount of

activity detected by the capintec reader, Three (3) different samples (10.90, 6.82 and 0.69MBq) in a vial were used. The measurement of radioactivity when the vial was placed at different level of capintec reader. The mean and standard deviation (mean and SD) from a vial containing 10.9MBq of [^{18}F]-FDG were 11.16 ± 0.11 (mean and SD) and the vial containing 6.82MBq has 6.90 ± 0.13 (mean and SD) whereas, the vail with 0.69MBq has 0.5 ± 0.01 (mean and SD). All radioactivity was decay corrected and this activity measured correspond to 2.3% ± 0.4% of the activity in those vials (Fig 19).

4.5 Discussion

Several *in-vitro* techniques are currently in used for the measurement of the particle size distribution of aerosols from OIPs using different pulmonary drug devices such as pMDIs, dry powder inhalers (DPIs) and nebulizers. The ultimate goal is to ascertain their application for product development, quality control testing and for simulation of likely performance in clinical use. The limitations of these various technique has been identified and decades of technological advancement brought about significant improvements to these techniques to be more predictive of the clinical situation [210].

The ACI operate on constant flow rate (i.e. 28.3L.min) drawing a fixed volume of air from the inhaler to the pump through the ACI stages but these does not replicate the actual human inhalation flow rate. However, the principles of size-separation of particles in the impactor is similar to the particles deposition pattern in in the lung [211]. Moreover, the ability of the impactors to determine the chemical identity of the deposited particles on each stage has allowed a better understanding of which stage of the impactor contain API [63].

The variability in the results can be attributed to many geometric and operational factors affecting the collection efficiency of each stage of the impactor. These factors includes; the linear velocities of the airstreams; the jet opening shape and size; the aerosol particle shape; the particle size; the particle density; the slip correlation; the air viscosity; the jet-to-collector

distance; the jet throat length as well as the character of the jet airflows [58]. The International Pharmaceutical Aerosol Consortium on Regulation and Science (IPAC-RS) design a diagram that visualized and categorized the factors that may affect a Cascade Impactor (CI) measurements [62].

Manual operation involved in operating impactor increase the likelihood of bias in the results [62]. However, reducing the number of stages in Abbreviated Anderson Impactor has significantly increase speed of the operation and reducing the recovery errors [209].

Additionally improper cleaning and maintenance can affect the proper working order of the impactor. This may results in significant variability of the aerodynamic particle size distribution resulting in misinterpretation of the product performance [60, 212].

The HPLC method adapted in this experiment is similar to the one in [213] with recovery of both drugs in 6 minutes. These was found consistent in the dry powder of the drugs, radiolabelled and unlabelled inhalers. Although the retention index of the drugs differ slight but it was within an acceptable range [214]. The process of radiolabelling of drugs molecules in PET is very complex and lengthy procedures [215], a standard radiolabelling process of the drugs has not been attempted in this study however, only a small amount of radioactive material were added to the dry inhaler. Proper shaking of the radiolabelled inhaler allow a significant mixing of the radioactivity and the drugs. Several radioactive materials were used in this experiment such as ^{68}Ga, [^{18}F]-Thia-fatty acid and [^{18}F]-FDG, only [^{18}F]-FDG was found to be reproducible. Failure to recover the radioactivity from the impactor throat and plates made ^{68}Ga, [^{18}F]-Thia-fatty acid unsuitable for this experiment. These process was found to be effective in distributing the drugs and radioactive materials along the stages of the impactor. Although, distribution of the drugs and the activity was not found to be the same at all the stages of the impactor, however, the distribution pattern is quite uniform, with more deposition on

the impactor stage believed to represent lung section with particles sizes between 1-5µg.

It has appeared that the [^{18}F]-FDG has travelled at similar proportion to the drugs along the stages of ACI. This could mean that [^{18}F]-FDG could be used as a bio marker to determine the precise location of the aerosol drug along the respiratory tract. These method can be used to complement the HPLC method in validating OIPs performance using impactor technology.

All efforts have been made to reduce the operator errors in performing these measurement to reduce the bias in the interpretation of these results.

4.6 Limitation

Actuation of the dummy inhaler containing [^{18}F]-FDG have not been attempted, this was meant to be done at some stage during the experiment. However, there was significant technical problems with the cyclotron in the University PET Centre and I had to return the ACI (the ACI was loaned from). Comparing the distribution of the [^{18}F]-FDG from dummy inhaler would have added more information regarding the behaviour of [^{18}F]-FDG when it is actuated along or in combination with the drugs.

4.7 Conclusion

Radiolabelling of the OIPs has the potentials in understanding APSD of the API. In this study an attempt to make a simple mixture of the drugs with radiotracer in an inhaler canister has been made, using abbreviated impactor. This impactor has the advantage of reducing the length of the experiment and improved APSD measurement accuracy. Although the impactor has been used for decades in pulmonary drug developmental studies, to my knowledge this is the first experiment using the combination of radiotracer and the drugs in the same canister. The purpose of this experiment was to explore the potential of imaging studies in pulmonary drug development. Although the animal inhalation studies which was supposed to be the last stage of this experiment has not been conducted due to time factor. The initial stages of

the experiment have been concluded and provided some useful insight into the potentials of this experiment.

In order to establish the relationship between inhaler radiotracer loading and delivered dose, the content of the inhaler (radiotracer and drugs) was actuated into reseal able bags before actuating the content into the impactor. These provided the measurement of the radiotracer per actuation of the inhaler and this information is crucial in understanding the radiation exposure in the development of these experiment. Actuating the content of the inhaler into the impactor stages provided information on the distribution pattern of the drugs and the radiotracer along the stages of the impactor. The deposition of the radiotracer and the drugs on the impactor inlet/throat has not been considered for quantification because the section has not been fully characterized to contain API. However, the particle deposition on the subsequent stages of the impactor were expected to contain API. The lower the impactor stage the finer the particle fraction, as the larger particles with enough inertia are expected to be deposited in the preceding stage. This phenomenon is explained by the principle of inertial impaction. The information from fine (small) and coarse (large) particle size fractions of the API in this experiment has demonstrated more API in the fine particle fraction. This translate to having more particle of drugs generated are between 1-5µg. moreover, the flow of the radiotracer within the impactor is similar to that of the drugs. This information is vital for the clinical imaging of the pulmonary drug deposition. Radiolabelling of the OIPs may provide a better understanding of the performance of the pulmonary drug delivery devices such as inhalers and nebulisers. It will also provide more understanding of the behaviour of the drug particles within the respiratory tract. Although, the drug molecules were not properly radiolabelled in this study, homogenous distribution of the radiotracer and the drugs along the impactor stages were demonstrated. However, there is need for a proper radiochemistry to better understand the interaction between radiotracer and the drugs. An animal in vivo/ex vitro study with follow up PET-CT imaging will be needed in order

to provide the correlation of drugs and radiotracer distribution between stages of impactor and the animal respiratory tract.

Chapter 5 Positron Emission Tomography (PET) in Idiopathic Pulmonary Fibrosis (IPF)

5.1 Background

Idiopathic Pulmonary Fibrosis (IPF) is the most frequent and deadliest form of Idiopathic Interstitial Pneumonias (IIPs) [118]. It is progressive and irreversible with median life expectancy of 2-4 years after diagnosis [30, 120, 121]. Despite several studies on IPF, the aetiology is still not fully understood [122, 138, 216]. However, several factors such as genetics, environmental and viral infection have been associated with the incidence of IPF [133], it is more predominant in males with an associated history of smoking [133, 217]. It is common among elderly people (above 50 years), there is incidence of about 100-fold higher in people above 75 years of age than in those below 50 years of age [217]. IPF has been shown to have high mortality rate than some malignancies such as bladder cancer [176, 218].

The disease course of idiopathic pulmonary fibrosis (IPF) is unpredictable and there is lack of biomarkers that accurately identify active disease, aid prognostication, and predict response to drug therapy [144]. Recently, Positron Emission Tomography-Computerised Tomography (PET-CT) imaging has revealed increased ^{18}fluorodeoxyglucose [^{18}F]-FDG) uptake both in areas of fibrotic lung and areas of lung with normal radiological appearance in IPF [130, 219]. As the disease course of IPF is characterised by increasing heterogeneity at the cellular level, we here evaluate the overall uptake of [^{18}F]-FDG in the radiologically normal lung of a small cohort of patients as well as the heterogeneity of uptake using established textural features [220].

5.2 Aims

Idiopathic pulmonary fibrosis (IPF) patients' demonstrates high [^{18}F]-FDG uptake in fibrotic lung tissues defined by high-resolution computed tomography (HRCT). The aim of the retrospective study was to review the [^{18}F]-FDG uptake at sites of normal-appearing lung on HRCT in IPF. The

findings may demonstrate high sensitivity of PET scan over CT scans on early fibrotic changes.

5.3 Materials and Methods

5.3.1 Study selection

Patients with IPF diagnosed in accordance with international guidelines that had undergone PET-CT imaging for concomitant cancer diagnosis and/or staging were identified retrospectively in a single interstitial lung disease (ILD) tertiary referral centre. Patients that had a PET-CT scan in the same centre for cancer diagnosis and/or staging without non-malignant lung disease were identified to form two control groups: a lung cancer control group and a control group with no evidence of intra-thoracic disease (extra-thoracic malignancy controls) (Fig 33). These two control groups were identified to allow assessment of whether the presence of thoracic malignancy effected [^{18}F]-FDG uptake. In the event of no effect being identified, a pooled analysis comparing IPF patients and all controls was planned.

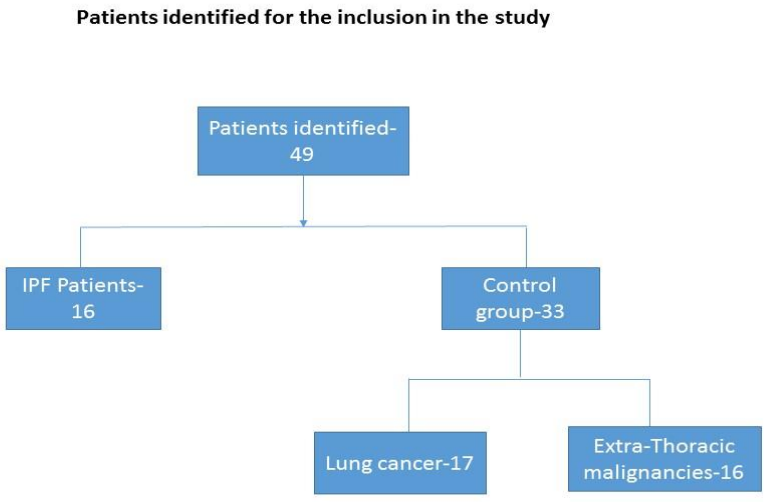

Fig 33: The group of Patient retrospectively identified to be included in the research

5.3.2 Image Analysis

Images were analysed by two experienced radiologists. [^{18}F]-FDG uptake and textural features were assessed within manually placed regions of interest (ROIs). ROIs were 3 dimensional and measured 10mm in diameter (Fig 34). 4 ROI were placed in areas of lung with normal CT appearance in IPF patients and corresponding areas in controls. Two ROIs were drawn in the upper lobe (posterior and anterior) and the other 2 ROIs were drawn in the middle or lower lobe where available. 4 ROIs were placed within areas of fibrosis in IPF patients. All ROI were placed away from areas of high FDG uptake (e.g. concomitant tumour, mediastinum, and diaphragm) to avoid spill over effect. To demonstrate a spill over effect, a lung phantom model was filled with a known amount of [^{18}]F-FDG and imaging with standard protocols was conducted. Several 10 mm circular ROIs were drawn horizontally from the edge of myocardium towards the periphery of the lung border. The quantification of these ROIs revealed the that the [^{18}]F-FDG uptake in these ROIs decreases the further away the RIO is from the myocardium (fig 35). These could mean the [^{18}]F-FDG uptake in the heart could affect the uptake of [^{18}]F-FDG in the neighbouring lung tissue.

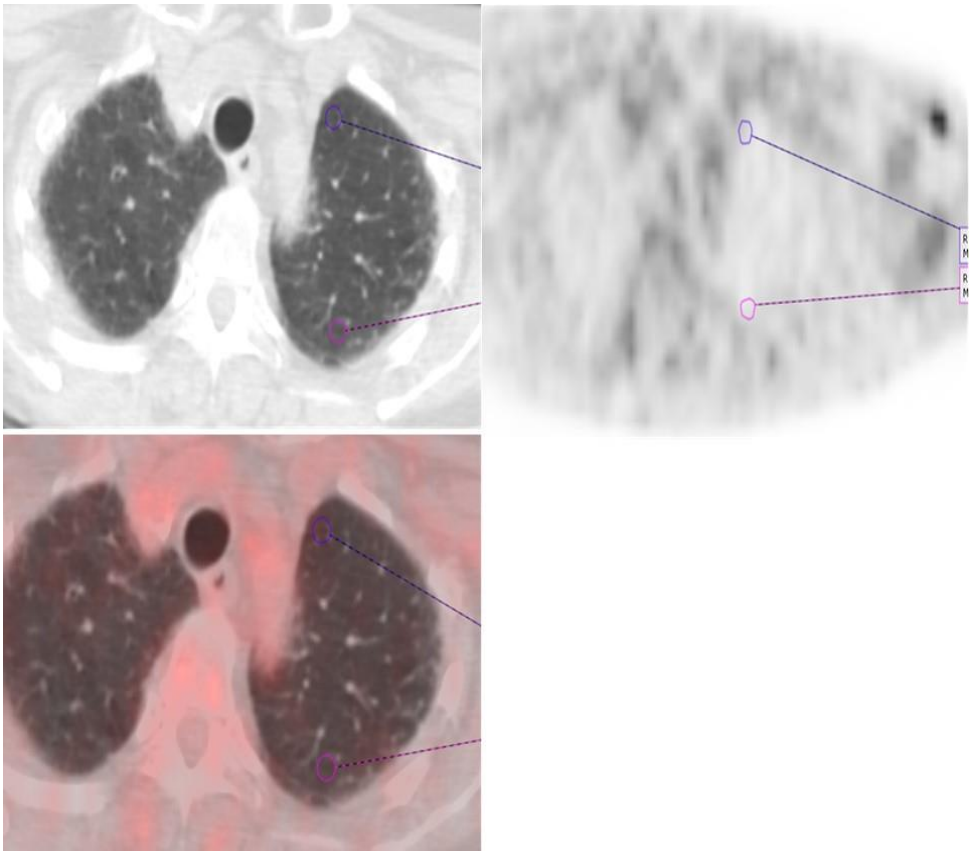

Fig 34: CT, PET and fused PET-CT images with 10mm ROIs within a normal CT appearing lungs

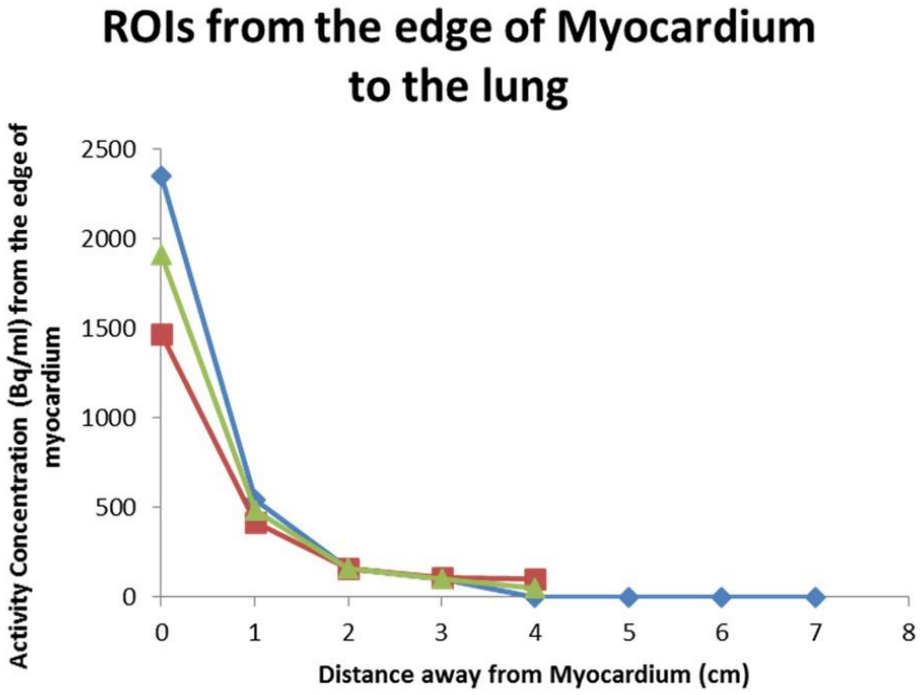

Fig 35: Demonstration of the effect of spill over of activity, ROI drawn closer to a hot area (e.g. myocardium) increases the uptake within the ROI. This effect overestimates the uptake in the area within the ROI.

5.3.3 Standard Uptake Value (SUV) Measurements

Mean and maximum standardized uptake values (SUV) within ROI were normalised using body weight (BW), body surface area (BSA) and activity concentration ([^{18}]F-FDG counts within a particular ROI). The average of all 4 ROIs in each patient were taken and the data are presented as mean ± SD. A paired t-test was used to compare fibrotic and normal lung in IPF patients and unpaired, 2-tailed t-tests were used to compare IPF and controls both with p-value <0.05 considered statistically significant.

The mean of 2 anterior ROIs on the upper and lower lobes was compared with the 2 posterior ROIs on the upper and lower lobes and paired t-tests were used to ascertain the differences between their means. Both SUV and CT number (Hounsfield unit) were treated the same way. Pearson correlation coefficients

between the features that were statistically significant were made to measure the strength of correlation between any two features.

Comparison of [^{18}F]-FDG uptake between normal, fibrotic lung, mediastinal blood pool (MBP) and liver were made. MBP and liver uptake were used as reference standards for lung imaging. Normal aerated lung has lower uptake than MBP and liver.

5.3.4 Computed tomography number (CT Number) Measurements

CT number which is expressed in Hounsfield Units (HU) within ROI were extracted from all 4 ROIs. The average of all 4 ROIs in each patient were taken and the data presented as mean ± SD. A paired t-test was used to compare fibrotic from normal lung in IPF patients and unpaired, 2-tailed t-tests and Bonferroni correction to account for multiple comparisons were used to compare IPF and controls both with p-value <0.005 considered statistically significant.

5.3.5 Textures Analysis

Twenty representative textural features were extracted from each ROIs both from PET and CT images. Those included First Order Statistics (FOS) derived from the grey-level intensity distribution, a measure of grey-level uniformity derived from the Laplacian of Gaussian (LoG) technique for a range of filter sizes (mm), and Laws Texture features (Table 3). The average of all 4 ROIs in each patient were taken and the data are presented as mean ± SD. A paired t-test was used to compare fibrotic from normal lung in IPF patients and unpaired, 2-tailed t-tests were used to compare IPF and controls both with p-value <0.05 considered statistically significant.

The mean of 2 upper lobe ROIs was compared with the other 2 ROIs and paired t-test was used to ascertain the differences between their means. Pearson correlation coefficient between the features that were statistically significant were made to measure the strength of correlation between any two features.

Textural Features Extracted from the ROIs					
1	Haralick 3D 2^6 Information Measure of Correlation	8	LoG size=3.8438 UPP	15	LoG size=6.1875 kurtosis
2	Haralick 3D 2^6 Sum of Squares: Variance range	9	LoG size =3.8438 skew	16	Laws E5E5 mean
3	Haralick 3D 2^6 Angular second moment mean	10	LoG size =3.8438 kurtosis	17	Laws E5S5 mean
4	Haralick 3D 2^6 Homogeneity range	11	LoG size =6.1875 UPP	18	LawsTex L5E5 mean
5	Haralick 3D 2^6 Entropy range	12	LoG size =6.1875 skew	19	LawsTex L5L5 std
6	First Order Statistic entropy	13	First Order Statistic std	20	LawsTex L5E5 std
7	First Order Statistic kurtosis	14	Shape D1		

Table 3: Textural features extracted from each ROI from PET and CT images

5.4 Results

Forty-nine subjects were identified and included in the study. 15 IPF patients (12 men, 3 women; age; 74.1 ± 10.2 years), 17 lung cancer controls (men 10, women 7; age 61.3 ± 16.4 years), and 16 extra-thoracic malignancy controls (men 9, women 7; age 64.5 ±12.4 years). Lung cancer patients staging was the most common reason for PET-CT imaging in IPF patients (11/16). The majority of extra-thoracic malignancy controls had PET-CT imaging to assess lymphoma or melanoma that was in remission (11/16). All 17 patients in the

lung cancer control group had PET-CT for lung cancer diagnosis and/or staging. IPF patients and 2 control groups (lung cancer and extra-thoracic malignancy) were compared.

Areas of radiologically established fibrosis in IPF patients exhibited higher SUV Max uptake in all the 3 normalisation techniques; body weight (BW), body surface area (BSA) and activity concentration (AC) compared to radiologically normal lung in the same patient (SUV Max (BW) 0.51 ± 0.15 and 0.24 ± 0.07, p<0.001; SUV Max (BSA) 0.5 ± 0.14 and 0.2 ± 0.07, p<0.001; SUV Max (AC) 7078.2 ± 3446.7 and 3250.6 ± 1509.3, P<0.001 (Fig 36,37 and 38).

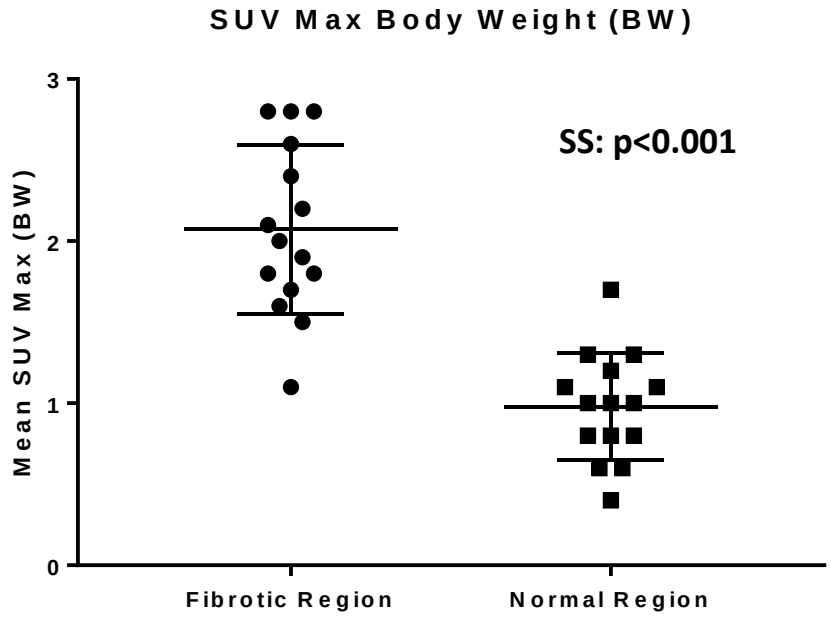

Fig 36: The comparison of the average of all 4 fibrotic ROIs and 4 normal ROIs in each patients normalized with body weight (BW).

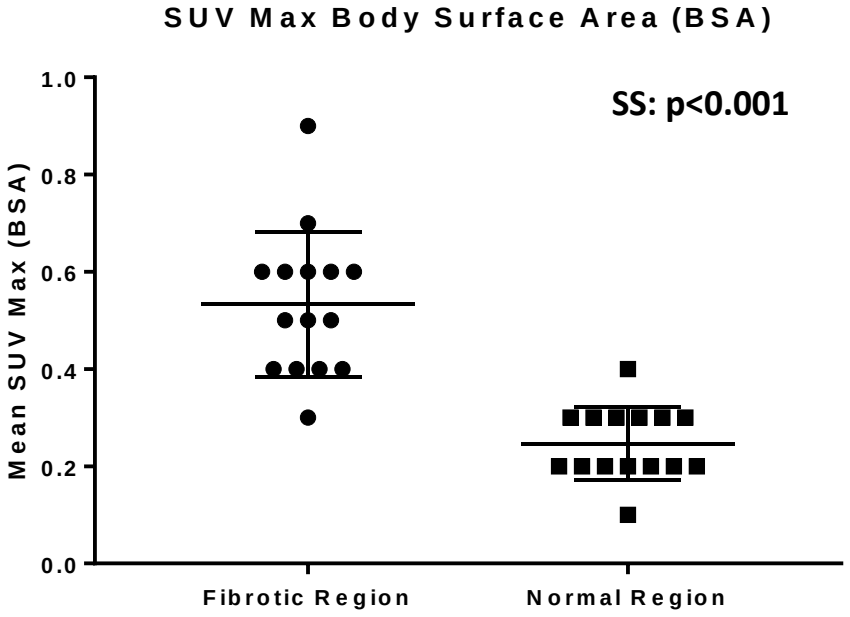

Fig 37: The comparison of the average of all 4 fibrotic ROIs and 4 normal ROIs in each patients normalized with body surface area (BSA).

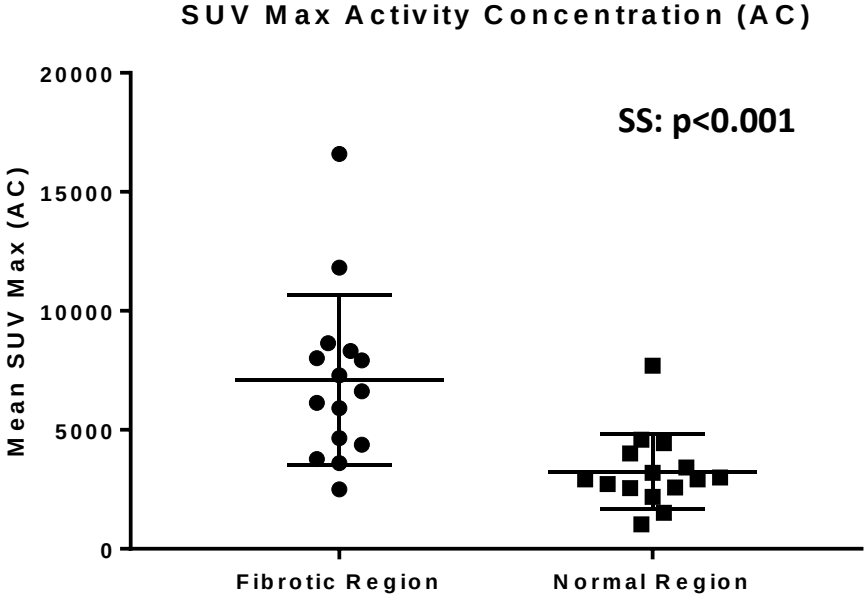

Fig 38: The comparison of the average of all 4 fibrotic ROIs and 4 normal ROIs in each patients normalized with Activity Concentration (AC).

Areas of radiologically established fibrosis in IPF patients exhibited higher SUV Mean uptake in all the 3 normalizations (BW, BSA and AC) compared to radiologically normal lung in the same patient (SUV Mean (BW) 0.33 ± 0.1 and 0.2 ± 0.07, p<0.001; SUV Max (BSA) 0.3 ± 0.1 and 0.2 ± 0.1, p<0,001; SUV Max (AC) 4160.3 ± 2218.9 and 2397.6 ± 1547.5; P<0.001 (Fig 39, 40 and 41).

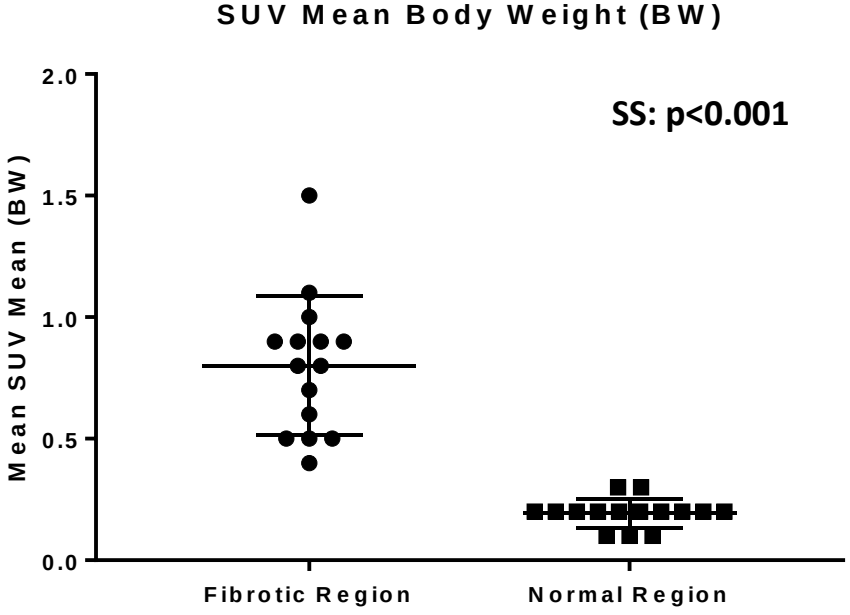

Fig 39: The comparison of the average of all 4 fibrotic ROIs and 4 normal ROIs in each patient normalized with body surface area (BSA).

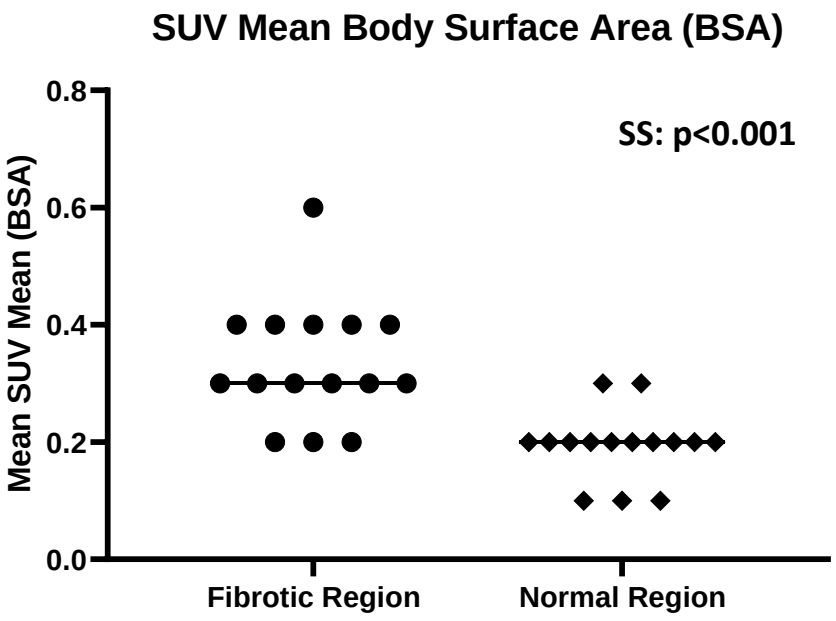

Fig 40: The comparison of the average of all 4 fibrotic ROIs and 4 normal ROIs in each patient normalized with body surface area (BSA).

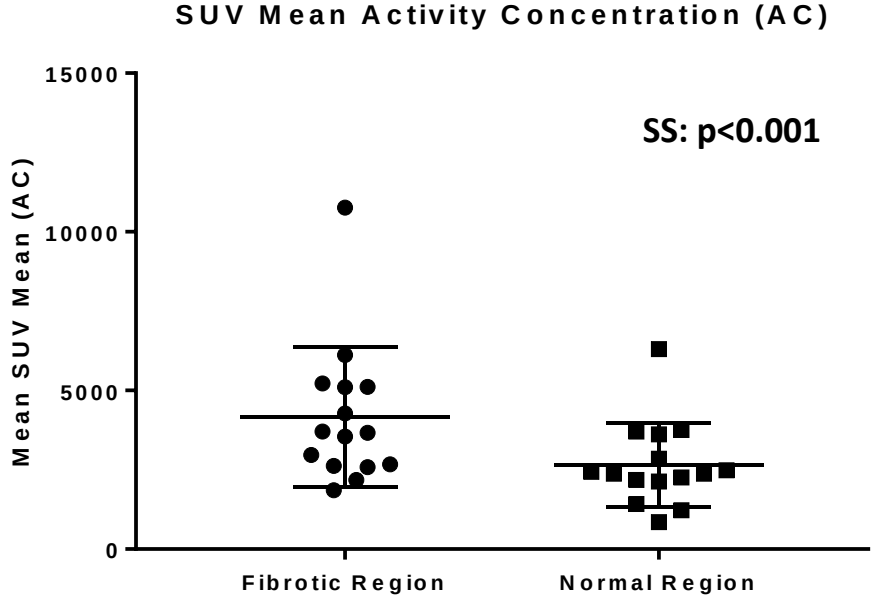

Fig 41: The comparison of the average of all 4 fibrotic ROIs and 4 normal ROIs in each patients normalized with Activity Concentration (AC).

No difference in SUV Max uptake was observed in the mean of 4 ROIs between lung cancer controls and extra-thoracic malignancy controls in all 3 normalizations (SUV Max BW, BSA and AC) (Fig 42, 43 and 44) and therefore data from these groups were pooled for comparison with IPF patients (Fig 45, 46 and 47). The maximum SUV of radiologically normal lung in IPF patients was significantly higher than the normal lung in controls (SUV Max (BW) 1.0 ± 0.3 and 0.6 ± 0.3, p=0.001; SUV Max (BSA) 0.2 ± 0.1 and 02 ± 0.1 p=0.001; SUV Max (AC) 3250.6 ± 1562.3 and 1667.3 ± 763.4; P=0.002.

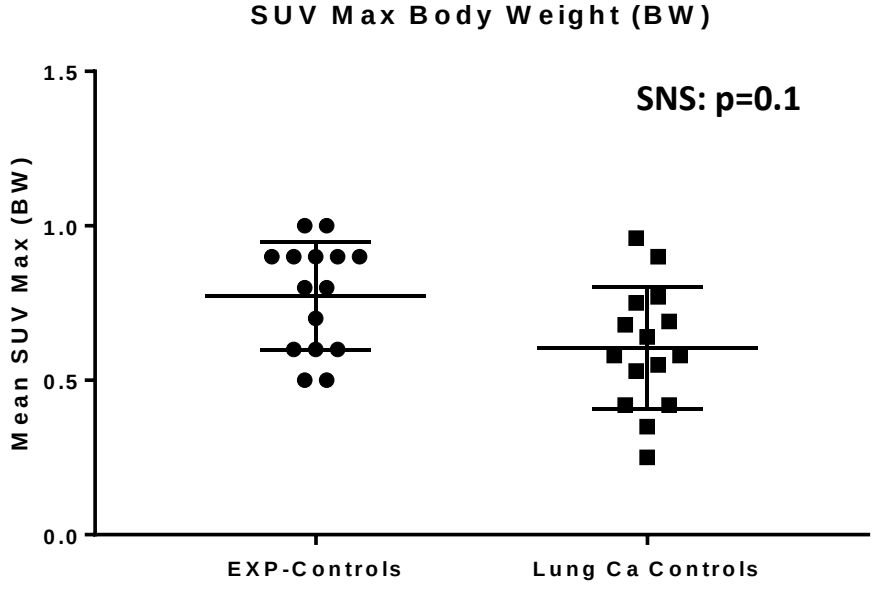

Fig 42: The comparison of the average of all 4 normal ROIs in lung cancer controls and 4 normal ROIs in extra-pulmonary cancer controls normalized with body weight (BW).

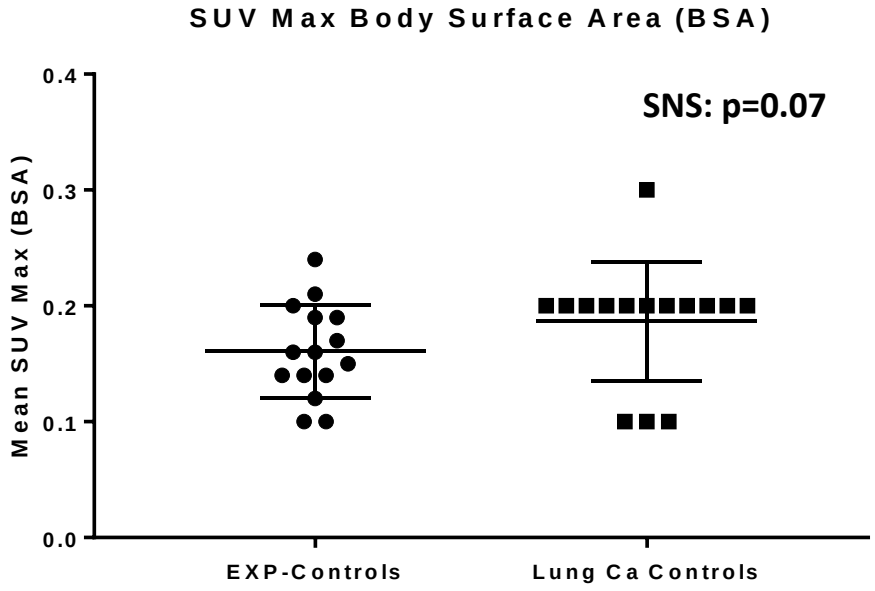

Fig 43: The comparison of the average of all 4 normal ROIs in lung cancer controls and 4 normal ROIs in extra-pulmonary cancer controls normalized with body surface area (BSA).

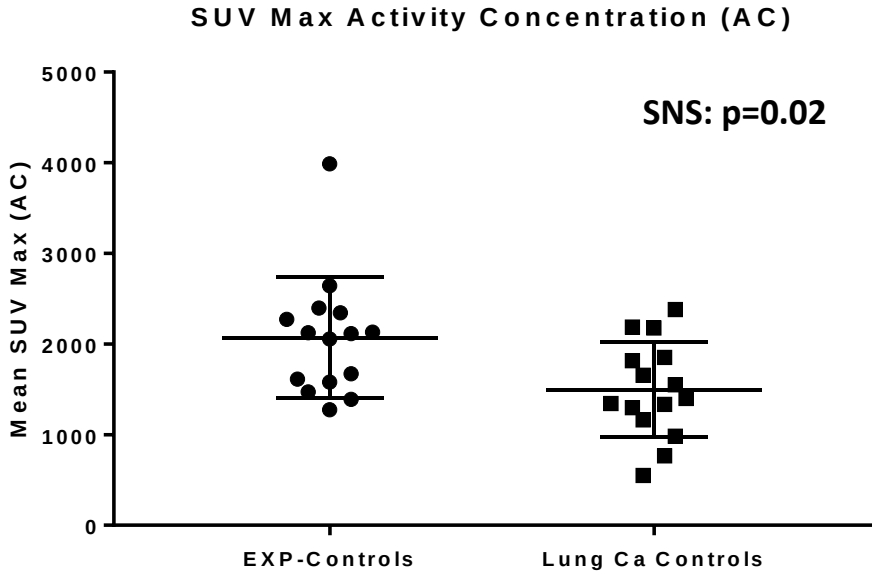

Fig 44: The comparison of the average of all 4 normal ROIs in lung cancer controls and 4 normal ROIs in extra-pulmonary cancer controls normalized with activity concentration (AC).

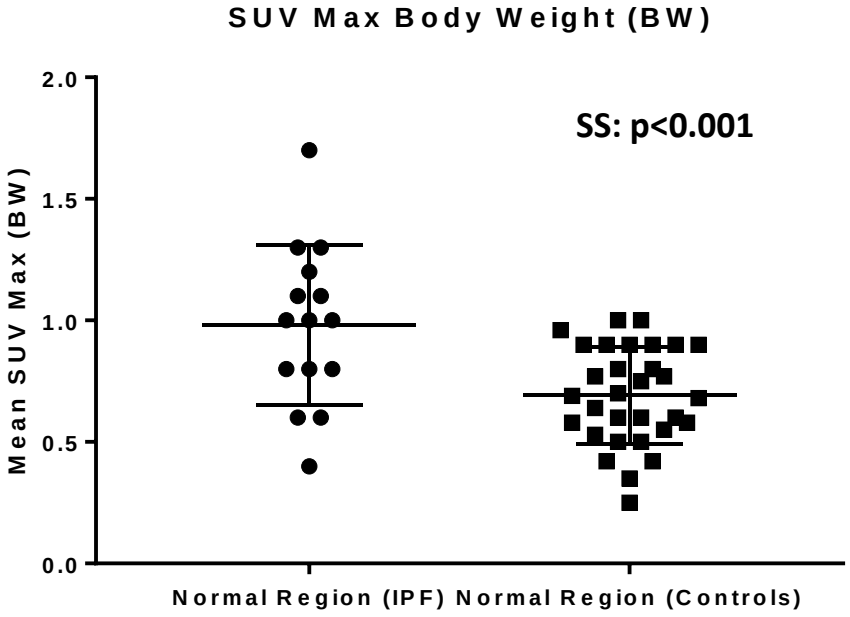

Fig 45: The comparison of the average of all 4 normal ROIs in IPF and 4 normal ROIs in controls normalized with body weight (BW).

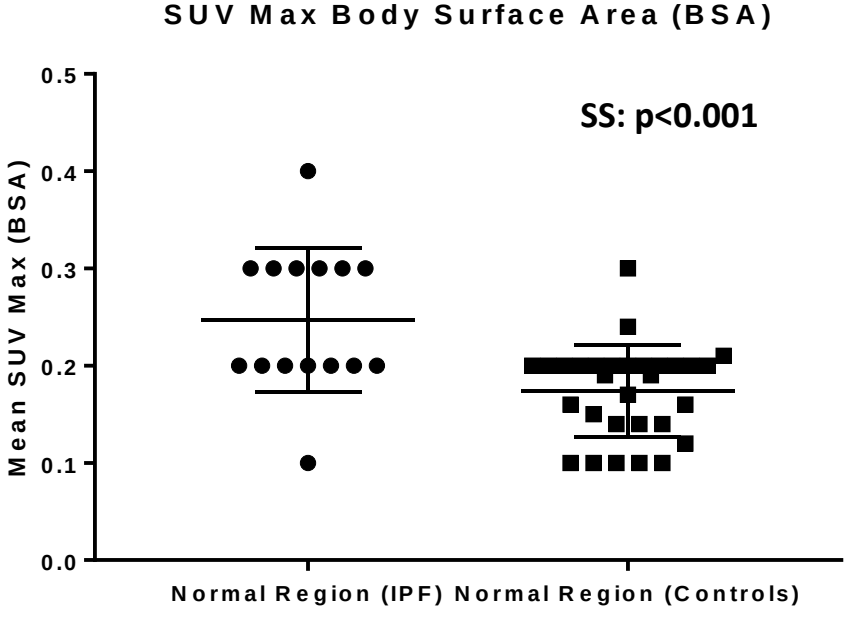

Fig 46: The comparison of the average of all 4 normal ROIs in IPF and 4 normal ROIs in controls normalized with body surface area (BSA).

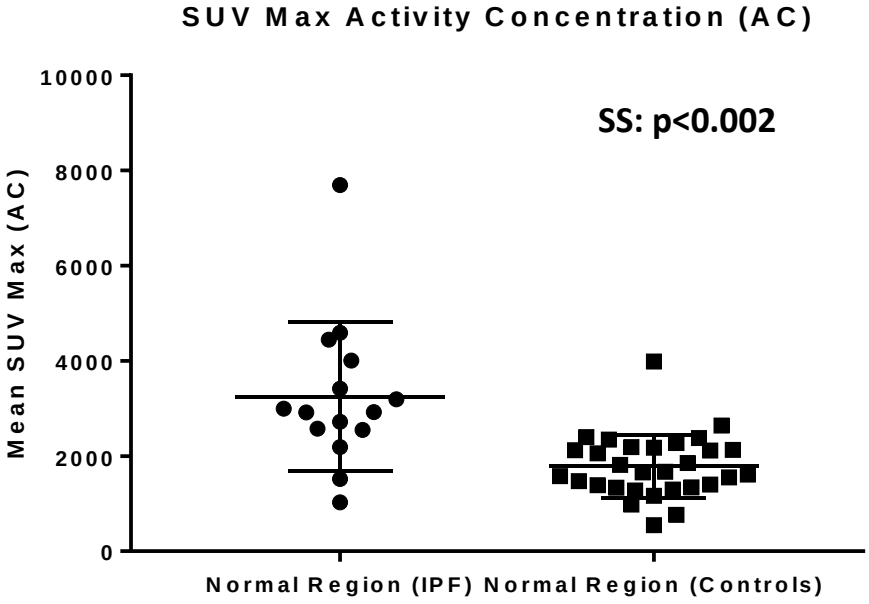

Fig 47: The comparison of the average of all 4 normal ROIs in IPF and 4 normal ROIs in controls normalized with Activity Concentration (AC).

Moreover, there are significant differences in SUV Mean between IPF and lung Ca controls in all the 3 normalization methods (Fig 48, 49 and 50); SUV Mean (BW) 0.8 ± 0.5 ± 0.2, p<0.001; SUV Mean (BSA) 0.2 ± 0.1 and 0.1 ± 0.04, p=0.001; SUV Mean (AC) 2560.5 ± 1392.4 and 1204.5 ± 400.3) P<0.001. there is also a significant differences between IPF and extra-pulmonary controls in activity concentration normalization (Fig 51) of SUV Mean (AC) 2560.5 ± 1392.4 and 1636.2 ± 628.7) P=0.004 However, no difference in SUV mean uptake is found between IPF and extra-pulmonary controls in SUV (BW) and SUV (BSA) (Fig 52 and 53). SUV Mean (BW) 0.8 ± 0.3 and 0.7 ± 0.2, p=0.1; SUV Mean (BSA) 0.2 ± 0.1 and 0.2 ± 0.03, p=0.05.

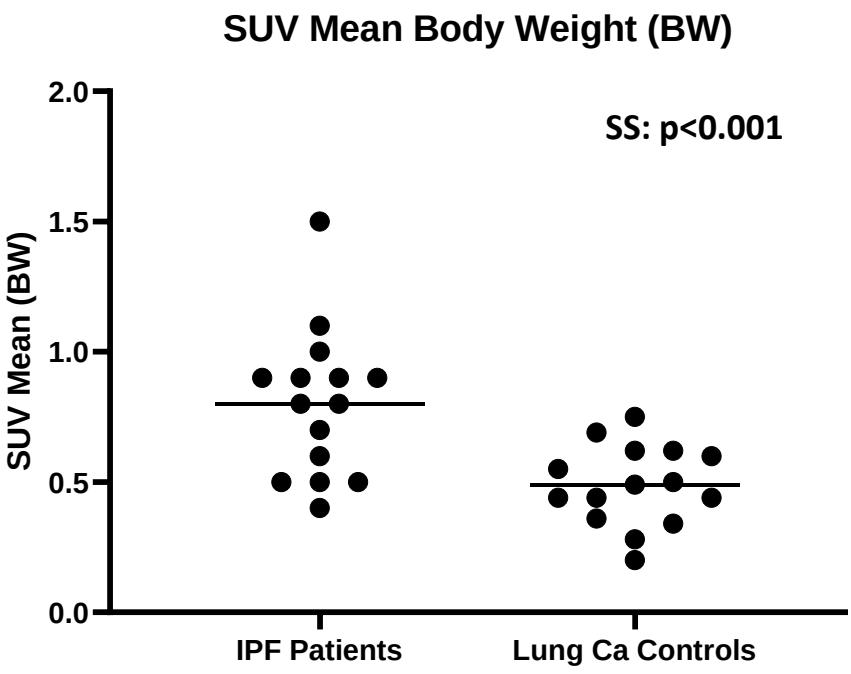

Fig 48: The comparison of the average of all 4 normal ROIs in IPF and 4 normal ROIs in lung Ca controls normalized with body weight (BW).

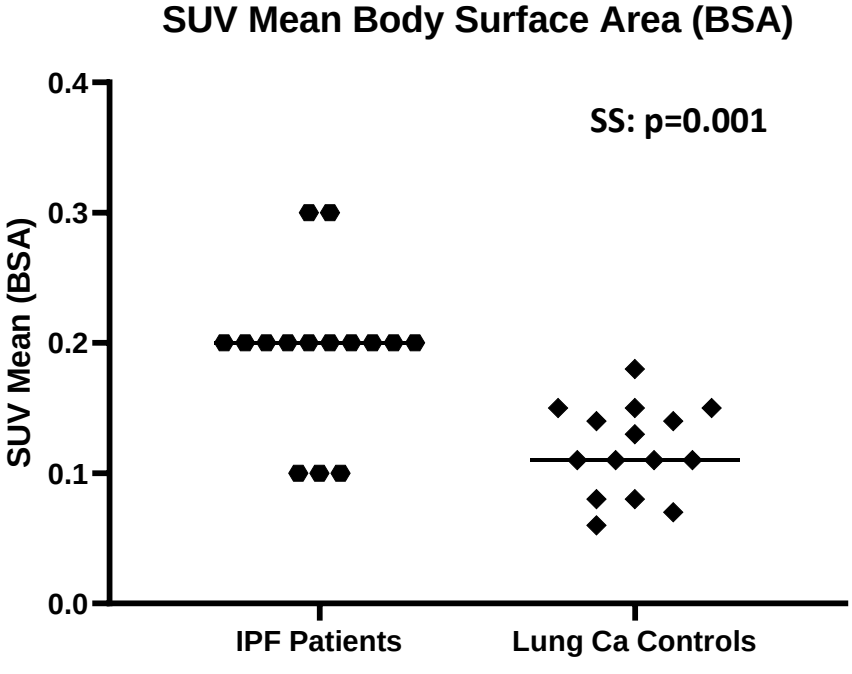

Fig 49: The comparison of the average of all 4 normal ROIs in IPF and 4 normal ROIs in lung Ca controls normalized with body surface area (BSA).

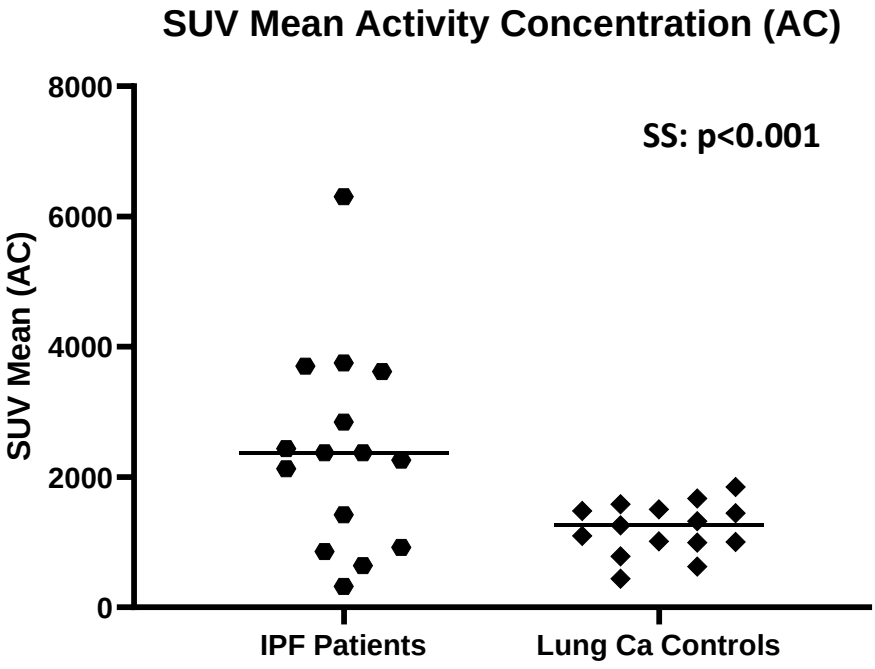

Fig 50: The comparison of the average of all 4 normal ROIs in IPF and 4 normal ROIs in lung Ca controls normalized with Activity Concentration (AC).

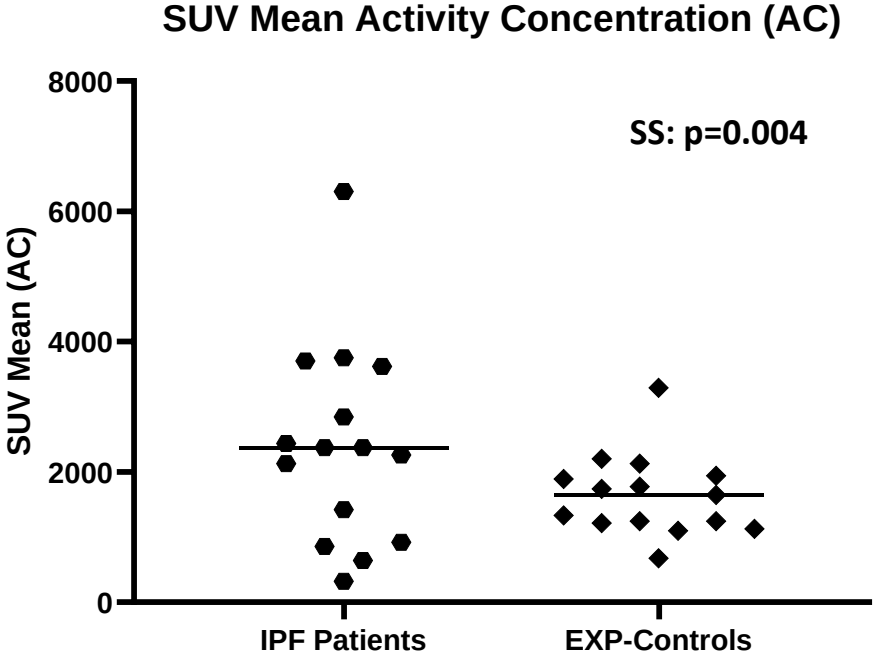

Fig 51: The comparison of the average of all 4 normal ROIs in IPF and 4

normal ROIs in extra-pulmonary controls normalized with Activity Concentration (AC).

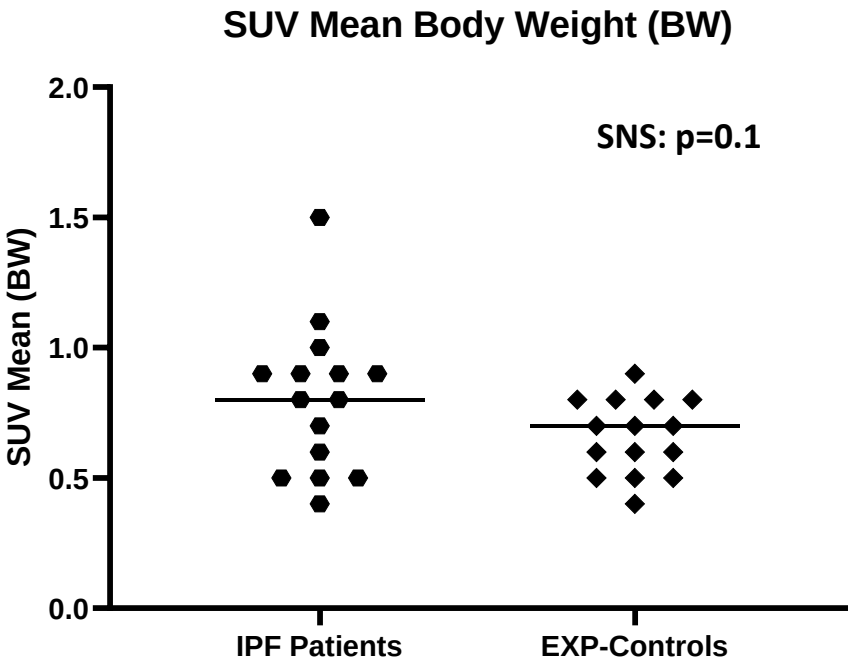

Fig 52: The comparison of the average of all 4 normal ROIs in IPF and 4 normal ROIs in extra-pulmonary controls normalized with body Weight (BW).

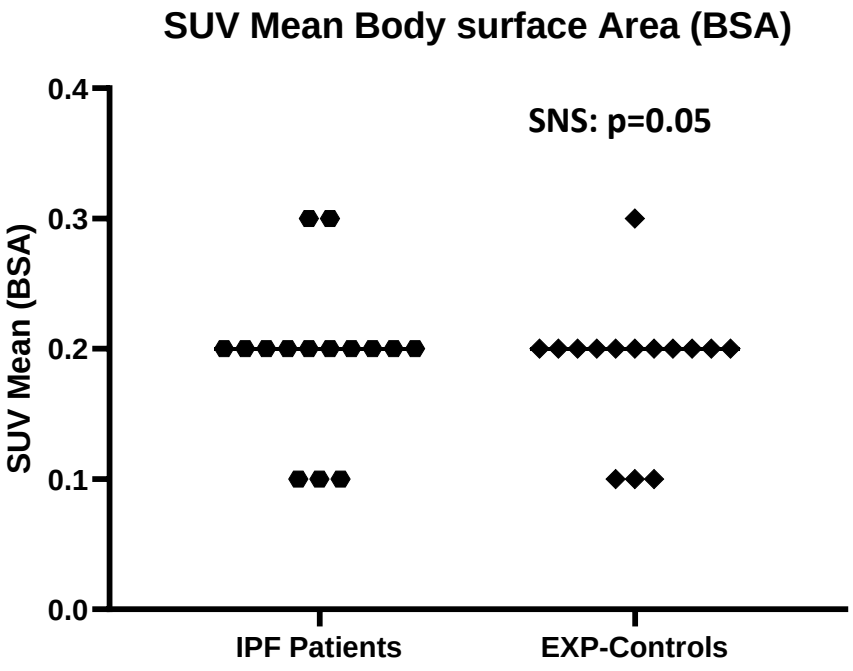

Fig 53: The comparison of the average of all 4 normal ROIs in IPF and 4 normal ROIs in extra-pulmonary controls normalized with body surface area (BSA).

The 2 anterior and 2 posterior ROIs has presented a significant different in their SUV Max and SUV Mean in all the 3 normalizations (BW< BSA and AC) SUV Max (BW) <0.001, r=43; SUV Max (BSA) p< 0.001, r=37; SUV Max (AC) p<0.001, r=70. SUV Max (BW) <0.001, r=55; SUV Max (BSA) p< 0.001, r=53; SUV Max (AC) p<0.001, r=75 (Fig 54-59).

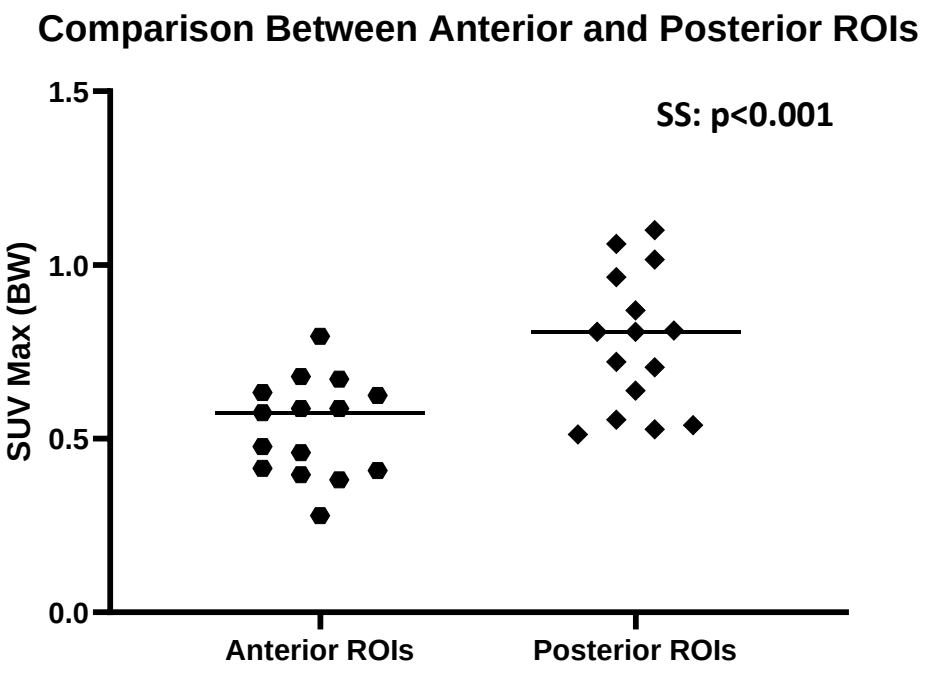

Fig 54: Comparison between the mean of 2 anterior and 2 posterior ROIs with normal lung in IPF patients.

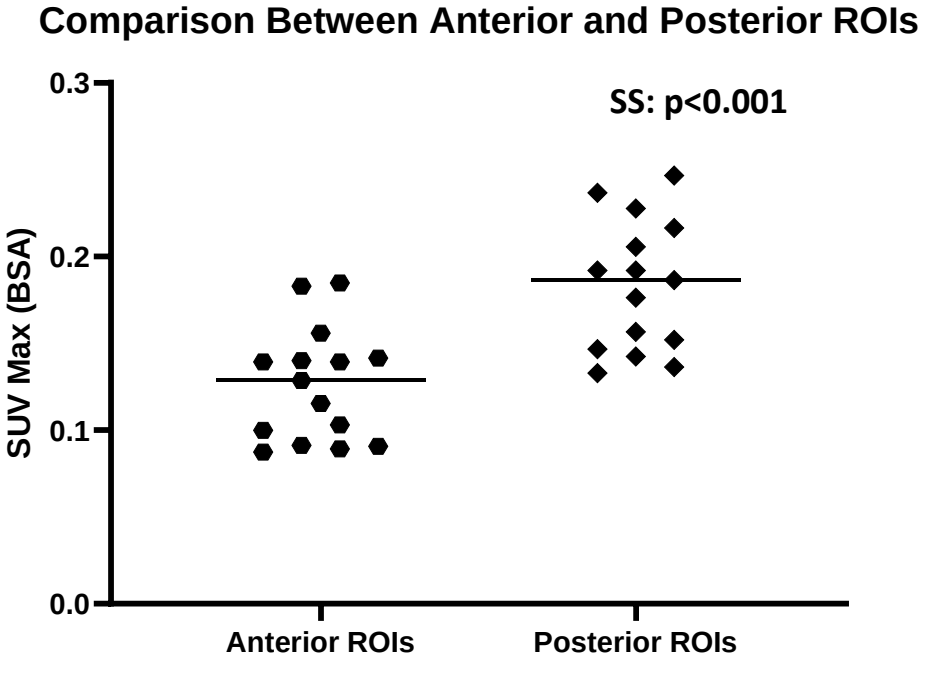

Fig 55: Comparison between the mean of 2 anterior and 2 posterior ROIs with normal lung in IPF patients.

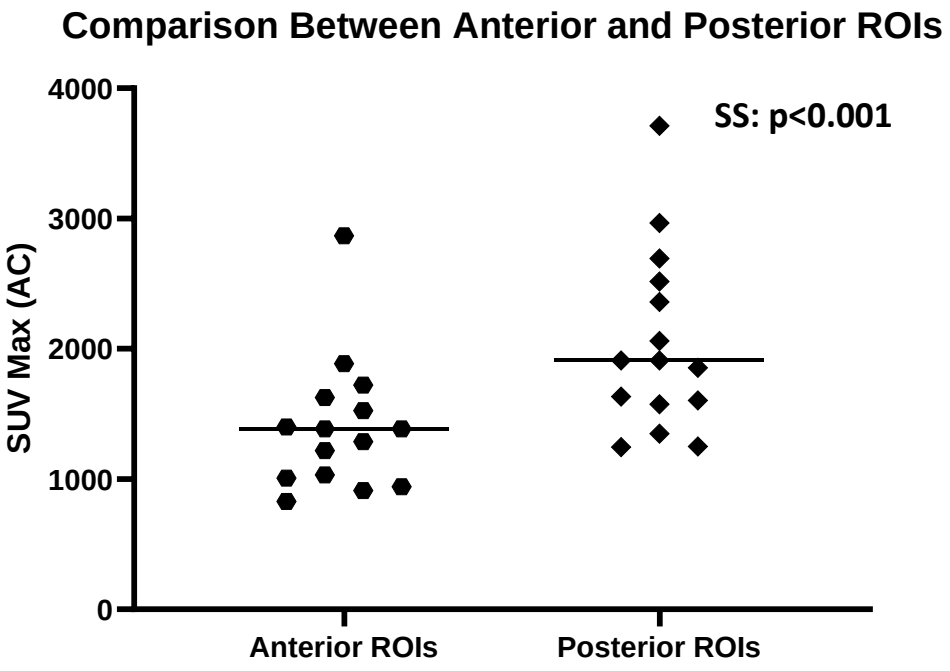

Fig 56: Comparison between the mean of 2 anterior and 2 posterior ROIs with normal lung in IPF patients.

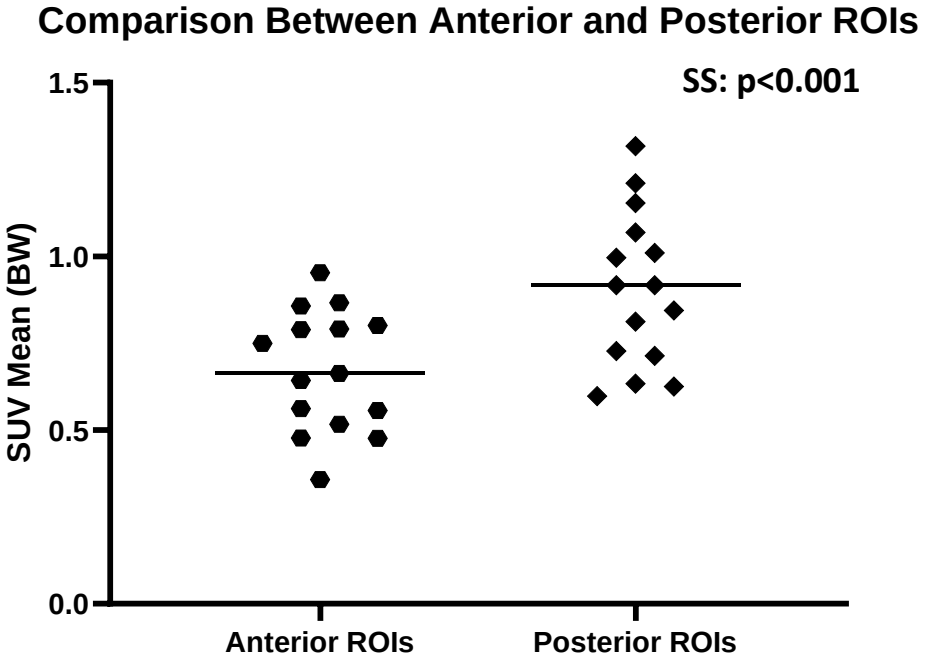

Fig 57: Comparison between the mean of 2 anterior and 2 posterior ROIs with normal lung in IPF patients.

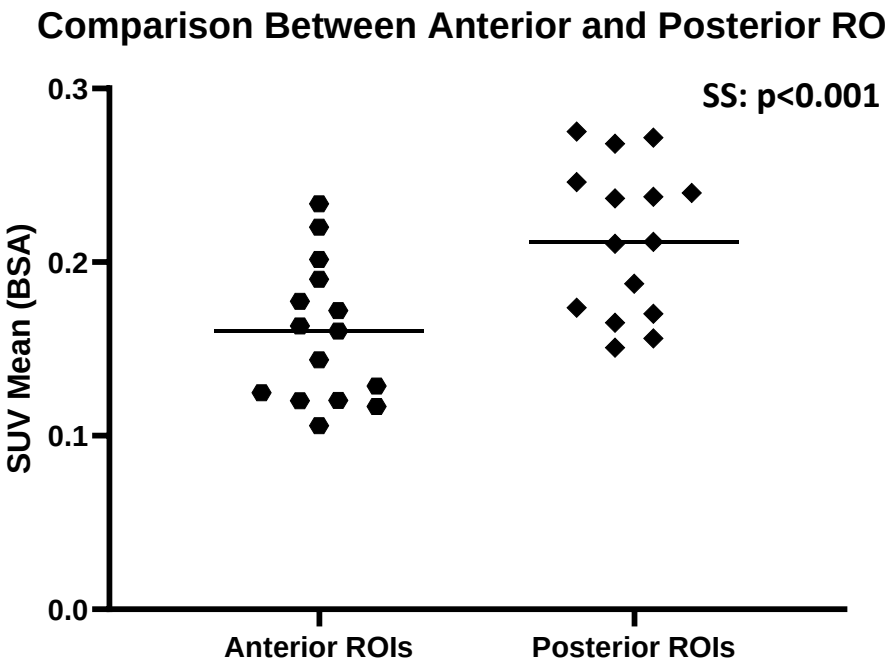

Fig 58: Comparison between the mean of 2 anterior and 2 posterior ROIs with normal lung in IPF patients.

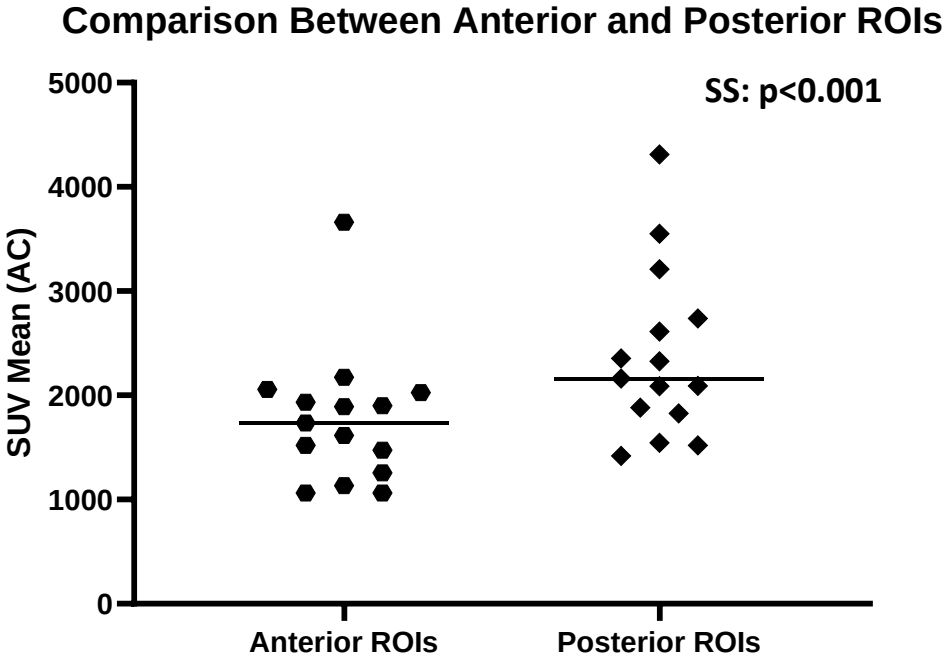

Fig 59: Comparison between the mean of 2 anterior and 2 posterior ROIs with normal lung in IPF patients.

Normal lung has the lowest maximum [^{18}F]-FDG uptake compared with the fibrotic lung, MBP and liver in all the 3 normalization. Normal lung SUV Max (BW) 1.0 ± 0.3, fibrotic lung SUV Max (BW) 2.1 ± 0.5, MBP SUV Max (BW) 2.4 ± 0.4 and liver SUV Max (BW) 3.0 ± 0.5; Normal lung SUV Max (BSA) 0.2 ± 0.07, fibrotic lung SUV Max (BSA) 0.5 ± 0.14, MBP SUV Max (BSA) 0.6 ± 0.10 and liver SUV Max (BSA) 0.7 ± 0.08; Normal lung SUV Max (AC) 3250.6 ± 1509.3, fibrotic lung SUV Max (AC) 7078.2 ± 3446.7, MBP SUV Max (AC) 7659.7 ± 2353.8 and liver SUV Max (AC) 9727.9 ± 3236.7 (Fig 60-62).

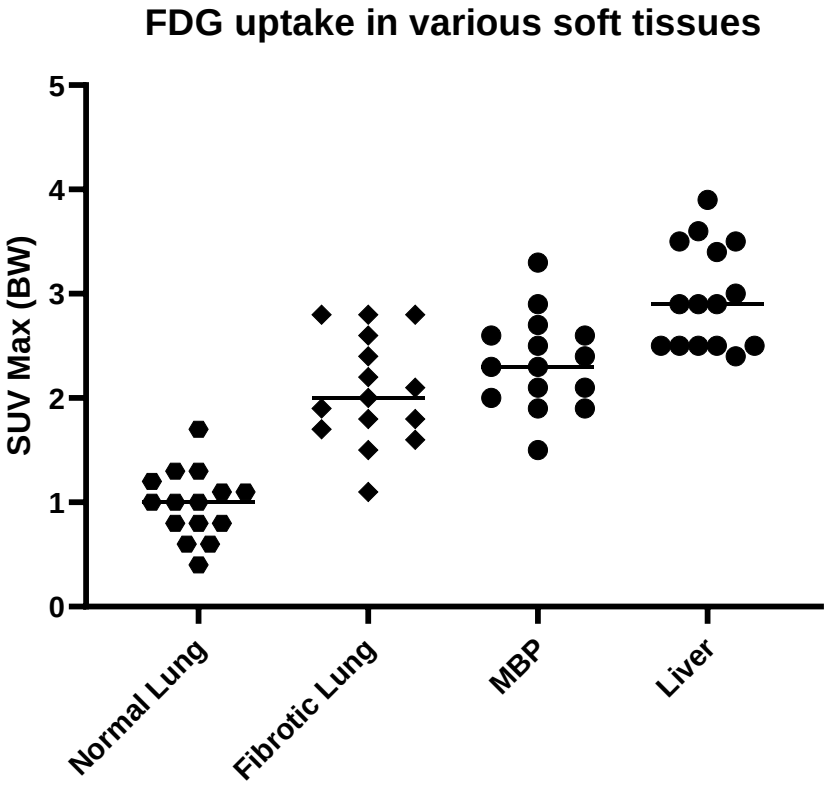

Fig 60: Comparison of FDG uptake between normal lung, fibrotic lung, MBP and liver in IPF patients.

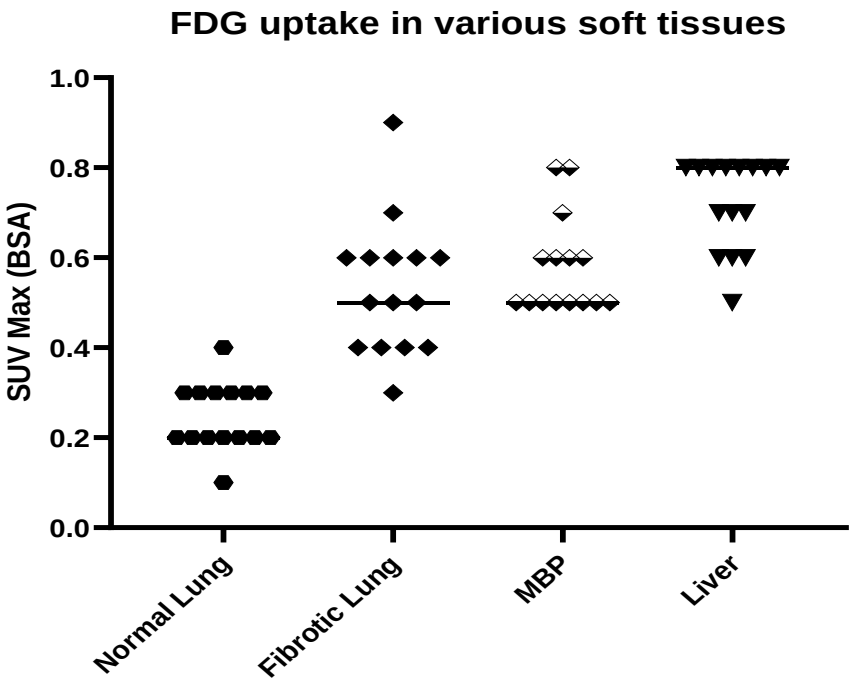

Fig 61: Comparison of [^{18}F]-FDG uptake between normal lung, fibrotic lung, MBP and liver in IPF patients.

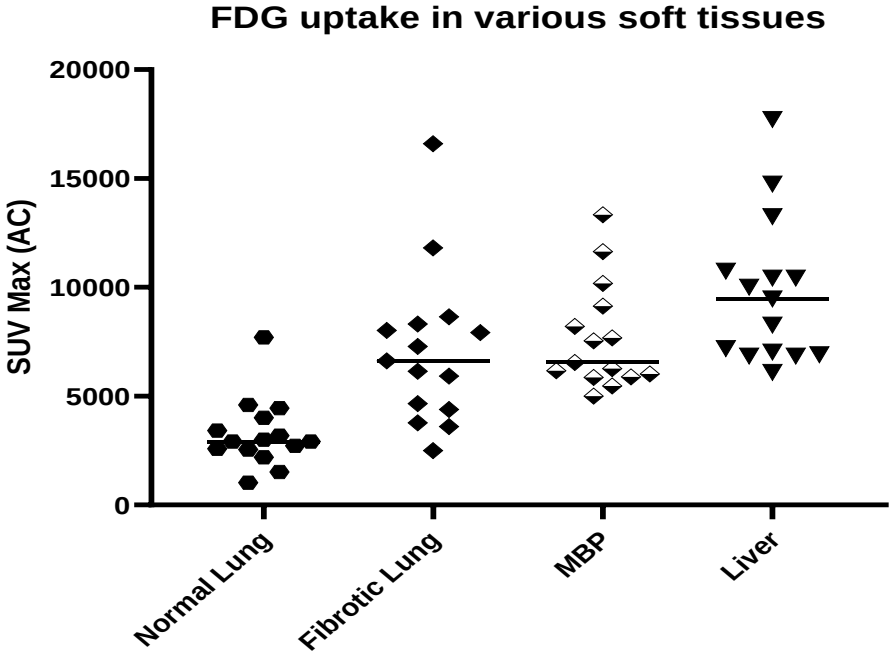

Fig 62: Comparison of [^{18}F]-FDG uptake between normal lung, fibrotic lung, MBP and liver in IPF patients.

There was no significant differences in the maximum and mean CT number in the normal regions of the two control groups (Fig 63 and 64), Max CT number -530.6 ± 61.2 and -593.3 ± 53.4, p=0.11; mean CT number -677.2 ± 164.9 and -769.4 ± 198.4, p-value=0.09 as such the 2 groups were pooled for comparison with normal regions in IPF patients (65 and 66) max CT number -471.7 ± 73.5 and -561.9 ± 108.3, p=0.05; mean CT number -719.4 ± 36.5 and -723.3 ± 146.6, p=0.9.

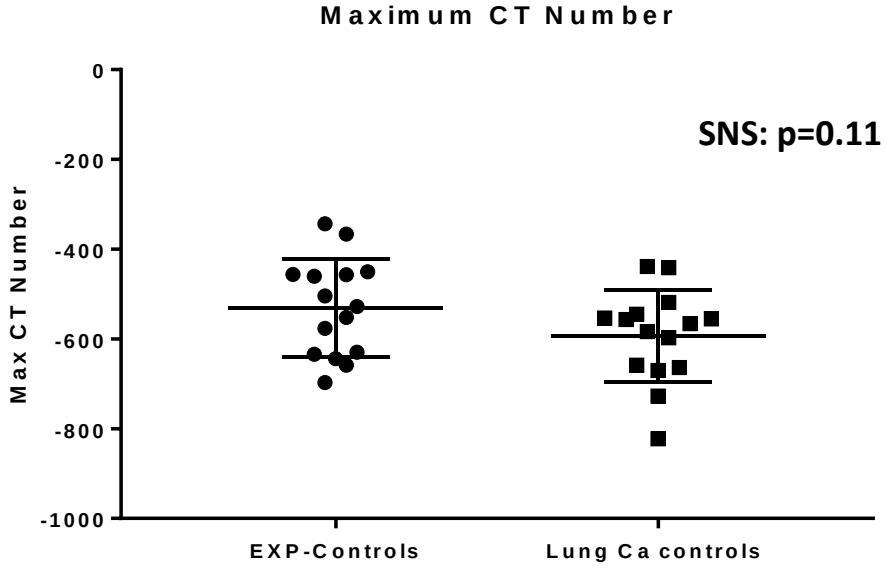

Fig 63: The comparison of the average maximum CT number (Hounsfield unit) of all 4 ROIs in extra-pulmonary controls and 4 ROIs in lung Ca controls.

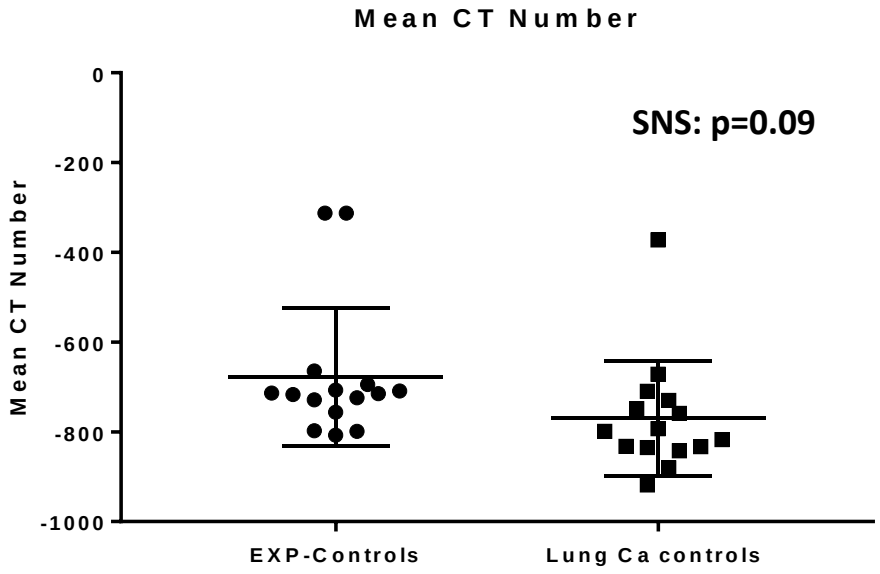

Fig 64: The comparison of the average mean CT number of all 4 ROIs in extra-pulmonary controls and 4 ROIs in lung Ca controls.

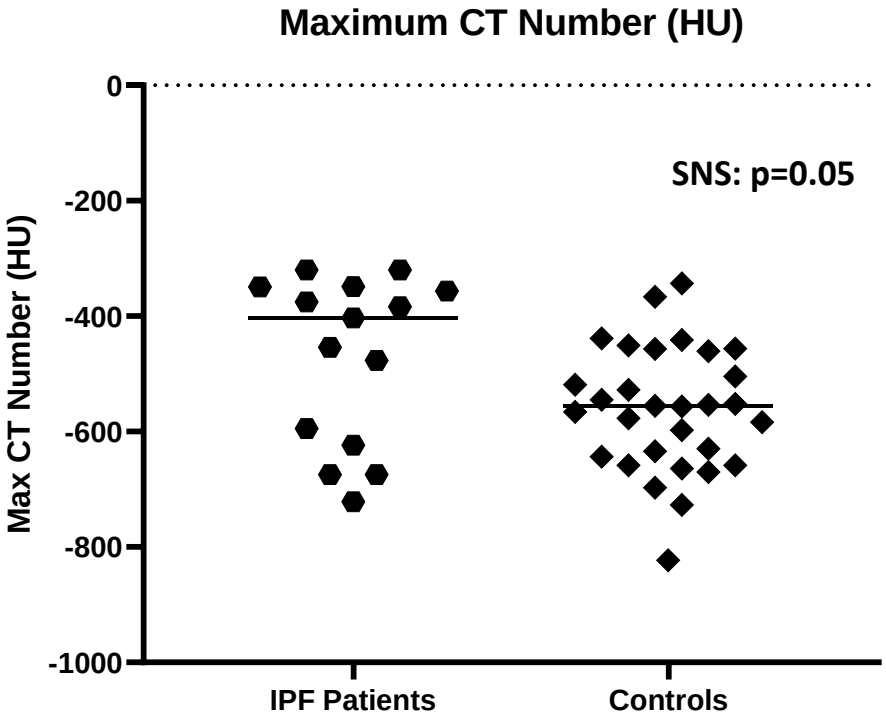

Fig 65: The comparison of the average maximum CT number of all 4 ROIs in IPF and controls.

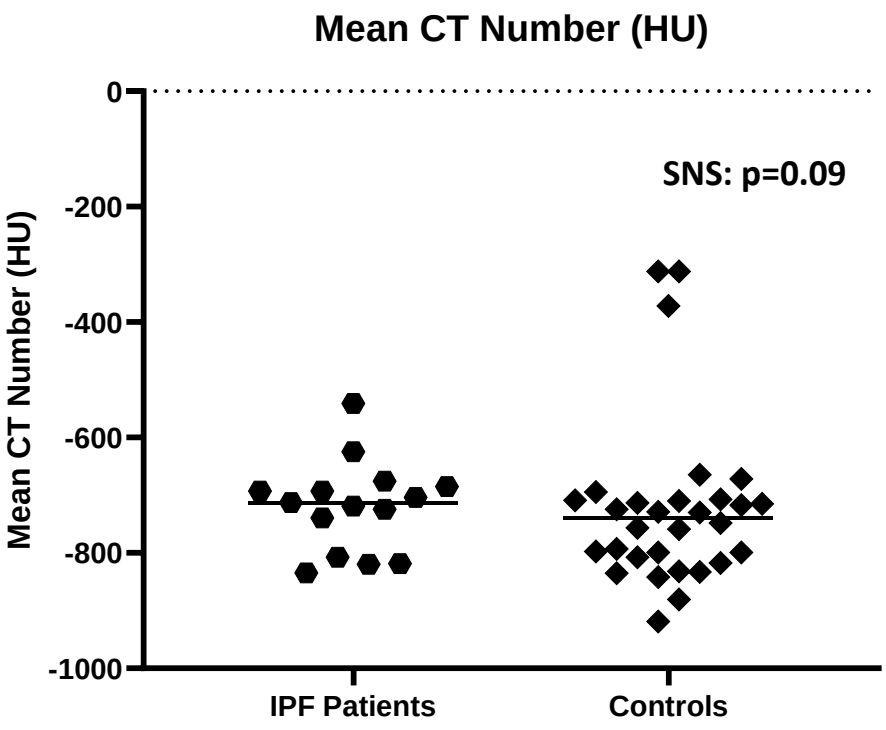

Fig 66: The comparison of the average mean CT number of all 4 ROIs in IPF and controls.

Only one out of twenty textural features within PET ROIs shows significant results when 2 controls normal lung were compared as such nineteen textural features were pooled together for comparison with IPF normal lung. Ten out of the nineteen textural features demonstrated significant differences when compared with IPF normal lung. However, five out of the twenty CT textural features shows significant differences between the 2 controls normal lung as such, they were excluded. Fifteen were pooled together for comparison with IPF normal lung. Five out of the fifteen CT textural features shows significant differences when compared with IPF normal lung and all are consistent with five features that shows significant difference in PET dataset (Fig 67-76). PET LoG (3.84mm filter) 0.77 ± 0.12, and 0.92 ± 0.10, p=0.0002), CT LoG (3.84mm filter) 0.43 ± 0.13 and 0.60 ± 0.20 p=0.001; PET LoG (6.19mm filter) 0.87 ± 0.12 and 0.98 ± 0.05, p=0.002, CT LoG (6.19mm filter) 0.61 ± 0.16 and 0.77 ± 0.19, p=0.005; PET LawsTex L5L5 std 2309882.92 ±

1500113.67 and 1056837.70 ± 574153.90, p=0.005, CT LawsTex L5L5 std 333285.88 ± 102232.05 and 247596.41 ± 67752.78, p=0.01 and PET first order statistic (FOS) entropy 6.75 ± 0.57 and 6.04 ± 0.50, p=0.0003, CT FOS entropy 5.17 ± 0.29 and 4.89 ± 0.29, p=0.003, PET FOS Standard deviation (std) 310.08 ± 199.03 and 139.71 ± 76.62, p=0.0004, CT FOS std 54.46 ± 14.18 and 43.63 ± 11.96, p=0.01.

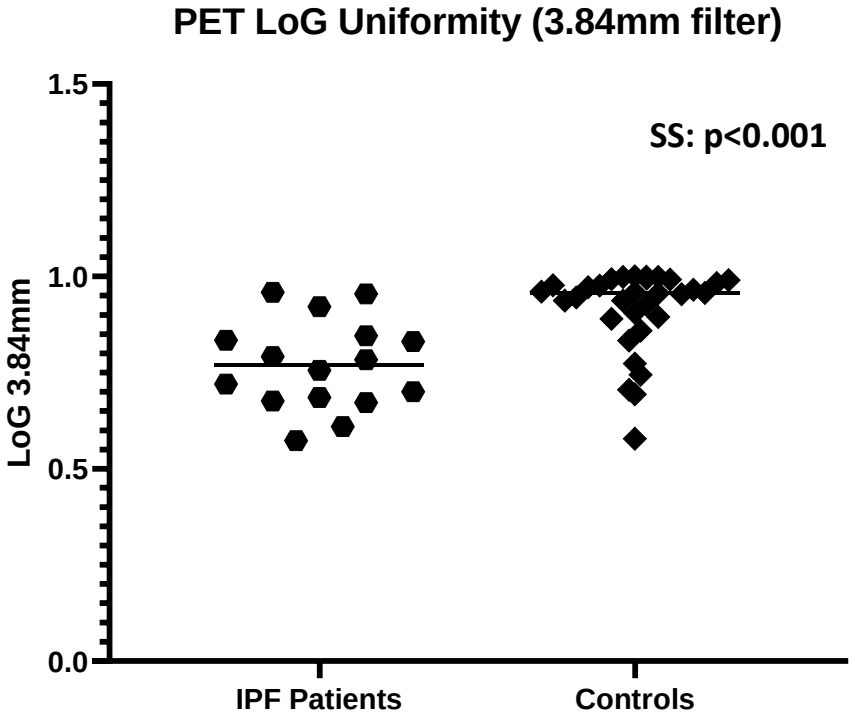

Fig 67: Laplacian of Gaussian (LoG) 3.84mm filter between IPF and controls with IPF widely distributed whereas in the control clustered above the mean.

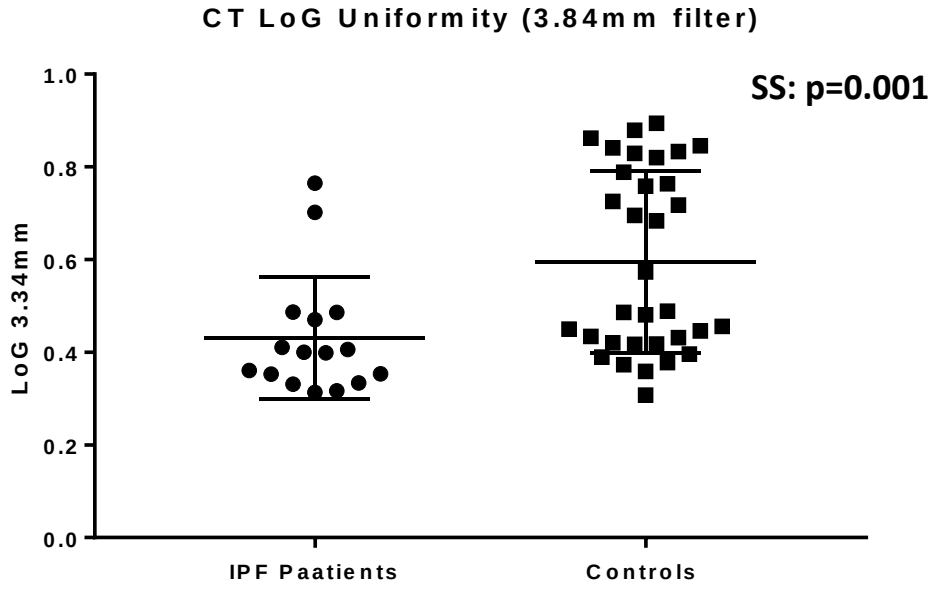

Fig 68: Laplacian of Gaussian (LoG) 3.84mm filter between IPF and controls with IPF widely distributed whereas in the control clustered above the mean.

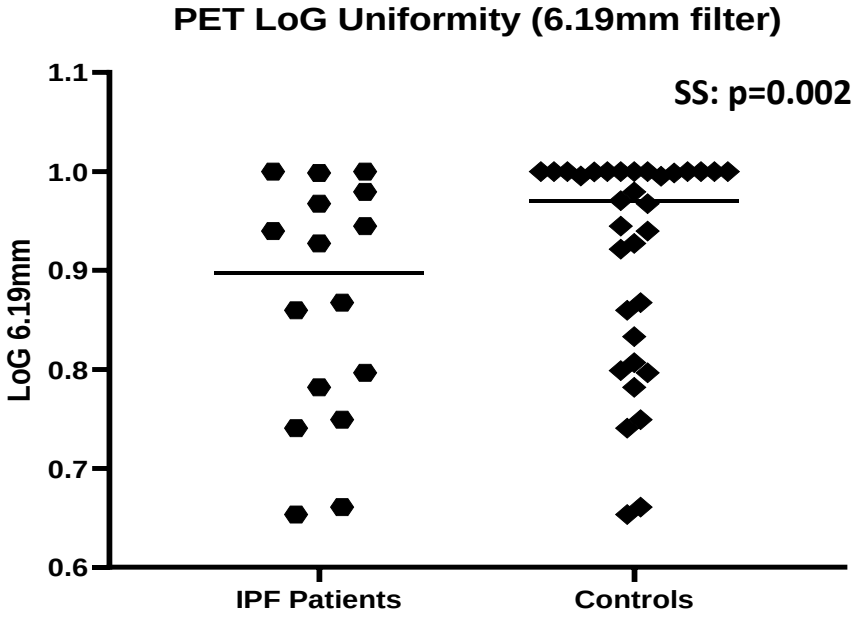

Fig 69: Laplacian of Gaussian (LoG) 6.19mm filter between IPF and controls with IPF widely distributed whereas in the control clustered above the mean.

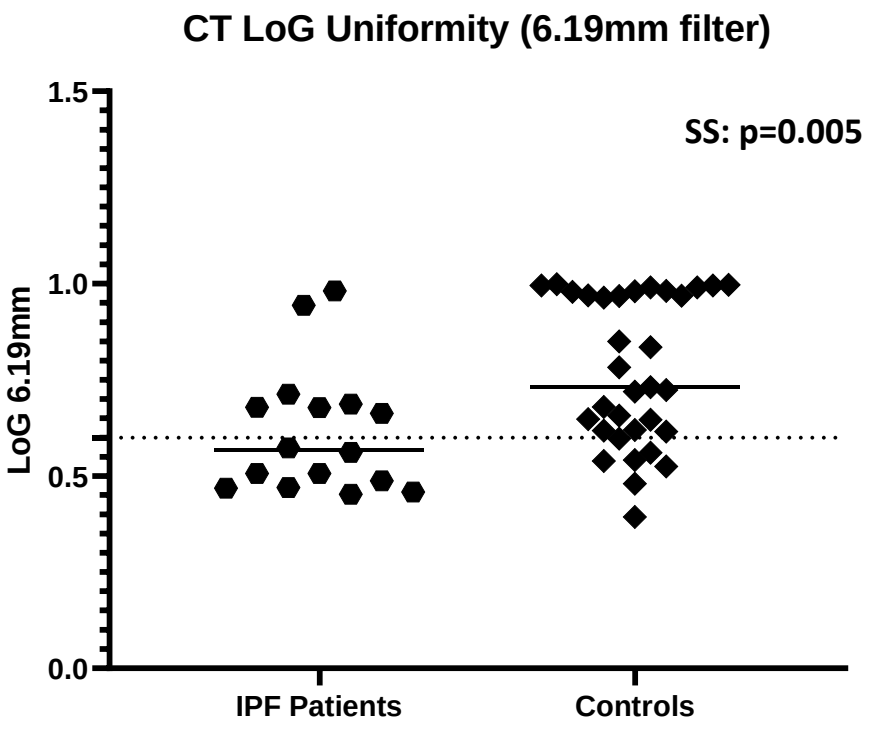

Fig 70: Laplacian of Gaussian (LoG) 6.19mm filter between IPF and controls with IPF widely distributed whereas in the control clustered above the mean.

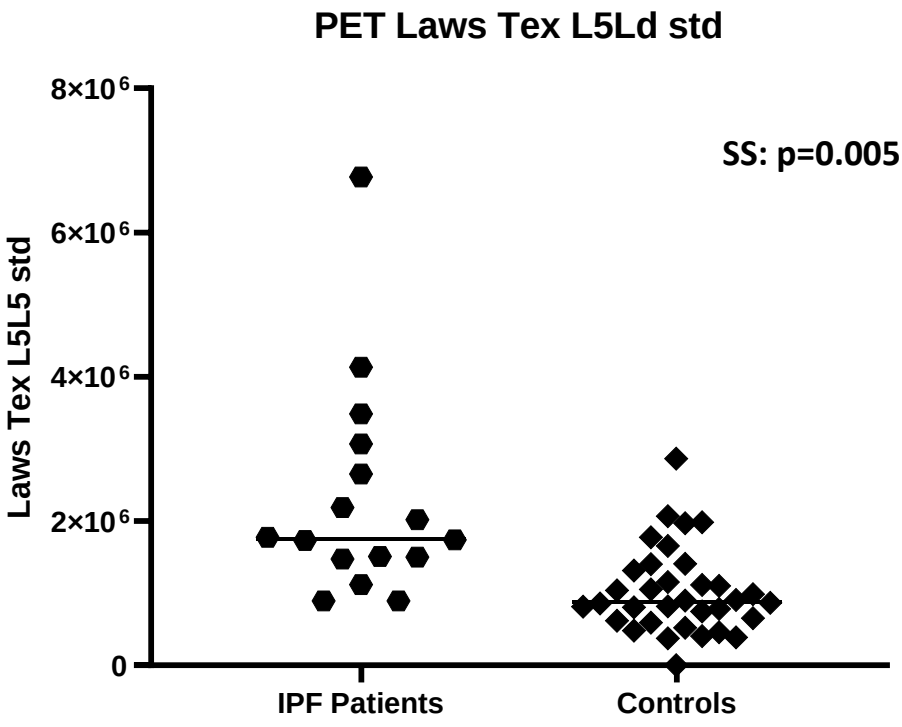

Fig 71: LawTex L5L5 std between IPF and controls with IPF widely distributed whereas in the control clustered above the mean.

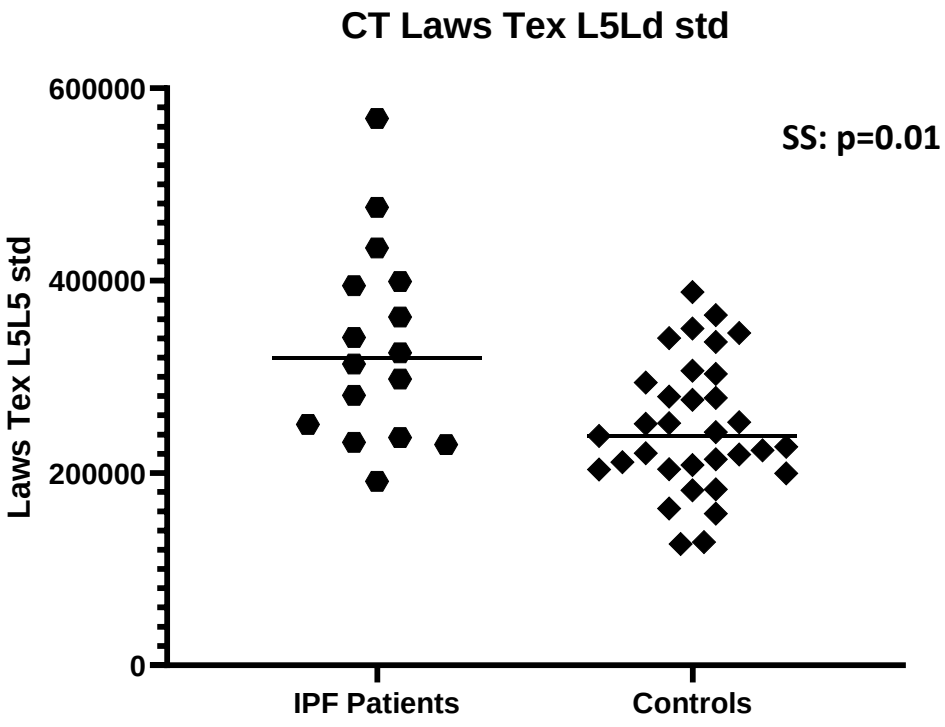

Fig 72: LawTex L5L5 std between IPF and controls with IPF widely distributed whereas in the control clustered above the mean.

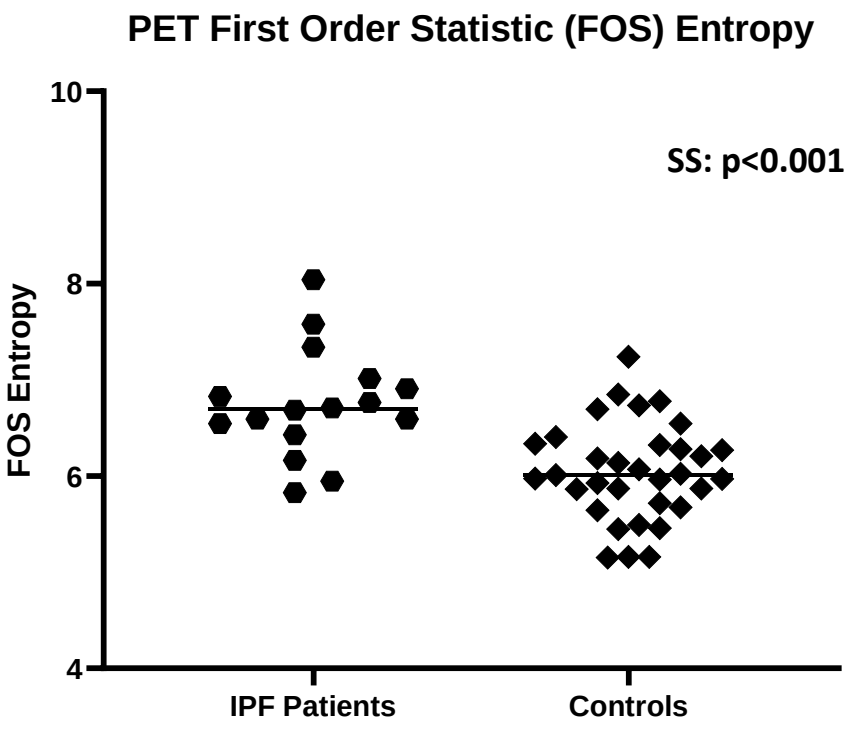

Fig 73: FOS Entropy between IPF and controls with IPF widely distributed whereas in the control clustered above the mean.

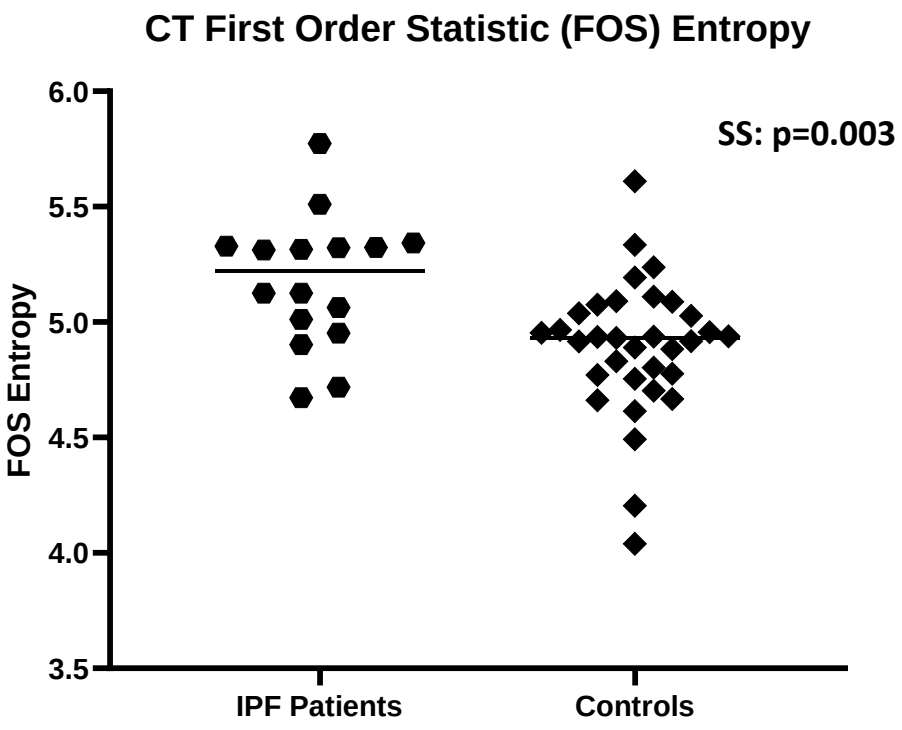

Fig 74: FOS Entropy between IPF and controls with IPF widely distributed whereas in the control clustered above the mean.

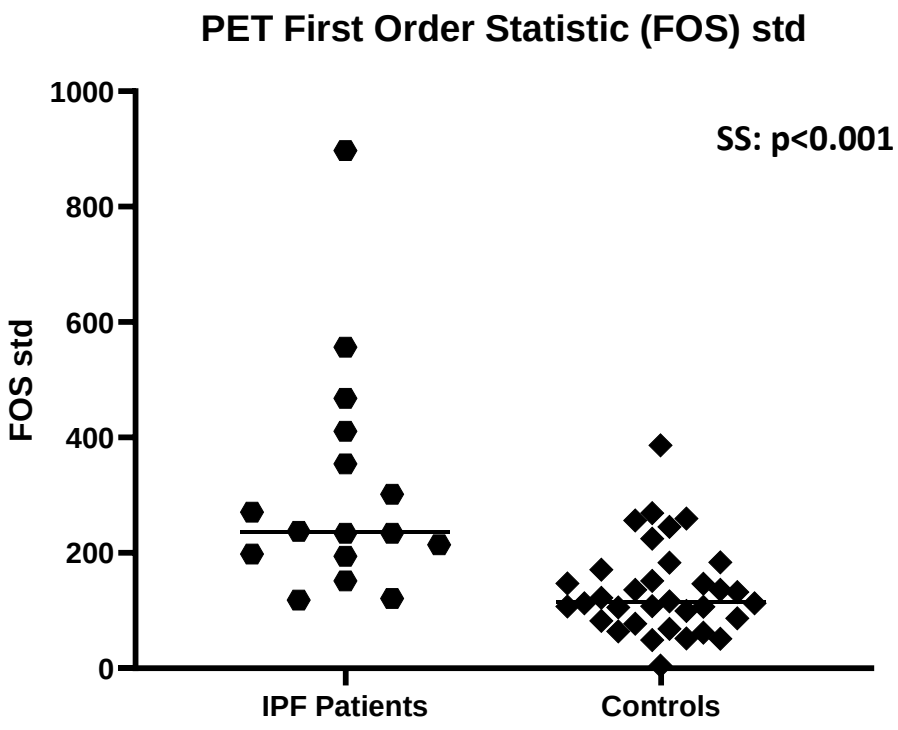

Fig 75: FOS std between IPF and controls with IPF widely distributed whereas in the control clustered above the mean.

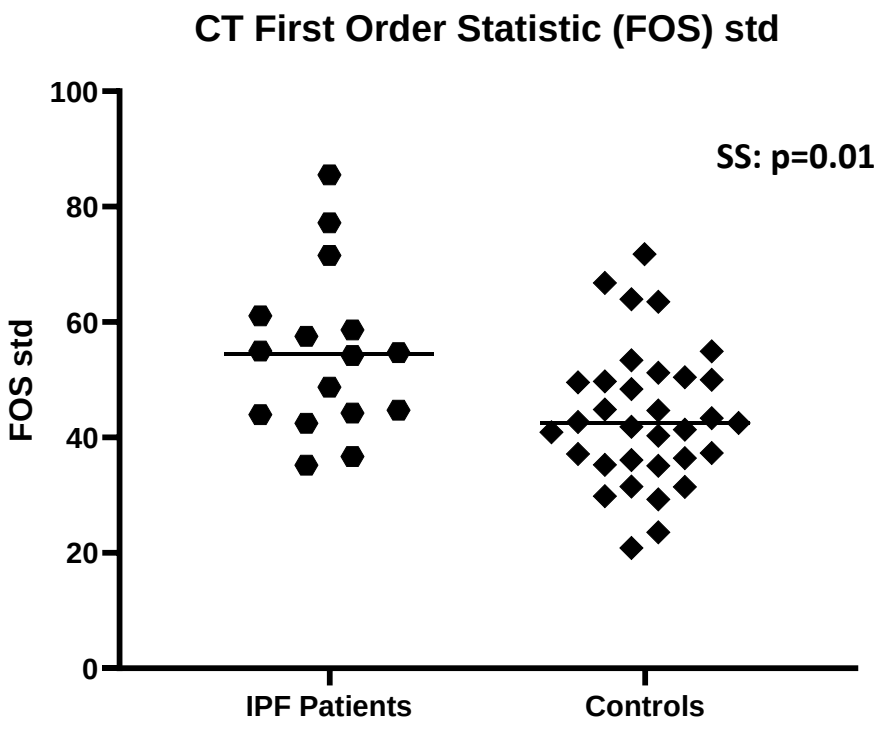

Fig 76: FOS std between IPF and controls with IPF widely distributed whereas in the control clustered above the mean.

When the above 5 textural features were compared against each other a range of different correlation between strong to weak correlation was found. There was a strong correlation between Laws Tex L5L5 std and FOS std, r=99; between FOS Entropy and FOS std, r=93; between Laws Tex L5L5 std and FOS entropy, r=92 and between LoG Uniformity (3.84mm filter and 6.19mm filters), r=87; (Fig 77-80). There is a very weak correlation between LoG Uniformity 3.84mm filter and FOS std, r=-63; between LoG Uniformity 3.84mm and Laws Tex L5L5 std, r=-51; between LoG Uniformity 6.19mm filter and Laws Tex L5L5 std, r=87; between LoG Uniformity 6.19mm filter and FOS std, r=-68; LoG Uniformity 6.19mm and FOS entropy, r=-80 and LoG Uniformity 3.84mm and FOS entropy, r=-80 (Fig 81-86).

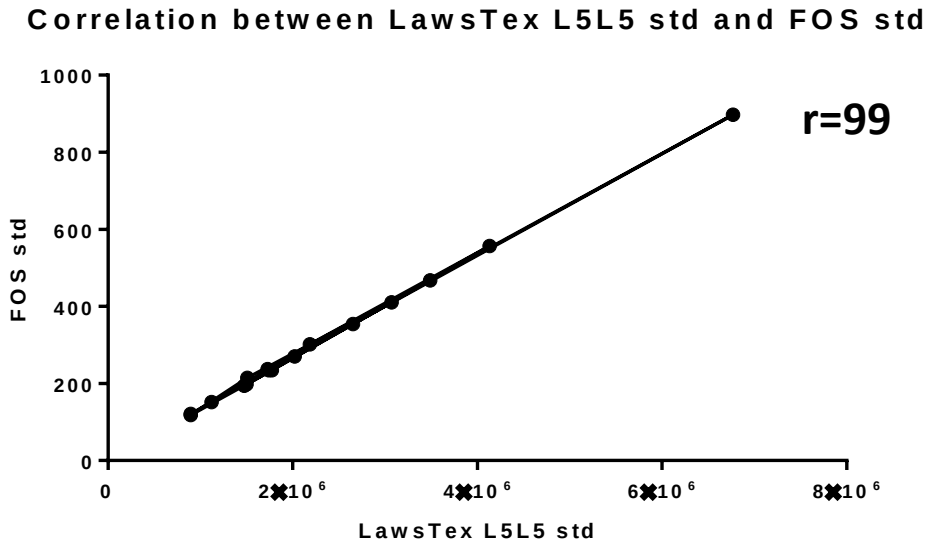

Fig 77: Correlation between Laws Tex L5L5 std and First order statistic (FOS) std.

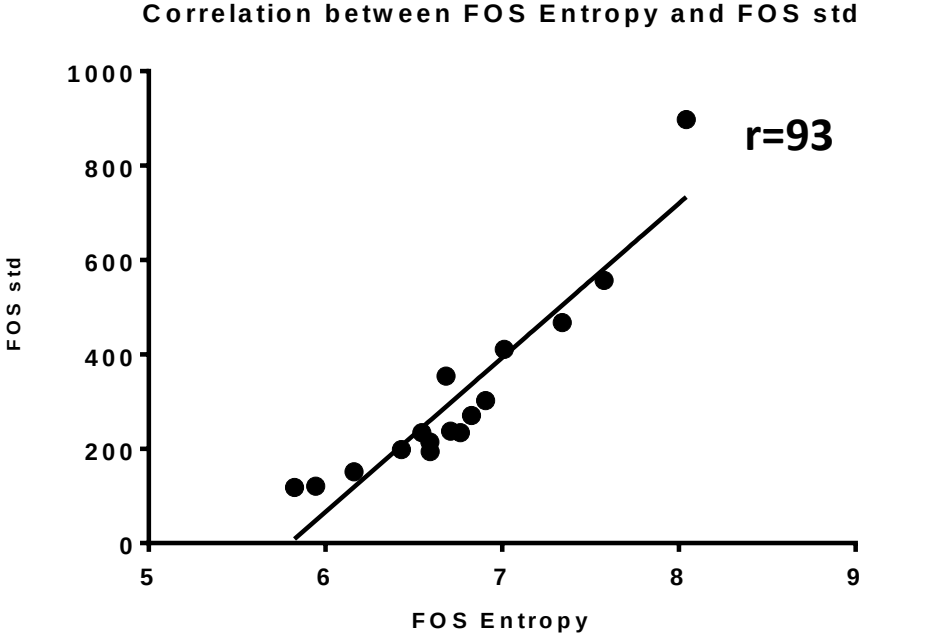

Fig 78: Correlation between first order statistic entropy and first order statistic (FOS) std

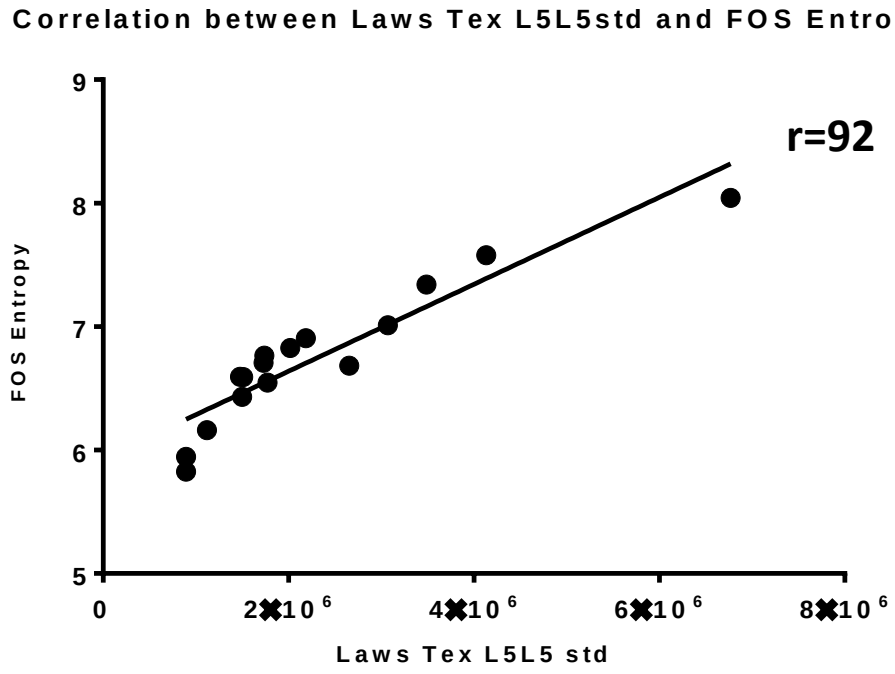

Fig 79: Correlation between Laws Tex L5L5 std and first order statistic entropy.

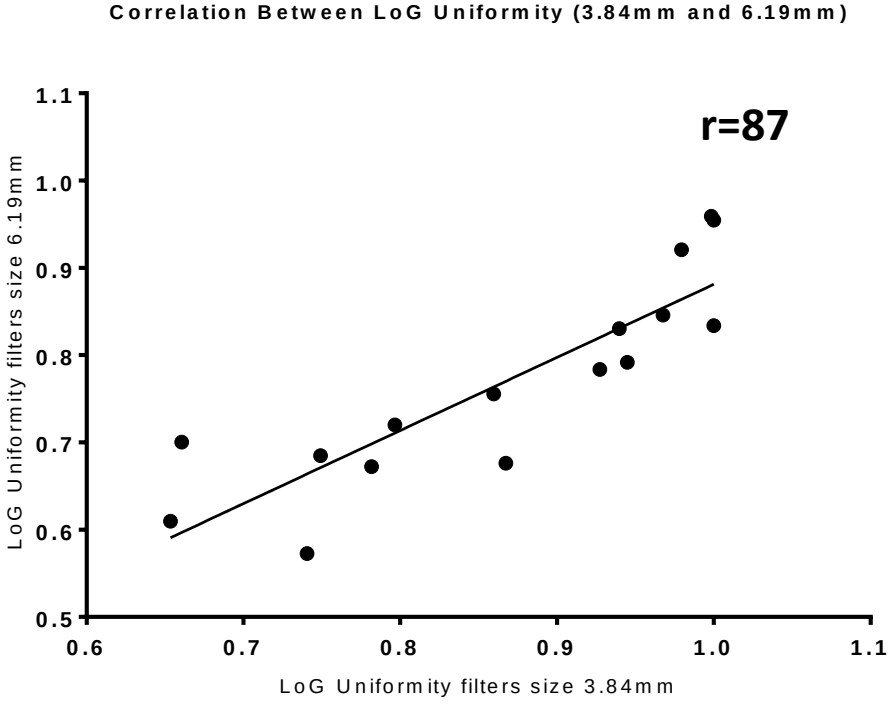

Fig 80: Correlation between LoG uniformity filter (3.84 and 6..19 mm) with strong positive correlation between the two filters.

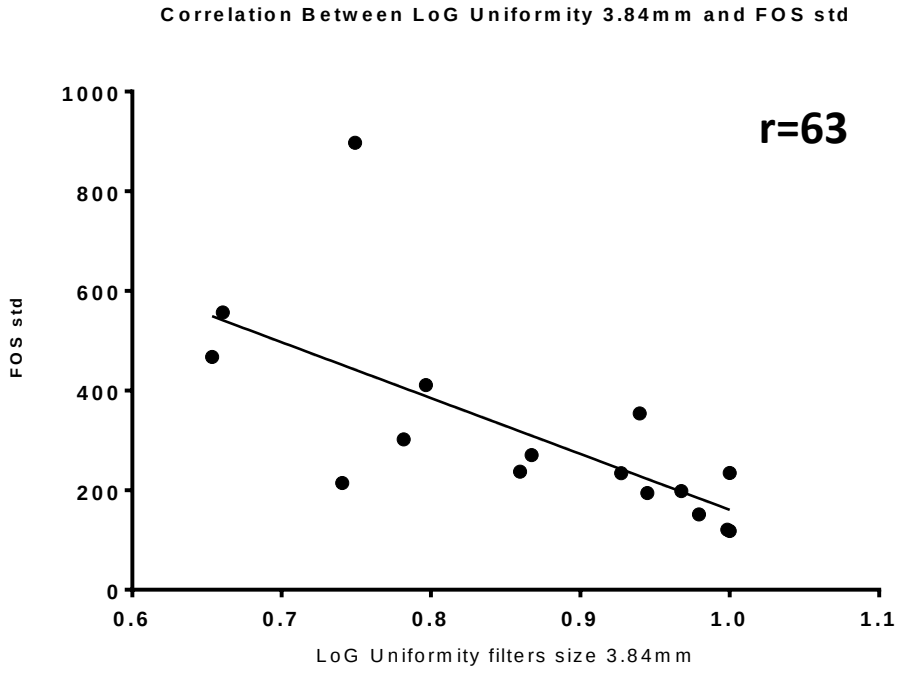

Fig 81: Correlation between LoG uniformity filter 3.84 mm and FOS std with negative correlation between them.

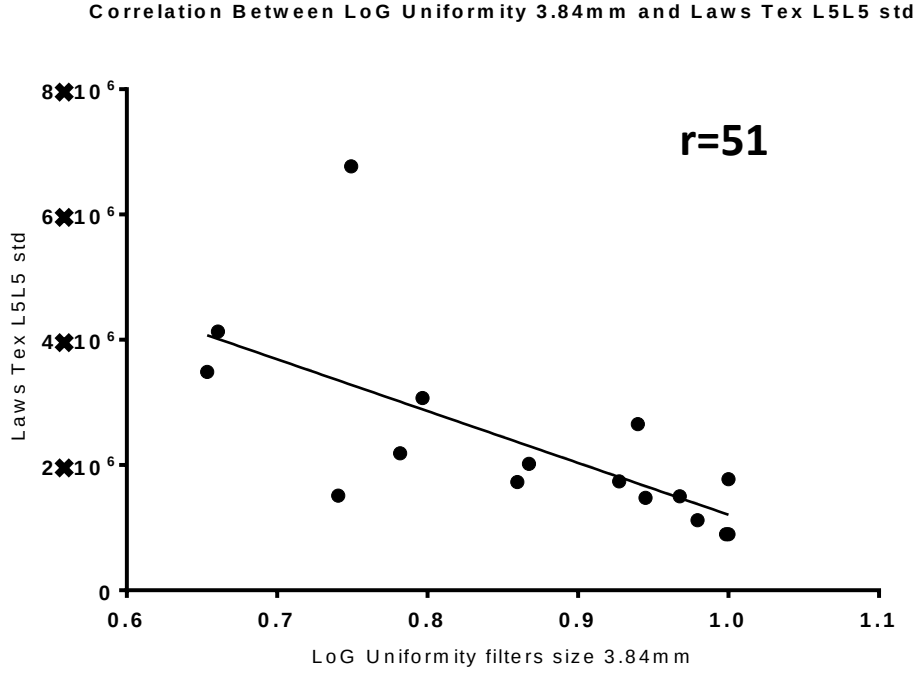

Fig 82: Correlation between LoG uniformity filter 3.84 mm and Laws Tex L5L5 std with negative correlation between them.

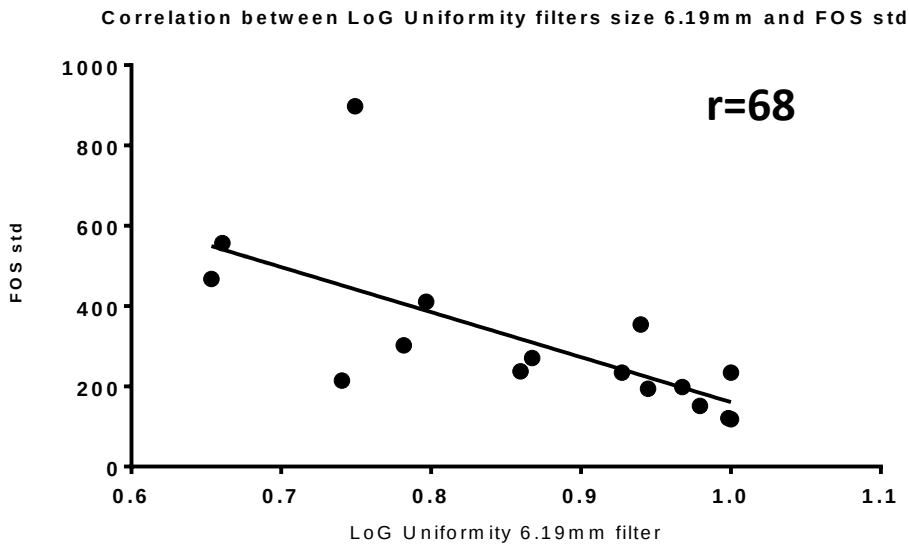

Fig 83: Correlation between LoG uniformity filter 6.19 mm and FOS std with negative correlation between them.

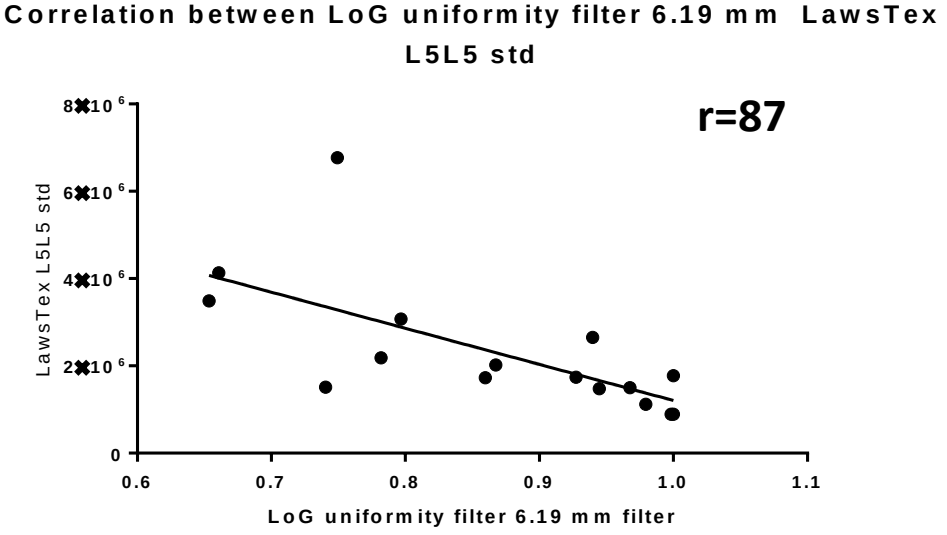

Fig 84: Correlation between LoG uniformity filter 6.19 mm and Laws Tex L5L5 std with negative correlation between them.

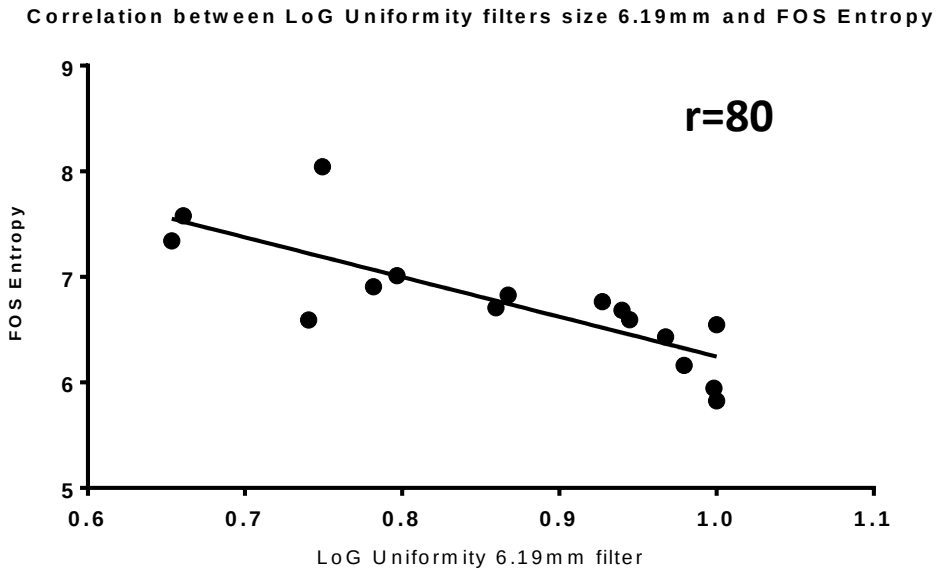

Fig 85: Correlation between LoG uniformity filter 6.19 mm and FOS entropy with negative correlation between them.

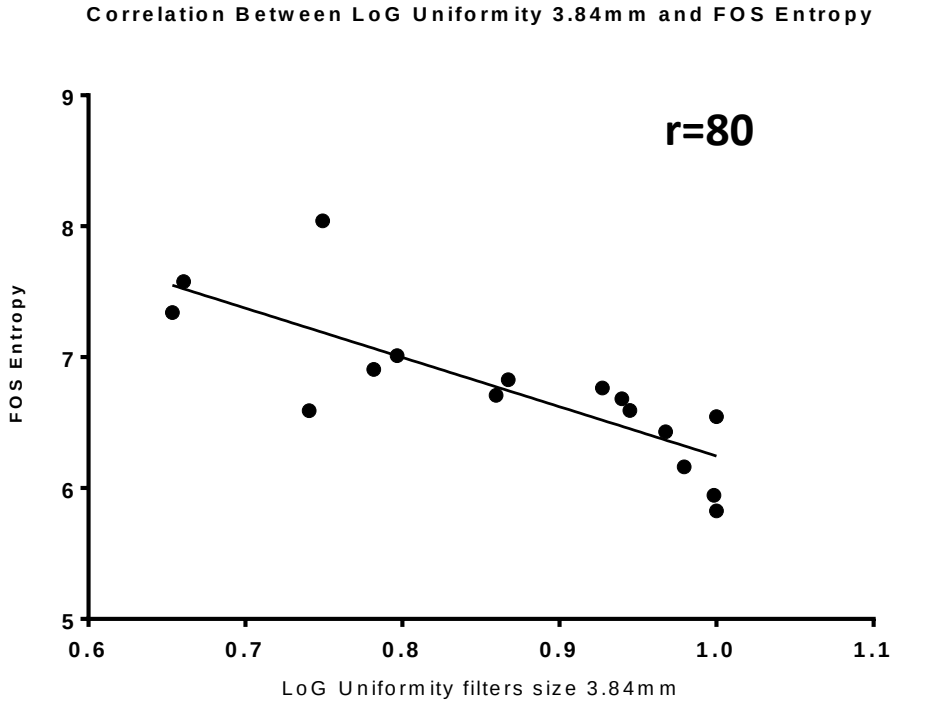

Fig 86: Correlation between LoG uniformity filter 3.84 mm and FOS entropy with negative correlation between them.

5.5 Discussion

There are many PET imaging studies conducted to evaluate the prognosis of pulmonary fibrosis over the years, most of which are preclinical studies using different PET tracers such as [^{18}F]-FDG [102]. Other PET tracers includes Cis-4-[^{18}F]-Fluoro-L-proline and ^{68}Ga [221]. All of these radiotracers are evaluated using SUV measurement to understand the uptake behaviours.

SUV measurements are semi quantitative methods commonly used in PET/CT studies for diagnosis of various diseases and monitoring tumour response to therapy [222]. There are many biological and physical factors affecting numerators of the SUV equation such as region of interest (ROI) size, definition of ROI, image resolution, reconstruction algorithm, and uptake period [223]. Different normalization factors (i.e., denominator factors) such as body weight (BW), body surface area, lean body mass (LBM), and blood glucose level have been used [224-227].

SUV normalised by body weight is the most widely used standardization method to measure [^{18}F]-FDG uptake. However, overestimation in overweight patients has been reported [228, 229]. In this study, SUV normalized by Body surface area (SUV_{BSA}) and SUV normalized by activity concentration (SUV_{AC}) have also been considered. These two normalization methods are independent of patients' body weight. In this retrospective study, the [^{18}F]-FDG uptake in fibrotic lung in all the IPF patients is higher than the background uptake in the normal lung tissues and lower than the reference standards (liver and MBP) in all the 3 normalizations technique [230] (Fig 36-41). SUV_{Max} and SUV_{Mean} (BW) normalization has been used previously to demonstrate the same pattern [219]. The Fibrotic ROIs were drawn at the region of honeycombing on HRCT which also revealed increase FDG uptake. Honeycombing appearance on HRCT were believed to represent irreversible fibrosis, however Increase [^{18}F]-FDG uptake around those areas suggest those areas may have metabolically active fibrotic process [231, 232]. Fibroblast

foci has been implicated as the hallmark in the pathogenesis of IPF [233, 234] and are recognized to express glucose transporter-1 [180].

The areas of radiologically normal lung in IPF have also demonstrated higher mean SUV_{Max} than background lung uptake when IPF patients were compared with group of control patients in all the 3 normalisations methods (SUV_{BW}, SUV_{BSA} and SUV_{AC}) (Fig 45-47). Similar results was found when mean SUV_{Mean} in IPF and lung cancer control group were compared in all the 3 normalization. These results have suggested that spill over effect of high [^{18}F]-FDG uptake within the lung tumour region does not influence the results in IPF patients. The high uptake in the normal lung in IPF patients is likely to be due to underlying pathology within the small airways and lung parenchyma. Higher SUV Max and Mean normalized with body weight in areas of normal lung parenchyma in IPF patients have been previously reported in the literature [130]. Hyper metabolic activity within apparent normal lung parenchyma may suggest the lung parenchyma is globally affected by IPF [235]. The cell type accounting for the metabolic signal on [^{18}F]-FDG PET also remains unclear. The presence of diffusely raised pulmonary [^{18}F]-FDG uptake, even in areas of normal parenchyma on HRCT, renders hypotheses suggesting that the PET signal in IPF patients is predominantly caused by colonization of polymorph infiltration secondary to infection in dilated airways less likely [119, 236]. Moreover, the fact that fibroblasts are generally sparse in normal lung may suggest that this cell type is not responsible for the PET signal.

The consistency of the results between the 3 normalisation (SUV_{BW}, SUV_{BSA} and SUV_{AC}) is strongly suggestive of a background pathology within the small airways and lung parenchyma. Moreover, the HRCT data of both groups (IPF and control) shows no significant differences in HU_{max} and HU_{mean} between the two groups. The lung tissue in both groups appeared to be normal, this may suggest that PET have higher sensitivity in early detection of pulmonary fibrosis than HRCT. Detection of high [^{18}F]-FDG

signal in IPF may have implication in understanding the pathogenesis, early diagnosis and treatment monitoring of the disease.

Identification of abnormal PET signal in IPF, undetectable on HRCT, could give an insight into the pathogenesis of the disease and may permit earlier detection of changes in disease activity [237]. In the absence of histology, it is difficult to speculate on the cellular origin for the raised pulmonary [18F]-FDG uptake in the areas of normal lung in IPF. It has been suggested increase pulmonary [18F]-FDG uptake is associated with increased leucocyte and fibroblast metabolism before structural changes become apparent on HRCT [150, 173]. Moreover, erythrocytes have also been proposed as potential source of increase [^{18}F]-FDG uptake [238]. [^{18}F]-FDG uptake could be used as a biomarker in IPF as it is considered a biomarker in inflammation. Two small animal studies using [^{18}F]-FDG PET (without CT) in IPF have been conducted [235, 239]. In one of the studies, increased pulmonary [^{18}F]-FDG was seen in 6 of 7 patients. In one of the patients, changes in [^{18}F]-FDG uptake correlated with a change in clinical status, supporting the use of PET as a monitor of disease activity [239]. In the other study [235], IPF [^{18}F]-FDG uptake was compared with other forms of interstitial lung disease, but no difference was found. This is consistent with hypotheses that suggest that although the initial stimulus for the fibrotic process may vary (e.g., epithelial injury or autoimmunity), there is a final common pathway [129, 140, 240]. Sensitive methods of disease monitoring in IPF patients are urgently required, as a lack of early measurable endpoints is hampering drug development.

[^{18}F]-FDG uptake measured by SUV (BW) and heterogeneity on textural analysis were both greater in areas of normal lung in IPF patients compared with controls, this result is consistent both in SUV mean and Max. This biological heterogeneity suggests that textural features derived from [^{18}F]-FDG PET may have prognostic use: this approach is increasingly applied in oncology as tumour heterogeneity is correlated with response to therapy as well as heterogeneity at the microscopic level [220, 241, 242]. This is the first

report of textural analysis of [^{18}F]-FDG PET in IPF patients and we identify 4 textural features that differ significantly compared to controls. Although, there are positive and negative correlations between some of the textural features, however, there are possibilities that some of the features are measuring the same thing within the ROI. The role of measuring [^{18}F]-FDG uptake and textural feature analysis to predict progressive fibrosis and lung function decline warrants further evaluation in a prospective cohort. Different [^{18}F]-FDG quantification methods such as; SUV_{BW}, SUV_{BSA}, SUV_{AC} and well as textural feature analysis have been used in this study and the same results have been recorded. These findings demonstrated that [^{18}F]-FDG has the potential of becoming a biomarker of disease progression and treatment response monitoring in IPF as it is commonly used in oncology and inflammatory diseases[243-245]. There is need for further studies to identify and standardize the useful textural features in IPF.

5.6 Limitation

20 IPF patients was recruited to further explore this theory prospectively. 2 PET-CT dual imaging was to be conducted six months apart to monitor changes in FDG uptake and textural features within the normal lung. Unfortunately due to time limit, technical issues with the PET scanner only few first images was carried out before the end of this research period.

5.7 Conclusion

Although, SUVs normalised by body weight is the main stay quantification method to measure [^{18}F]-FDG uptake within the PET imaging. In these studies, I demonstrated the potentials of textural features analysis in determining heterogeneity within the lung PET images in IPF patients. [^{18}F]-FDG PET-CT textural features are different between IPF patients and controls in areas of otherwise normal appearing lung. Further research is warranted to explore the relationship between [^{18}F]-FDG uptake, textural features and disease course to assess the role of PET-CT in prognostication and assessing treatment response in IPF patients.

Chapter 6 General Conclusion

The importance of PET imaging in cancer studies has been fully established, it is used for staging and treatment response monitoring of many cancers. However, the potentials of this imaging modality in non-malignant diseases has not been fully exploited. In this study, I explored its potentials in pulmonary drug depositions and imaging of Idiopathic Pulmonary Fibrosis.

Delivery of a therapeutic agent by inhalation has seen increasing applications for many respiratory diseases, including asthma, COPD, allergies, and influenza. Aerosol delivery has advantages: it delivers medication directly to where it is needed and it avoids the first-pass effect with minimum reduction of bioavailability. Following inhalation therapy, only a fraction of the dose reaches the expected target area, knowledge of the amount of drug actually deposited is essential in designing the delivery system or devices to optimize the delivery efficiency to the targeted region of the respiratory tract. This knowledge is also essential in developing a dosing regimen to deliver the required amount of active compound to the patient. It is also important in comparing the efficiency of delivery among different inhalational delivery devices.

Drugs that are administered by inhalation represent by far the most prolific area of drug bio distribution studies for drug development. Although the drug application is essentially topical, the tissues of the nasal turbinates, oral cavity and lungs are internal and inaccessible for direct measurements of drug distribution or local effect. Furthermore, the immediate local effect, if measurable, is not necessarily proportional to the deposition of drug. Thus, imaging is the only effective method for observation of deposition and absorption *in vivo.*

Molecular imaging technologies have a vital role to play in the drug development process. Over the past decade, molecular imaging has gained increasing acceptance by the academic and industry communities regarding drug discovery and development. It has been useful in the acquisition of a

deeper knowledge of biology regarding a variety of diseases, allowing the design of better candidate drugs in the identification and validation of new therapeutic targets, in the selection of candidate drugs that must move forward to the clinic or those where research should be stopped and in the establishment of dose range and regimens. Imaging has brought modern drug development to a superior level, not only by providing a deeper understanding of normal physiology, molecular mechanisms of disease and drug effects but also by allowing significant savings (in terms of time and resources). Molecular imaging in particular has driven not only the development of safer and innovative drugs but also strengthens the concept of personalized medicine.

Gamma scintigraphy, comprising two dimensional 'planar' imaging, is used widely to visualize and to quantify drug delivery, particularly by the oral and pulmonary routes. However, three-dimensional imaging modalities SPECT and PET also have applications within this area. SPECT and PET offer potential advantages over gamma scintigraphy in the assessment of regional lung deposition of orally inhaled therapeutic agents.

Planar imaging has by far the most literature in the drug distribution field. However, it has many disadvantages such as poor image quality and lack of information from regional deposition. Planar imaging has only one real advantage to consider when choosing a study method: it is simple.

Both planar and SPECT cameras uses the same radiopharmaceuticals, the radiopharmaceuticals are designed by either direct or Indirect labelling by adding an approved ^{99m}Tc compound to an aerosol medication and demonstrating that the radioactivity associated with the ^{99m}Tc distributes proportionally to the active drug content. So there is no change in the radiochemistry, a SPECT study can be done essentially as easily or even more easily than a planar study, since it gives data that can be better corrected for attenuation and scatter and provides a valuable improvement in the data obtained, both qualitatively and quantitatively. Aside from providing 3D data

with improved quantification, the issues surrounding a SPECT and a planar study are the same because they use the same radiotracers.

The 3D nature of PET, like SPECT, allows the drug measurement to be made in 3D regions of interest of any size and shape within the body. Corrections for quantification are based on the simultaneous detection of the two photons that result from positron decay and are built into the PET technique. PET cameras provide the most reliable quantification in molecular imaging.

Because of the historical dominance of planar imaging the question of choice of imaging method is generally framed in terms of comparison to that technique. The strengths and weaknesses of each method are mentioned clearly in the text. SPECT scanning is the same as planar in most respects, since any proposed study can adopt the same tracer, protocol, scan strategy, and analytical methods for either technique. The major difference, of course, is that SPECT provides 3D data, and attenuation and scatter corrections are easier and more accurate.

PET uses different radioisotopes, which emit a positively charged electron (position). Positrons travel a short distance in the body before interacting with an electron, causing annihilation and emission of 2 high-energy gamma rays in exactly opposite directions. In making a comparison with SPECT and planar imaging, the major advantage of PET is the ability to label and observe the active ingredient and to acquire kinetic data, very short half-lives radiotracers and scanning times can be very short (comparable to or shorter than those in planar imaging, and much shorter than those in SPECT imaging). Recent advancement in hybrid PET-CT imaging systems has made it easier to visualize lung anatomy alongside molecular information from the PET.

In pulmonary drug deposition study, two experiments were conducted concurrently, one experiment was performed using a nebulizer attached to a lung surrogate phantom to study the deposition pattern of the orally inhaled [^{18}F]-FDG along the phantom. Series of experimental procedures were conducted in order to understand different inputs such as; nebulizer out and

change in radioactivity concentration, without which the interpretation of the final results will be impossible. Establishing the linearity of the nebuliser output by aerosolising 0.9% saline repeatedly over time has made it possible to ascertain the volume nebulised at each time point. It was expected that the during nebulisation process the amount of [^{18}F]-FDG nebulised might not be similar to that of the saline, as such; determining the change in activity ([^{18}F]-FDG in the nebuliser after the nebulisation procedure was necessary. These factors (volume and change in activity concentration) were very vital in calculating the amount of [^{18}F]-FDG nebulised. The choice of one-minute nebulisation time was made in order to keep the radiation exposure as low as reasonably achievable (ALARA). The final stage of the experiment was designing a lung surrogate phantom, which was sectioned as pulmonary as well as the extra-pulmonary sections using a sponge that has similar density (similar Hounsfield unit) as the human lung. Similarity of the sponge density to human lung was very necessary to avoid quantification variability.

Although the lung surrogate phantom experiment did not measure the regional distribution of the [^{18}F]-FDG, it has however, provided the quantification of the [^{18}F]-FDG along what was considered as oral cavity, trachea and central zone of the lung. The phantom was limited in providing the quantification on the regional distribution due to structural limitation of the design. The phantom was not aimed to replicate the entire structure of the lung including the generations of the bronchial tree, however, it was meant to provide an understanding of the radiation safety of conducting aerosolised [^{18}F]-FDG procedures; identify the suitable duration of the procedure as well as the radiation dose required in conducting the procedure. Quantification of the various sections of the phantom as well as the various measurements conducted during the experiments have provided the answers to the questions. The experiment was a proof of concept and it has multiple implications in pulmonary drug development. The phantom could be used in testing the efficiency of new nebulizers in delivery inhalational drugs to the lung and it could also be used to compare the efficiency of different nebulisers. This will

add more information to the data obtained using *in vitro* and *ex vitro* procedures. Moreover, the imaging data in this experiment provided both quantitative as well as qualitative information which is closer to the *in vivo* human procedures.

The phantom experiment has demonstrated feasibility of using PET imaging to understand deposition pattern of aerosol drugs along respiratory pathway. Aerosolizing 0.9% saline to establish the linearity of the nebuliser output was first conducted, this help to understand the volume loss from the nebuliser per unit time. After several experiments at different time-points. The decision to choose 1-minute nebulisation of [^{18}F]-FDG to limit the radiation exposure to the operator was made. 1-minute nebulisation of [^{18}F]-FDG into the phantom not only produced a quantifiable image it also proved the radiation safety of this procedure. In this experiment, the amount of [^{18}F]-FDG dispensed into the nebuliser before the start of the experiment was between 800-1200MBq, an average of 81MBq nebulised after one-minute nebulisation with a total of around 10MBq deposited into the phantom. Motion artefact and the size of the patient may influence the results in human clinical trials, as such; increasing the initial radioactivity in the nebuliser will compensate for that. This however, will increase the radiation exposure to the patient. Based on our calculations, increasing the initial radioactivity in the nebuliser before the start of the experiment to 2.5GBq in 2 mls of 0.9% saline will expected to nebulise around 227MBq in one-minute however, only around 14MBq will be expected into the patient. Increasing the amount of radioactivity to the amount state will not pose any significant risk to the patient as the amount projected (14MBq) is far less than the average intravenous adult dose of 230MBq.

The other experiment involved the use of inhaler attached to ACI. Cascade impactors are used to validate the radiolabelling of the inhalational drug delivery devices. They operate on the principle of inertial impaction. Each stage of the impactor comprises a series of nozzles or jets through which the

sample laden air is drawn, directing any airborne particles towards the surface of the collection plate for that particular stage. ACI is arguably the most commonly used impactor within the pharmaceutical industry for the testing of inhaled products. The conventional ACI is an 8-stage cascade impactor suitable for measuring the aerodynamic particle size distribution (APSD) of both metered dose inhalers (MDIs) and DPIs. In this experiment, Abbreviated Cascade impactor with 3-stages was used. It has been reported to be more efficient and accurate than the longer version (8-stages).

The first stage of the inhaler experiment was mixing the content of the inhaler canister with the radiotracer. Radiolabelling of inhaler formulations for imaging studies is an indirect method of determining lung deposition and regional distribution of drug in human subjects. Hence, ensuring that the radiotracer and drug exhibit similar aerodynamic characteristics when aerosolised, and that addition of the radiotracer has not significantly altered the characteristics of the formulation, are critical steps in the development of a radiolabelling method.

The validation process involves characterization of the aerodynamic particle size distribution (APSD) of drug in the reference formulation, and of both drug and radiotracer in the radiolabelled formulation. ACI is considered to be quicker and more accurate in quantifying the deposition pattern due to its ability to illuminate many human and technical errors in the procedure.

HPLC method of isolating the retention time of the BDP and FFA compounds from the inhaler was developed and the method was used to compare the retention time and the concentration of the drugs compound from the inhaler and the stock solution of BDP and FFA from reference formulation. No significant difference in the HPLC retention time was observed between the 2 samples. After ACI analysis, sample from each stage of the impactor was collected for HPLC analysis to measure the concentration of the drug compounds along the stages of the ACI. Sample from each stage of the ACI

from the radiolabelled inhaler was assessed for radiation content using gamma counter.

The HPLC analysis of the drugs content of the radiolabelled inhaler and the [^{18}F]-FDG content from each stage has been placed side-by-side to understand the similarity of the distribution pattern along the stage of the ACI. Although, the radiolabelling in this experiment was just a mixture of the drugs and [^{18}F]-FDG in the inhaler canister and does not involved a chemical bonding, the [^{18}F]-FDG was assumed to be homogenously distributed within liquid droplets when generated by actuation of the inhaler. The comparison has revealed much closer distribution between the drugs and the [^{18}F]-FDG at each stage of the ACI. The [^{18}F]-FDG has travelled at the same rate as the drug compounds. The next stage of this experiment is to perform the inhalation procedure using anaesthetized animal instead of ACI, followed by PET imaging to ascertain the distribution pattern using image analysis.

This experiment has paved the way to more Positron-emitting radiotracers labelled with inhalational drug agents. Further development of this experiment will involve radiolabelling a suitable compound with positron-emitting radionuclides such as ^{18}F, ^{64}Cu, ^{68}Ga, or ^{89}Zr. standard radiolabelling will provide more accurate distribution of the radiotracers and the drug agents along the respiratory tract. Positron-emitting radionuclides of elements such as Carbon (C), Nitrogen (N) and Oxygen (O_2) can replace the stable analogues in drugs and biomolecules, and hence it is possible to synthesize PET probes with the same chemical structure as the parent unlabelled molecules without altering their biological activity.

PET image-guided drug delivery has important role in realizing the full potential of the next generation of inhalational drug agents. For this purpose, it is essential to choose radioisotopes of appropriate half-lives to match the pharmacokinetics of the drug carriers used. Moreover, lung can also be used as a portal for the delivery of drugs to the systemic circulation and to achieve this, the alveolar zone usually needs to be targeted to gain maximum cross-

over to the circulation. Quantification of the total and regional lung deposition is important to the understanding of the therapeutic response for both topical and systemic targeting of an inhaled drug. Further development of these 2 experiments is necessary which for time constrained could not be done during this research period. The nebuliser experiments will focus on effective quantification of the regional deposition in healthy human volunteers. Whereas, the inhaler experiment will proceed by conducting preclinical animal inhalational experiments to corroborate the ACI findings.

IPF has been considered the deadliest form of IIPs, the prognosis is variable; patients with IPF have progressive dyspnoea and a median survival of 36 months. Currently, the diagnosis is based on a combination of clinical, physiologic, radiologic, and, if necessary, histopathologic criteria. Despite advances in medical therapy and technology, the prognosis in IPF remains poor, and the need for progress and new approaches is acute. The lack of progress reflects the poorly understood aetiology and pathogenesis of IPF. Some patients may experience a more precipitous course, with periods of relative stability followed by acute deteriorations in respiratory status. Many of these acute deteriorations are of unknown aetiology and have been termed acute exacerbations of IPF.

High-resolution CT (HRCT) is the current imaging reference standard in the investigation of patients with IPF, revealing structural detail of the entire lung parenchyma that corresponds to pathologic specimens. However, HRCT is a purely structural imaging technique on which the metabolic activity within the lung cannot ascertained. PET offers the ability to noninvasively investigate cellular metabolism *in vivo*. Recent technologic advances have led to the integration of PET with CT, allowing molecular imaging to be combined with the fine structural detail of CT. PET has profoundly affected the management of cancer; however, the role of PET in IPF had been poorly explored.

PET imaging has the potential in adding more information to the more conventional CT imaging in IPF. In adding to a typical UIP pattern seen on the CT, PET imaging added more information regarding the subtle features not clearly identified by CT. In the literature, IPF patients have been shown to demonstrates high [^{18}F]-FDG uptake in fibrotic lung tissues as defined by HRCT. The aim of the retrospective study undertaken in this research was to review the [^{18}F]-FDG uptake at sites of normal-appearing lung on HRCT in IPF. Semi-quantitative measurement using SUV normalized by body weight, body surface area and activity concentration as well as the textural features within the VOIs around the normal lung parenchyma was considered for analysis.

Among the 3 group of patients considered in this study namely lung cancer, extra-pulmonary cancers and IPF, only IPF demonstrated high [^{18}F]-FDG uptake within normal lung parenchyma. The results from SUV measurements have been consistent with the textural features analysis both results indicate high [^{18}F]-FDG update in the areas of normal lung in IPF patients. To further analyse the correlation between the measurements, CT number (Hounsfield unit) among the 3 group of patients were found to be within the range of normal aerated lung. These results suggest that the changes within the lung tissues are microscopic making them undetectable by CT. This may indicate the high sensitivity of PET imaging in detecting microscopic changes because of changes in metabolism within the apparently normal lung in IPF patients. The high uptake of [^{18}F]-FDG in the areas of apparently normal lung may represent areas of 'micro fibrosis' which in the future may develop radiological features of fibrosis. Understanding the cells responsible for the high [^{18}F]-FDG uptake in the areas of normal lung will be valuable in finding effective treatment for the disease. A prospective study has been designed to perform dual PET imaging (1 hour and 3 hours) after the injection of [^{18}F]-FDG with a repeat imaging after 6 months to further understand the implication of the increase [^{18}F]-FDG within the normal lung tissues in IPF patients. This may have implication in prognosis of the disease, early

detection of exacerbated IPF and treatment response monitoring. At the time of compiling this thesis 6 patients have already undertaken their first dual imaging.

PET imaging has the potentials in pulmonary drug development and IPF, however, there is a clear need to standardise methodology such that multi-centred PET imaging data can be compared. Moreover, to my knowledge, this is the first experiment exploring the potential usage of the textural parameters in IPF. Textural parameters of lung tissue heterogeneity in [^{18}F]-FDG PET/CT may have implication for therapy response assessment and prognosis in Patients with IPF. More research are need to better understand the suitable textural parameters.

Chapter 7 Future Work

The findings in the phantom experiment needs to be validated by a human clinical trial, where a healthy volunteer will inhale similar amount of [^{18}F]-FDG using the same experimental protocols as the phantom experiment. In addition to quantification of deposition pattern within the human lung, information about internal dose and clearance of [^{18}F]-FDG from the system will be provided.

Pre-clinical Animal study to compare the deposition pattern within the stages of ACI with the *in vivo* deposition within the mice is needed. In the future, this experiment will be translated into human clinical trial.

Imaging pulmonary drug deposition will play a vital role in personalised medicine in inhaler technique (i.e which nebulizer for which patient?) and targeting airway deposition (e.g. large airways in asthma smaller in IPF)

More prospective studies with substantial number of patients are required to establish the role of PET imaging in IPF. Moreover, understanding the cells responsible for increase [^{18}F]-FDG uptake within the normal lung tissues will play a pivotal role in IPF drug development (e.g. choosing which expensive drug to give in IPF active/inactive disease as well as monitoring therapy)

Textural feature analysis has demonstrated the potentials in the management of IPF. However, these is need for establishing standard textural features to be used in IPF.

PET imaging has the potentials in pulmonary drug development and IPF, however, there is a clear need to standardise methodology so that data from PET imaging can be compared between centres.

Chapter 8 References

1. Fiamma, M.N., et al., *Effects of hypercapnia and hypocapnia on ventilatory variability and the chaotic dynamics of ventilatory flow in humans.* Am J Physiol Regul Integr Comp Physiol, 2007. **292**(5): p. R1985-93.
2. Feldman, J.L. and C.A. Del Negro, *Looking for inspiration: new perspectives on respiratory rhythm.* Nature reviews. Neuroscience, 2006. **7**(3): p. 232-242.
3. Smith, J.C., et al., *Pre-Botzinger complex: a brainstem region that may generate respiratory rhythm in mammals.* Science, 1991. **254**(5032): p. 726-9.
4. Caubit, X., et al., *Teashirt 3 Regulates Development of Neurons Involved in Both Respiratory Rhythm and Airflow Control.* The Journal of neuroscience : the official journal of the Society for Neuroscience, 2010. **30**: p. 9465-76.
5. Que, C.L., et al., *Homeokinesis and short-term variability of human airway caliber.* J Appl Physiol (1985), 2001. **91**(3): p. 1131-41.
6. D'Angelo, E., et al., *Pulmonary and chest wall mechanics in anesthetized paralyzed humans.* Journal of Applied Physiology, 1991. **70**(6): p. 2602-2610.
7. Mangin, L., et al., *Source of human ventilatory chaos: lessons from switching controlled mechanical ventilation to inspiratory pressure support in critically ill patients.* Respir Physiol Neurobiol, 2008. **161**(2): p. 189-96.
8. Kleinstreuer, C. and Z. Zhang, *Airflow and Particle Transport in the Human Respiratory System.* Annual Review of Fluid Mechanics, 2010. **42**(1): p. 301-334.
9. O'Donnell, K.P. and H.D.C. Smyth, *Macro- and Microstructure of the Airways for Drug Delivery*, in *Controlled Pulmonary Drug Delivery*, H.D.C. Smyth and A.J. Hickey, Editors. 2011, Springer New York: New York, NY. p. 1-19.

10. Bates, J.H.T., *Lung Mechanics: An Inverse Modeling Approach*. 2009, Cambridge: Cambridge University Press.
11. Oca, M.M.d., J. Rassulo, and B.R. Celli, *Respiratory muscle and cardiopulmonary function during exercise in very severe COPD.* American Journal of Respiratory and Critical Care Medicine, 1996. **154**(5): p. 1284-1289.
12. Pump, K.K., *The Morphology of the Finer Branches of the Bronchial Tree of the Human Lung.* CHEST, 1964. **46**(4): p. 379-398.
13. Itoh, H., M. Nishino, and H. Hatabu, *Architecture of the lung: morphology and function.* Journal of thoracic imaging, 2004. **19**(4): p. 221-227.
14. Petersson, J. and R.W. Glenny, *Gas exchange and ventilation–perfusion relationships in the lung.* European Respiratory Journal, 2014. **44**(4): p. 1023-1041.
15. Schreider, J.P. and O.G. Raabe, *Structure of the human respiratory acinus.* American Journal of Anatomy, 1981. **162**(3): p. 221-232.
16. Tawhai, M.H. and P.J. Hunter, *Characterising respiratory airway gas mixing using a lumped parameter model of the pulmonary acinus.* Respiration Physiology, 2001. **127**(2): p. 241-248.
17. Pelosi, P., et al., *Total Respiratory System, Lung, and Chest Wall Mechanics in Sedated-Paralyzed Postoperative Morbidly Obese Patients.* Chest, 1996. **109**(1): p. 144-151.
18. Sheel, A.W. and L.M. Romer, *Ventilation and respiratory mechanics.* Compr Physiol, 2012. **2**(2): p. 1093-142.
19. Weibel, E.R., et al., *Morphometric model for pulmonary diffusing capacity. I. Membrane diffusing capacity.* Respir Physiol, 1993. **93**(2): p. 125-49.
20. Gehr, P., M. Bachofen, and E.R. Weibel, *The normal human lung: ultrastructure and morphometric estimation of diffusion capacity.* Respiration Physiology, 1978. **32**(2): p. 121-140.

21. Wielpütz, M.O., et al., *Radiological diagnosis in lung disease: factoring treatment options into the choice of diagnostic modality.* Deutsches Arzteblatt international, 2014. **111**(11): p. 181-187.
22. De Wever, W., J. Coolen, and J.A. Verschakelen, *Imaging techniques in lung cancer.* Breathe, 2011. **7**(4): p. 338-346.
23. Merritt, C.R., et al., *Digital imaging of the chest.* Journal of thoracic imaging, 1985. **1**(1): p. 1-13.
24. Ball, L., et al., *Lung imaging: how to get better look inside the lung.* Annals of translational medicine, 2017. **5**(14): p. 294-294.
25. Ley, S., *Lung imaging.* European Respiratory Review, 2015. **24**(136): p. 240-245.
26. Lynch, D.A., et al., *High-Resolution Computed Tomography in Idiopathic Pulmonary Fibrosis.* American Journal of Respiratory and Critical Care Medicine, 2005. **172**(4): p. 488-493.
27. Wielpütz, M.O., et al., *Radiological Diagnosis in Lung Disease: Factoring Treatment Options Into the Choice of Diagnostic Modality.* Deutsches Ärzteblatt International, 2014. **111**(11): p. 181-187.
28. Lynch, D.A., et al., *High-Resolution Computed Tomography in Idiopathic Pulmonary Fibrosis.* American Journal of Respiratory and Critical Care Medicine, 2005. **172**(4): p. 488-493.
29. Oda, K., et al., *High-resolution CT scoring system-based grading scale predicts the clinical outcomes in patients with idiopathic pulmonary fibrosis.* Respiratory research, 2014. **15**: p. 10.
30. ERS, *ERS Handbook of respiratory medicine [electronic resource]*, ed. P. Palange and A.K. Simonds. 2013, Sheffield: European Respiratory Society.
31. Isitman, A.T., et al., *Comparison of technetium-99m pyrophosphate and technetium-99m DTPA aerosols for SPECT ventilation lung imaging.* J Nucl Med, 1988. **29**(11): p. 1761-7.
32. Cabahug, C.J., et al., *Utility of technetium-99m-DTPA in determining regional ventilation.* J Nucl Med, 1996. **37**(2): p. 239-44.

33. Newman, S.P. and I.R. Wilding, *Imaging techniques for assessing drug delivery in man.* Pharm Sci Technolo Today, 1999. **2**(5): p. 181-189.
34. Zhenghong, L. and M.S. Berridge, *PET imaging-based evaluation of aerosol drugs and their delivery devices: nasal and pulmonary studies.* Medical Imaging, IEEE Transactions on, 2002. **21**(10): p. 1324-1331.
35. Cunha, L., et al., *The role of molecular imaging in modern drug development.* Drug Discovery Today, 2014. **19**(7): p. 936-948.
36. Laube, B.L., et al., *Editorial: Standards for lung imaging techniques.* J Aerosol Med Pulm Drug Deliv, 2012. **25 Suppl 1**: p. S1-2.
37. Bar-Shalom, R., A.Y. Valdivia, and M.D. Blaufox, *PET imaging in oncology.* Semin Nucl Med, 2000. **30**(3): p. 150-85.
38. Kastelik, J.A., et al., *A widely available method for the assessment of aerosol delivery in cystic fibrosis.* Pulm Pharmacol Ther, 2002. **15**(6): p. 513-9.
39. Berridge, M.S., D.L. Heald, and Z. Lee, *Imaging studies of biodistribution and kinetics in drug development.* Drug Development Research, 2003. **59**(2): p. 208-226.
40. Dolovich, M.B., *Measuring total and regional lung deposition using inhaled radiotracers.* J Aerosol Med, 2001. **14 Suppl 1**: p. S35-44.
41. Bateman, T.M., *Advantages and disadvantages of PET and SPECT in a busy clinical practice.* J Nucl Cardiol, 2012. **19 Suppl 1**: p. S3-11.
42. Bateman, T.M., et al., *Diagnostic accuracy of rest/stress ECG-gated Rb-82 myocardial perfusion PET: comparison with ECG-gated Tc-99m sestamibi SPECT.* J Nucl Cardiol, 2006. **13**(1): p. 24-33.
43. Chris Baker, C.F., *Design, execution and testing of a phantom to allow optimisation of simultaneous dual isotope Krypton V/Q SPECT imaging*. 2016, Harefield Hospital

Royal Brompton & Harefield NHS Foundation Trust.

44. Lippmann, M., D. Yeates, and R. Albert, *Deposition, retention, and clearance of inhaled particles.* Occupational and Environmental Medicine, 1980. **37**(4): p. 337-362.
45. Shelly, M., G. Lloyd, and G. Park, *A review of the mechanisms and methods of humidification of inspired gases.* Intensive care medicine, 1988. **14**(1): p. 1-9.
46. Thompson, D.C. and R.J. Altiere, *Physiology and Pharmacology of the Airways*, in *Inhalation Aerosols*. 2006, CRC Press. p. 109-152.
47. Tamer, M.A., J.H. Modell, and C.N. Rieffel, *Hyponatremia secondary to ultrasonic aerosol therapy in the newborn infant.* The Journal of pediatrics, 1970. **77**(6): p. 1051-1054.
48. Patton, J.S. and P.R. Byron, *Inhaling medicines: delivering drugs to the body through the lungs.* Nature reviews Drug discovery, 2007. **6**(1): p. 67.
49. Patton, J.S., *Mechanisms of macromolecule absorption by the lungs.* Advanced drug delivery reviews, 1996. **19**(1): p. 3-36.
50. Massaro, G.D. and D. Massaro, *Formation of pulmonary alveoli and gas-exchange surface area: quantitation and regulation.* Annual review of physiology, 1996. **58**(1): p. 73-92.
51. Schulz, H., *Mechanisms and factors affecting intrapulmonary particle deposition: implications for efficient inhalation therapies Holger Schulz.* Pharmaceutical Science & Technology Today, 1998. **1**(8): p. 326-344.
52. Shekunov, B.Y., et al., *Particle Size Analysis in Pharmaceutics: Principles, Methods and Applications.* Pharmaceutical Research, 2007. **24**(2): p. 203-227.
53. Mitchell, J. and M. Nagel, *Particle Size Analysis of Aerosols from Medicinal Inhalers.* KONA Powder and Particle Journal, 2004. **22**: p. 32-65.
54. Katz, I., et al., *Controlled, Parametric, Individualized, 2D, and 3D Imaging Measurements of Aerosol Deposition in the Respiratory*

Tract of Healthy Human Subjects: Preliminary Comparisons with Simulations. Aerosol Science and Technology, 2013. **47**(7): p. 714-723.

55. Corcoran, T.E., S.G. Devadason, and P.J. Kuehl, *Introduction: Aerosol delivery of orally inhaled agents.* J Aerosol Med Pulm Drug Deliv, 2012. **25 Suppl 1**: p. S3-5.
56. Sakagami, M., *In vivo, in vitro and ex vivo models to assess pulmonary absorption and disposition of inhaled therapeutics for systemic delivery.* Adv Drug Deliv Rev, 2006. **58**(9-10): p. 1030-60.
57. Marple, V.A. and B.Y.H. Liu, *Characteristics of laminar jet impactors.* Environmental Science & Technology, 1974. **8**(7): p. 648-654.
58. Newton, G.J., O.G. Raabe, and B.V. Mokler, *Cascade impactor design and performance.* Journal of Aerosol Science, 1977. **8**(5): p. 339-347.
59. Son, Y.-J., J.P. Mitchell, and J.T. McConville, *In Vitro Performance Testing for Pulmonary Drug Delivery*, in *Controlled Pulmonary Drug Delivery*, H.D.C. Smyth and A.J. Hickey, Editors. 2011, Springer New York: New York, NY. p. 383-415.
60. Roberts, D., *Theory of Multi-Nozzle Impactor Stages and the Interpretation of Stage Mensuration Data*. Vol. 43. 2009. 1119-1129.
61. Sethuraman, V.V. and A.J. Hickey, *Evaluation of preseparator performance for the 8-stage nonviable andersen impactor.* AAPS PharmSciTech, 2001. **2**(1): p. E4.
62. Bonam, M., et al., *Minimizing variability of cascade impaction measurements in inhalers and nebulizers.* AAPS PharmSciTech, 2008. **9**(2): p. 404-13.
63. Christopher, D., et al., *Considerations for the development and practice of cascade impaction testing, including a mass balance failure investigation tree.* J Aerosol Med, 2003. **16**(3): p. 235-47.

64. Tougas, T.P., et al., *Improved Quality Control Metrics for Cascade Impaction Measurements of Orally Inhaled Drug Products (OIPs).* AAPS PharmSciTech, 2009. **10**(4): p. 1276.

65. Marple, V.A., et al., *Next generation pharmaceutical impactor (a new impactor for pharmaceutical inhaler testing). Part II: Archival calibration.* Journal of Aerosol medicine, 2003. **16**(3): p. 301-324.

66. Hoe, S., et al., *Measuring charge and mass distributions in dry powder inhalers using the electrical Next Generation Impactor (eNGI).* European Journal of Pharmaceutical Sciences, 2009. **38**(2): p. 88-94.

67. Hallworth, G. and D. Westmoreland, *The twin impinger: a simple device for assessing the delivery of drugs from metered dose pressurized aerosol inhalers.* Journal of pharmacy and pharmacology, 1987. **39**(12): p. 966-972.

68. Robison, T.W., R.J. Dorio, and K.J. Kim, *Formation of tight monolayers of guinea pig airway epithelial cells cultured in an air-interface: bioelectric properties.* BioTechniques, 1993. **15**(3): p. 468-473.

69. de Jong, P.M., et al., *Serial culturing of human bronchial epithelial cells derived from biopsies.* In Vitro Cell Dev Biol Anim, 1993. **29a**(5): p. 379-87.

70. Oreffo, V.I., A. Morgan, and R.J. Richards, *Isolation of Clara cells from the mouse lung.* Environmental health perspectives, 1990. **85**: p. 51-64.

71. Buckley, S.T., K.-J. Kim, and C. Ehrhardt, *In Vitro Cell Culture Models for Evaluating Controlled Release Pulmonary Drug Delivery*, in *Controlled Pulmonary Drug Delivery*, H.D.C. Smyth and A.J. Hickey, Editors. 2011, Springer New York: New York, NY. p. 417-442.

72. HSU, M.C.-P. and J.P.F. BAI, *Investigation into the Presence of Insulin-degrading Enzyme in Cultured Type II Alveolar Cells and the*

Effects of Enzyme Inhibitors on Pulmonary Bioavailability of Insulin in Rats. Journal of Pharmacy and Pharmacology, 1998. **50**(5): p. 507-514.

73. Garcia Contreras, L., et al., *Pharmacokinetics of Inhaled Rifampicin Porous Particles for Tuberculosis Treatment: Insight into Rifampicin Absorption from the Lungs of Guinea Pigs.* Mol Pharm, 2015. **12**(8): p. 2642-50.
74. Sakagami, M., *Insulin disposition in the lung following oral inhalation in humans : a meta-analysis of its pharmacokinetics.* Clinical pharmacokinetics, 2004. **43**(8): p. 539-552.
75. Linder, J., et al., *Bronchoalveolar lavage in the cytologic diagnosis of carcinoma of the lung.* Acta Cytol, 1987. **31**(6): p. 796-801.
76. Dorato, M.A., *Overview of inhalation toxicology.* Environmental health perspectives, 1990. **85**: p. 163-170.
77. Raeburn D, U.S., Villamil ME *Techniques for drug delivery to the airways,*

and the assessment of lung function in animal models. J Pharmacol Toxicol Meth, 1992. **27:**: p. 143–159.

78. Garcia-Contreras, L., *In Vivo Animal Models for Controlled-Release Pulmonary Drug Delivery*, in *Controlled Pulmonary Drug Delivery*, H.D.C. Smyth and A.J. Hickey, Editors. 2011, Springer New York: New York, NY. p. 443-474.
79. Garcia-Contreras, L., et al., *Evaluation of dosing regimen of respirable rifampicin biodegradable microspheres in the treatment of tuberculosis in the guinea pig.* J Antimicrob Chemother, 2006. **58**(5): p. 980-6.
80. Labiris, N.R., et al., *Uptake of 18fluorodeoxyglucose in the cystic fibrosis lung: a measure of lung inflammation?* European Respiratory Journal, 2003. **21**(5): p. 848-854.

81. Eberl, S., H.-K. Chan, and E. Daviskas, *SPECT Imaging for Radioaerosol Deposition and Clearance Studies.* Journal of Aerosol Medicine, 2006. **19**(1): p. 8-20.
82. Henderson, A.J., *Bronchoalveolar lavage.* Archives of disease in childhood, 1994. **70**(3): p. 167-169.
83. Conway, J., *Lung imaging — Two dimensional gamma scintigraphy, SPECT, CT and PET.* Advanced Drug Delivery Reviews, 2012. **64**(4): p. 357-368.
84. Van Beers, B.E., et al., *Imaging Biomarker Measurements*, in *Imaging Biomarkers: Development and Clinical Integration*, L. Martí-Bonmatí and A. Alberich-Bayarri, Editors. 2017, Springer International Publishing: Cham. p. 87-99.
85. Alberich-Bayarri, A., *Imaging Biomarker Structural Analysis*, in *Imaging Biomarkers: Development and Clinical Integration*, L. Martí-Bonmatí and A. Alberich-Bayarri, Editors. 2017, Springer International Publishing: Cham. p. 65-69.
86. Manikis, G.C., N. Papanikolaou, and C. Matos, *Validating the Imaging Biomarker: The Proof of Efficacy and Effectiveness*, in *Imaging Biomarkers: Development and Clinical Integration*, L. Martí-Bonmatí and A. Alberich-Bayarri, Editors. 2017, Springer International Publishing: Cham. p. 115-122.
87. O'Connor, J.P.B., et al., *Imaging biomarker roadmap for cancer studies.* Nature Reviews Clinical Oncology, 2016. **14**: p. 169.
88. Trattnig, S., *The Shift in Paradigm to Precision Medicine in Imaging: International Initiatives for the Promotion of Imaging Biomarkers*, in *Imaging Biomarkers: Development and Clinical Integration*, L. Martí-Bonmatí and A. Alberich-Bayarri, Editors. 2017, Springer International Publishing: Cham. p. 1-7.
89. Willmann, J.K., et al., *Molecular imaging in drug development.* Nature Reviews Drug Discovery, 2008. **7**: p. 591.

90. Martí-Bonmatí, L., *Introduction to the Stepwise Development of Imaging Biomarkers*, in *Imaging Biomarkers: Development and Clinical Integration*, L. Martí-Bonmatí and A. Alberich-Bayarri, Editors. 2017, Springer International Publishing: Cham. p. 9-27.
91. Deshpande, D.S., et al., *Gamma scintigraphic evaluation of a miniaturized AERx pulmonary delivery system for aerosol delivery to anesthetized animals using a positive pressure ventilation system.* J Aerosol Med, 2005. **18**(1): p. 34-44.
92. Biddiscombe, M.F., et al., *Comparing lung regions of interest in gamma scintigraphy for assessing inhaled therapeutic aerosol deposition.* J Aerosol Med Pulm Drug Deliv, 2011. **24**(3): p. 165-73.
93. Newman, S., et al., *Standardization of techniques for using planar (2D) imaging for aerosol deposition assessment of orally inhaled products.* J Aerosol Med Pulm Drug Deliv, 2012. **25 Suppl 1**: p. S10-28.
94. Devadason, S.G., et al., *Validation of radiolabeling of drug formulations for aerosol deposition assessment of orally inhaled products.* J Aerosol Med Pulm Drug Deliv, 2012. **25 Suppl 1**: p. S6-9.
95. Verbanck, S., et al., *Inhaled Aerosol Distribution in Human Airways: A Scintigraphy-Guided Study in a 3D Printed Model.* J Aerosol Med Pulm Drug Deliv, 2016. **29**(6): p. 525-533.
96. Pitcairn, G.R., et al., *Pulmonary drug delivery from the Taifun dry powder inhaler is relatively independent of the patient's inspiratory effort.* J Aerosol Med, 2000. **13**(2): p. 97-104.
97. Pitcairn, G.R. and S.P. Newman, *Tissue Attenuation Corrections in Gamma Scintigraphy.* Journal of Aerosol Medicine, 1997. **10**(3): p. 187-198.
98. Newman, S.P., *Scintigraphic assessment of therapeutic aerosols.* Crit Rev Ther Drug Carrier Syst, 1993. **10**(1): p. 65-109.

99. Nana, A., et al., *Beta 2-agonists administered by a dry powder inhaler can be used in acute asthma.* Respir Med, 1998. **92**(2): p. 167-72.
100. Newman, S.P., et al., *Radionuclide imaging technologies and their use in evaluating asthma drug deposition in the lungs.* Advanced Drug Delivery Reviews, 2003. **55**(7): p. 851-867.
101. Bailey, D.L., et al., *Development of a cost-effective modular SPECT/CT scanner.* Eur J Nucl Med Mol Imaging, 2007. **34**(9): p. 1415-26.
102. Dolovich, M. and R. Labiris, *Imaging Drug Delivery and Drug Responses in the Lung.* Proceedings of the American Thoracic Society, 2004. **1**(4): p. 329-337.
103. Fleming, J., et al., *Standardization of techniques for using single-photon emission computed tomography (SPECT) for aerosol deposition assessment of orally inhaled products.* J Aerosol Med Pulm Drug Deliv, 2012. **25 Suppl 1**: p. S29-51.
104. Fleming, J.S., et al., *Comparison of SPECT Aerosol Deposition Data with Twenty-Four-Hour Clearance Measurements.* Journal of Aerosol Medicine, 2006. **19**(3): p. 261-267.
105. Fleming, J., et al., *The Use of Combined Single Photon Emission Computed Tomography and X-ray Computed Tomography to Assess the Fate of Inhaled Aerosol.* Journal of Aerosol Medicine and Pulmonary Drug Delivery, 2010. **24**(1): p. 49-60.
106. Fleming, J.S., et al., *A comparison of planar scintigraphy and SPECT measurement of total lung deposition of inhaled aerosol.* J Aerosol Med, 2003. **16**(1): p. 9-19.
107. Fleming, J.S., et al., *Comparison of SPECT aerosol deposition data with a human respiratory tract model.* J Aerosol Med, 2006. **19**(3): p. 268-78.
108. Dolovich Aerosol Research Laboratory, M.U., St. Joseph's Healthcare, Hamilton, ON, Canada, *Positron Emission Tomography*

(PET) for Assessing Aerosol Deposition of Orally Inhaled Drugs. 2012: Canada. p. Lead Shield.

109. Kotzerke, J., M. Andreeff, and G. Wunderlich, *PET aerosol lung scintigraphy using Galligas.* European Journal of Nuclear Medicine and Molecular Imaging, 2010. **37**(1): p. 175-177.
110. Dolovich, M.B. and D.L. Bailey, *Positron emission tomography (PET) for assessing aerosol deposition of orally inhaled drug products.* J Aerosol Med Pulm Drug Deliv, 2012. **25 Suppl 1**: p. S52-71.
111. Dolovich, M.B. and D.P. Schuster, *Positron Emission Tomography and Computed Tomography versus Positron Emission Tomography–Computed Tomography.* Proceedings of the American Thoracic Society, 2007. **4**(4): p. 328-333.
112. Yanai, M., et al., *Deposition and clearance of inhaled 18FDG powder in patients with chronic obstructive pulmonary disease.* Eur Respir J, 1998. **11**(6): p. 1342-8.
113. Fleming, J., et al., *The use of combined single photon emission computed tomography and X-ray computed tomography to assess the fate of inhaled aerosol.* J Aerosol Med Pulm Drug Deliv, 2011. **24**(1): p. 49-60.
114. Yamada, A., et al., *Evaluation of 2-deoxy-2-[18F]fluoro-D-glucose positron emission tomography in gastric carcinoma: relation to histological subtypes, depth of tumor invasion, and glucose transporter-1 expression.* Annals of Nuclear Medicine, 2006. **20**(9): p. 597-604.
115. Deng, D., et al., *Crystal structure of the human glucose transporter GLUT1*. Nature, 2014. **510**: p. 121.
116. Dolovich, M.B., *18F-Fluorodeoxyglucose Positron Emission Tomographic Imaging of Pulmonary Functions, Pathology, and Drug Delivery.* Proceedings of the American Thoracic Society, 2009. **6**(5): p. 477-485.

117. *ERS Handbook of respiratory medicine [electronic resource]*, ed. P. Palange and A.K. Simonds. 2013, Sheffield: European Respiratory Society.
118. Akgün, K.M., K. Crothers, and M. Pisani, *Epidemiology and Management of Common Pulmonary Diseases in Older Persons.* The Journals of Gerontology Series A: Biological Sciences and Medical Sciences, 2012. **67A**(3): p. 276-291.
119. Antoniades, N., et al., *Platelet-derived growth factor in idiopathic pulmonary fibrosis.* J Clin Invest, 1990. **86**: p. 1055 - 1064.
120. Collard, H.R., et al., *Acute Exacerbations of Idiopathic Pulmonary Fibrosis.* American Journal of Respiratory and Critical Care Medicine, 2007. **176**(7): p. 636-643.
121. Abe, S. and A. Gemma, *Definition of IPF*, in *Idiopathic Pulmonary Fibrosis: Advances in Diagnostic Tools and Disease Management*, H. Nakamura and K. Aoshiba, Editors. 2016, Springer Japan: Tokyo. p. 3-9.
122. ATS/ERS, *American Thoracic Society/European Respiratory Society International Multidisciplinary Consensus Classification of the Idiopathic Interstitial Pneumonias.* American Journal of Respiratory and Critical Care Medicine, 2002. **165**(2): p. 277-304.
123. Khalil, N. and R. O'Connor, *Idiopathic pulmonary fibrosis: current understanding of the pathogenesis and the status of treatment.* Canadian Medical Association Journal, 2004. **171**(2): p. 153-60.
124. Selman, M. and A. Pardo, *Idiopathic pulmonary fibrosis: an epithelial/fibroblastic cross-talk disorder.* Respiratory Research, 2002. **3**(1): p. 3.
125. ATS/ERS, *Idiopathic Pulmonary Fibrosis: Diagnosis and Treatment.* American Journal of Respiratory and Critical Care Medicine, 2000. **161**(2): p. 646-664.

126. Crystal, R.G., et al., *Future Research Directions in Idiopathic Pulmonary Fibrosis.* American Journal of Respiratory and Critical Care Medicine, 2002. **166**(2): p. 236-246.
127. Enomoto, N., et al., *Quantitative analysis of lung elastic fibers in idiopathic pleuroparenchymal fibroelastosis (IPPFE): Comparison of clinical, radiological, and pathological findings with those of idiopathic pulmonary fibrosis (IPF).* BMC Pulmonary Medicine, 2014. **14**(1).
128. Nicholson, A.G., *Classification of idiopathic interstitial pneumonias: making sense of the alphabet soup.* Histopathology, 2002. **41**(5): p. 381-391.
129. Gross, T.J. and G.W. Hunninghake, *Idiopathic pulmonary fibrosis.* N Engl J Med, 2001. **345**(7): p. 517-25.
130. Win, T., et al., *Areas of normal pulmonary parenchyma on HRCT exhibit increased FDG PET signal in IPF patients.* European Journal of Nuclear Medicine and Molecular Imaging, 2014. **41**(2): p. 337-342.
131. Mikolasch, T.A., H.S. Garthwaite, and J.C. Porter, *Update in diagnosis and management of interstitial lung disease.* Clinical Medicine, 2016. **16**(Suppl 6): p. s71-s78.
132. Sharma, R., R. Guleria, and J. Pande, *Idiopathic pulmonary fibrosis: newer concepts and management strategies.* INDIAN JOURNAL OF CHEST DISEASES AND ALLIED SCIENCES, 2003. **45**(1): p. 31-50.
133. Hodgson, U., *Idiopathic pulmonary fibrosis-From epidemiology to gene mapping.* 2006.
134. Raghu, G., et al., *An Official ATS/ERS/JRS/ALAT Statement: Idiopathic Pulmonary Fibrosis: Evidence-based Guidelines for Diagnosis and Management.* American Journal of Respiratory and Critical Care Medicine, 2011. **183**(6): p. 788-824.
135. Harari, S., et al., *Epidemiology of Idiopathic Pulmonary Fibrosis in Northern Italy.* PloS one, 2016. **11**(2): p. e0147072-e0147072.

136. Borchers, A.T., et al., *Idiopathic pulmonary fibrosis-an epidemiological and pathological review*. Clin Rev Allergy Immunol, 2011. **40**(2): p. 117-34.
137. Nalysnyk, L., et al., *Incidence and prevalence of idiopathic pulmonary fibrosis: review of the literature.* Eur Respir Rev, 2012. **21**(126): p. 355-61.
138. Kuwano, K., J. Araya, and H. Hara, *Epidemiology and Risk Factors of IPF*, in *Idiopathic Pulmonary Fibrosis: Advances in Diagnostic Tools and Disease Management*, H. Nakamura and K. Aoshiba, Editors. 2016, Springer Japan: Tokyo. p. 11-25.
139. Barbas-Filho, J., et al., *Evidence of type II pneumocyte apoptosis in the pathogenesis of idiopathic pulmonary fibrosis (IFP)/usual interstitial pneumonia (UIP).* J Clin Pathol, 2001. **54**: p. 132 - 138.
140. Selman, M., T.E. King, and A. Pardo, *Idiopathic pulmonary fibrosis: prevaling and evolving hypotheses about its pathogenesis and implications for therapy.* Ann Intern Med, 2001. **134**.
141. Wang, Y., et al., *Genetic defects in surfactant protein A2 are associated with pulmonary fibrosis and lung cancer.* American journal of human genetics, 2009. **84**(1): p. 52-59.
142. Nogee, L.M., et al., *A mutation in the surfactant protein C gene associated with familial interstitial lung disease.* N Engl J Med, 2001. **344**(8): p. 573-9.
143. Adamson, I., L. Young, and D. Bowden, *Relationship of alveolar epithelial injury and repair to the induction of pulmonary fibrosis.* Am J Pathol, 1988. **130**: p. 377 - 383.
144. Ishii, Y., *Acute Exacerbation of IPF*, in *Idiopathic Pulmonary Fibrosis: Advances in Diagnostic Tools and Disease Management*, H. Nakamura and K. Aoshiba, Editors. 2016, Springer Japan: Tokyo. p. 27-42.
145. Chodon, T., et al., *Keloid-derived fibroblasts are refractory to Fas-mediated apoptosis and neutralization of autocrine transforming*

growth factor-beta 1 can abrogate this resistance. Am J Pathol, 2000. **157**: p. 1661 - 1669.

146. Khalil, N., et al., *TGF-beta1, but not TGF-beta2 or TGF-beta3, is differentially present in epithelial cells of advanced pulmonary fibrosis: an immunohistochemical study.* Am J Respir Cell Mol Biol, 1996. **14**: p. 131 - 138.
147. Thannickal, V.J., et al., *Myofibroblast differentiation by TGF-β1 is dependent on cell adhesion and integrin signaling via focal adhesion kinase.* Journal of Biological Chemistry, 2003.
148. Zhang, L., et al., *Ectopic pancreas in the anterior mediastinum: A report of two cases and review of the literature.* Oncology Letters, 2014. **7**(4): p. 1053-1056.
149. Serini, G., et al., *The fibronectin domain ED-A is crucial for myofibroblastic phenotype induction by transforming growth factor-beta1*. J Cell Biol, 1998. **142**(3): p. 873-81.
150. Amara, N., et al., *NOX4/NADPH oxidase expression is increased in pulmonary fibroblasts from patients with idiopathic pulmonary fibrosis and mediates TGF-β1-induced fibroblast differentiation into myofibroblasts.* Thorax, 2010. **65**(8): p. 733-738.
151. Cantin, A.M., et al., *Oxidant-mediated epithelial cell injury in idiopathic pulmonary fibrosis.* J Clin Invest, 1987. **79**(6): p. 1665-73.
152. Kinnula, V.L., et al., *Oxidative Stress in Pulmonary Fibrosis.* American Journal of Respiratory and Critical Care Medicine, 2005. **172**(4): p. 417-422.
153. Chiba, H. and H. Takahashi, *Specific Serum Markers of IPF*, in *Idiopathic Pulmonary Fibrosis: Advances in Diagnostic Tools and Disease Management*, H. Nakamura and K. Aoshiba, Editors. 2016, Springer Japan: Tokyo. p. 61-76.
154. Greene, K.E., et al., *Serum surfactant proteins-A and -D as biomarkers in idiopathic pulmonary fibrosis.* Eur Respir J, 2002. **19**(3): p. 439-46.

155. Drakopanagiotakis, F., et al., *Biomarkers in idiopathic pulmonary fibrosis.* Matrix Biol, 2018. **68-69**: p. 404-421.
156. Seibold, M.A., et al., *The Idiopathic Pulmonary Fibrosis Honeycomb Cyst Contains A Mucocilary Pseudostratified Epithelium.* PLOS ONE, 2013. **8**(3): p. e58658.
157. Seibold, M.A., et al., *A Common MUC5B Promoter Polymorphism and Pulmonary Fibrosis.* New England Journal of Medicine, 2011. **364**(16): p. 1503-1512.
158. Noth, I., et al., *Genetic variants associated with idiopathic pulmonary fibrosis susceptibility and mortality: a genome-wide association study.* The Lancet Respiratory Medicine, 2013. **1**(4): p. 309-317.
159. Fingerlin, T.E., et al., *Genome-wide association study identifies multiple susceptibility loci for pulmonary fibrosis.* Nature Genetics, 2013. **45**: p. 613.
160. Cha, S.-I., et al., *Cleaved cytokeratin-18 is a mechanistically informative biomarker in idiopathic pulmonary fibrosis.* Respiratory Research, 2012. **13**(1): p. 105.
161. Armanios, M.Y., et al., *Telomerase Mutations in Families with Idiopathic Pulmonary Fibrosis.* New England Journal of Medicine, 2007. **356**(13): p. 1317-1326.
162. Tsakiri, K.D., et al., *Adult-onset pulmonary fibrosis caused by mutations in telomerase.* Proceedings of the National Academy of Sciences, 2007. **104**(18): p. 7552-7557.
163. Hewitt, R.J. and P.L. Molyneaux, *The respiratory microbiome in idiopathic pulmonary fibrosis.* Annals of Translational Medicine, 2017. **5**(12).
164. Bratic, A. and N.-G. Larsson, *The role of mitochondria in aging.* The Journal of Clinical Investigation, 2013. **123**(3): p. 951-957.
165. Kawabata, Y., *Pathology of IPF*, in *Idiopathic Pulmonary Fibrosis: Advances in Diagnostic Tools and Disease Management*, H.

Nakamura and K. Aoshiba, Editors. 2016, Springer Japan: Tokyo. p. 105-132.

166. Caravan, P., et al., *Molecular Magnetic Resonance Imaging of Pulmonary Fibrosis in Mice.* American Journal of Respiratory Cell and Molecular Biology, 2013. **49**(6): p. 1120-1126.

167. Ambrosini, V., et al., *68Ga-DOTANOC PET/CT Allows Somatostatin Receptor Imaging in Idiopathic Pulmonary Fibrosis: Preliminary Results.* Journal of Nuclear Medicine, 2010. **51**(12): p. 1950-1955.

168. Fell, C.D., et al., *Clinical Predictors of a Diagnosis of Idiopathic Pulmonary Fibrosis.* American Journal of Respiratory and Critical Care Medicine, 2010. **181**(8): p. 832-837.

169. Bartholmai, B.J., et al., *Quantitative CT Imaging of Interstitial Lung Diseases.* Journal of thoracic imaging, 2013. **28**(5): p. 10.1097/RTI.0b013e3182a21969.

170. Fischer, T., J. Reynolds, and S. Trotter, *The idiopathic interstitial pneumonias: a beginner's guide.* 2014.

171. Vos, T., et al., *Global, regional, and national incidence, prevalence, and years lived with disability for 301 acute and chronic diseases and injuries in 188 countries, 1990-2013: A systematic analysis for the Global Burden of Disease Study 2013.* The Lancet, 2015. **386**(9995): p. 743-800.

172. Sakai, F., *High-Resolution Computed Tomography of Honeycombing and IPF/UIP*, in *Idiopathic Pulmonary Fibrosis: Advances in Diagnostic Tools and Disease Management*, H. Nakamura and K. Aoshiba, Editors. 2016, Springer Japan: Tokyo. p. 77-104.

173. Bondue, B., et al., *PET/CT with 18F-FDG– and 18F-FBEM–Labeled Leukocytes for Metabolic Activity and Leukocyte Recruitment Monitoring in a Mouse Model of Pulmonary Fibrosis.* Journal of Nuclear Medicine, 2015. **56**(1): p. 127-132.

174. Win, T., et al., *Novel Positron Emission Tomography/Computed Tomography of Diffuse Parenchymal Lung Disease Combining a*

Labeled Somatostatin Receptor Analogue and 2-Deoxy-2 [18F] Fluoro-D-Glucose. Molecular Imaging, 2012. **11**(2): p. 7290.2011.00030.

175. Win, T., et al., *Pulmonary (18)F-FDG uptake helps refine current risk stratification in idiopathic pulmonary fibrosis (IPF).* Eur J Nucl Med Mol Imaging, 2018. **45**(5): p. 806-815.
176. Win, T., et al., *Areas of normal pulmonary parenchyma on HRCT exhibit increased FDG PET signal in IPF patients.* European Journal of Nuclear Medicine and Molecular Imaging, 2014. **41**(2): p. 337-342.
177. Umeda, Y., et al., *Dual-time-point 18F-FDG PET imaging for diagnosis of disease type and disease activity in patients with idiopathic interstitial pneumonia.* European Journal of Nuclear Medicine & Molecular Imaging, 2009. **36**(7): p. 1121-30.
178. Bjoraker, J., et al., *Prognostic significance of histopathologic subsets in idiopathic pulmonary fibrosis.* Am J Respir Crit Care Med, 1998. **157**: p. 199 - 203.
179. Martinez-Outschoorn, U.E., et al., *Cancer cells metabolically "fertilize" the tumor microenvironment with hydrogen peroxide, driving the Warburg effect: Implications for PET imaging of human tumors.* Cell Cycle, 2011. **10**(15): p. 2504-2520.
180. El-Chemaly, S., et al., *Glucose transporter-1 distribution in fibrotic lung disease: association with [8F]-2-fluoro-2-deoxyglucose-PET scan uptake, inflammation, and neovascularization.* Chest, 2013. **143**(6): p. 1685-91.
181. Varecza, Z., et al., *Expression of the Somatostatin Receptor Subtype 4 in Intact and Inflamed Pulmonary Tissues.* Journal of Histochemistry and Cytochemistry, 2009. **57**(12): p. 1127-1137.
182. Borie, R., et al., *Activation of somatostatin receptors attenuates pulmonary fibrosis.* Thorax, 2008. **63**(3): p. 251-258.
183. Smyth, H.D.C., *Controlled pulmonary drug delivery*, A.J. Hickey, Editor. 2011, Springer: New York :.

184. Newman, S.P., *IMAGING PULMONARY DRUG DELIVERY*, in *Drug Delivery Applications of Noninvasive Imaging*. 2013, John Wiley & Sons, Inc. p. 333-366.
185. Fleming, J.S., et al., *Three-dimensional description of pulmonary deposition of inhaled aerosol using data from multimodality imaging.* J Nucl Med, 1996. **37**(5): p. 873-7.
186. Barbara, S.K. and M.P. Patricia, *Positron Emission Tomography*, in *Radiotracers in Drug Development*. 2006, CRC Press. p. 251-267.
187. Baker CD, F.J., *Creating a lung phantom to allow simultaneous dual isotope V/Q SPECT imaging*. 2016, Harefield Hospital, Royal Brompton & Harefield NHS Foundation Trust.
188. Zarski, J.P., et al., *Comparison of nine blood tests and transient elastography for liver fibrosis in chronic hepatitis C: the ANRS HCEP-23 study.* J Hepatol, 2012. **56**(1): p. 55-62.
189. Fällmar, D., et al., *Validation of true low-dose (18)F-FDG PET of the brain.* American Journal of Nuclear Medicine and Molecular Imaging, 2016. **6**(5): p. 269-276.
190. Darquenne, C., *Aerosol Deposition in Health and Disease.* Journal of Aerosol Medicine and Pulmonary Drug Delivery, 2012. **25**(3): p. 140-147.
191. Cheng, Y.S., *Mechanisms of Pharmaceutical Aerosol Deposition in the Respiratory Tract.* AAPS PharmSciTech, 2014. **15**(3): p. 630-640.
192. Clark, L.D., et al., *Changes in Radiation Dose with Variations in Human Anatomy: Moderately and Severely Obese Adults.* J Nucl Med, 2010. **51**.
193. Mitchell, J., and Myrna B. Dolovich, *Clinically Relevant Test Methods to Establish In Vitro Equivalence for Spacers and Valved Holding Chambers Used with Pressurized Metered Dose Inhalers (PMDIs).* Journal of Aerosol Medicine and Pulmonary Drug Delivery, 2012. **25**(4): p. 217–242.

194. Conway, J., et al., *The Co-imaging of Gamma Camera Measurements of Aerosol Deposition and Respiratory Anatomy.* Journal of Aerosol Medicine and Pulmonary Drug Delivery, 2013. **26**(3): p. 123-130.
195. Ojima, F., et al., *Preparation of a fine powder of 2-deoxy-2-[18F]fluoro-D-glucose suitable for inhalation to diagnose lung diseases by means of PET.* Annals of Nuclear Medicine, 1989. **3**(3): p. 143-147.
196. Constantinou, M., et al., *Flixotide™-pressurized metered-dose inhalers loaded with [18F]fluticasone propionate particles for drug deposition studies in humans with PET–formulation and analysis.* Journal of Labelled Compounds and Radiopharmaceuticals, 2004. **47**(1): p. 55-70.
197. Ament, S.J., et al., *PET lung ventilation/perfusion imaging using (68)Ga aerosol (Galligas) and (68)Ga-labeled macroaggregated albumin.* Recent Results Cancer Res, 2013. **194**: p. 395-423.
198. Berridge, M.S., Z. Lee, and D.L. Heald, *Pulmonary Distribution and Kinetics of Inhaled [11C]Triamcinolone Acetonide.* Journal of Nuclear Medicine, 2000. **41**(10): p. 1603-1611.
199. Newman, S., et al., *Efficient drug delivery to the lungs from a continuously operated open-vent nebulizer and low pressure compressor system*. Vol. 7. 1994. 1177-81.
200. Brown, J.S., et al., *Thoracic and respirable particle definitions for human health risk assessment.* Part Fibre Toxicol, 2013. **10**: p. 12.
201. Mettler Jr, F.A., et al., *Effective doses in radiology and diagnostic nuclear medicine: a catalog.* Radiology, 2008. **248**(1): p. 254-263.
202. England, P.H., *Ionising radiation: dose comparisons*. 2011: London.
203. Rader, D.J. and V.A. Marple, *Effect of Ultra-Stokesian Drag and Particle Interception on Impaction Characteristics.* Aerosol Science and Technology, 1985. **4**(2): p. 141-156.

204. Rohdewald, P., H.W. Mollman, and G. Hochhaus, *Affinities of glucocorticoids for glucocorticoid receptors in the human lung.* Agents Actions, 1986. **17**(3-4): p. 290-1.

205. Wurthwein, G. and P. Rohdewald, *Activation of beclomethasone dipropionate by hydrolysis to beclomethasone-17-monopropionate.* Biopharm Drug Dispos, 1990. **11**(5): p. 381-94.

206. Parmar, V.K., H.N. Patel, and B.K. Patel, *Sensitive and robust methods for simultaneous determination of beclomethasone dipropionate and formoterol fumarate dihydrate in rotacaps.* Journal of Chromatographic Science, 2014. **52**(10): p. 1255-66.

207. Wurthwein, G., *Lipophilicity and receptor affinity of glucocorticoids.* Pharm Ztg Wiss, 1992. **4**: p. 161-167.

208. Pauwels , R.A., et al., *Effect of Inhaled Formoterol and Budesonide on Exacerbations of Asthma.* New England Journal of Medicine, 1997. **337**(20): p. 1405-1411.

209. Mitchell, J., et al., *Adapting the Abbreviated Impactor Measurement (AIM) Concept to Make Appropriate Inhaler Aerosol Measurements to Compare with Clinical Data: A Scoping Study with the "Alberta" Idealized Throat (AIT) Inlet.* Journal of Aerosol Medicine and Pulmonary Drug Delivery, 2012. **25**(4): p. 188-197.

210. Denyer, J. and T. Dyche, *The Adaptive Aerosol Delivery (AAD) Technology: Past, Present, and Future.* Journal of Aerosol Medicine and Pulmonary Drug Delivery, 2010. **23**(Suppl 1): p. S-1-S-10.

211. Dunbar, C. and J. Mitchell, *Analysis of Cascade Impactor Mass Distributions.* Journal of Aerosol Medicine, 2005. **18**(4): p. 439-451.

212. Mitchell, J.P. and M.W. Nagel, *Cascade Impactors for the Size Characterization of Aerosols from Medical Inhalers: Their Uses and Limitations.* Journal of Aerosol Medicine, 2003. **16**(4): p. 341-377.

213. Blum, F., *High performance liquid chromatography.* British Journal of Hospital Medicine (2005), 2014. **75**(Sup2): p. C18-C21.

214. Shellie, R.A., L.-L. Xie, and P.J. Marriott, *Retention time reproducibility in comprehensive two-dimensional gas chromatography using cryogenic modulation: An intralaboratory study.* Journal of Chromatography A, 2002. **968**(1): p. 161-170.
215. McBride, W.J., et al., *A novel method of 18F radiolabeling for PET.* J Nucl Med, 2009. **50**(6): p. 991-8.
216. Khalil, N. and R. O'Connor, *Idiopathic pulmonary fibrosis: current understanding of the pathogenesis and the status of treatment.* CMAJ Canadian Medical Association Journal, 2004. **171**(2): p. 153-160.
217. Garcia, C.K., *Idiopathic Pulmonary Fibrosis.* Proceedings of the American Thoracic Society, 2011. **8**(2): p. 158-162.
218. Olson, A.L.M.D.M., et al., *Seasonal Variation: Mortality From Pulmonary Fibrosis Is Greatest in the Winter.* Chest, 2009. **136**(1): p. 16-22.
219. Win, T., et al., *18F-Fluorodeoxyglucose positron emission tomography pulmonary imaging in idiopathic pulmonary fibrosis is reproducible: implications for future clinical trials.* European Journal of Nuclear Medicine and Molecular Imaging, 2012. **39**(3): p. 521-528.
220. Chicklore, S., et al., *Quantifying tumour heterogeneity in 18F-FDG PET/CT imaging by texture analysis.* Eur J Nucl Med Mol Imaging, 2013. **40**(1): p. 133-40.
221. Wallace, W.E., et al., *Cis-4-[(18)F]fluoro-L-proline PET imaging of pulmonary fibrosis in a rabbit model.* J Nucl Med, 2002. **43**(3): p. 413-20.
222. Park, S.H., et al., *The Feasibility of (18)F-Fluorothymidine PET for Prediction of Tumor Response after Induction Chemotherapy Followed by Chemoradiotherapy with S-1/Oxaliplatin in Patients with Resectable Esophageal Cancer.* Nuclear medicine and molecular imaging, 2012. **46**(1): p. 57-64.
223. Boellaard, R., *Standards for PET image acquisition and quantitative data analysis.* J Nucl Med, 2009. **50 Suppl 1**: p. 11s-20s.

224. Zasadny, K.R. and R.L. Wahl, *Standardized uptake values of normal tissues at PET with 2-[fluorine-18]-fluoro-2-deoxy-D-glucose: variations with body weight and a method for correction.* Radiology, 1993. **189**(3): p. 847-50.

225. Yeung, H.W., et al., *Standardized uptake value in pediatric patients: an investigation to determine the optimum measurement parameter.* Eur J Nucl Med Mol Imaging, 2002. **29**(1): p. 61-6.

226. Menda, Y., et al., *Evaluation of various corrections to the standardized uptake value for diagnosis of pulmonary malignancy.* Nucl Med Commun, 2001. **22**(10): p. 1077-81.

227. Kim, C.K., et al., *Standardized uptake values of FDG: body surface area correction is preferable to body weight correction.* J Nucl Med, 1994. **35**(1): p. 164-7.

228. Kim, C.K., et al., *Standardized uptake values of FDG: body surface area correction is preferable to body weight correction.* Journal of nuclear medicine, 1994. **35**(1): p. 164-167.

229. Chen, D.L., M.A. Mintun, and D.P. Schuster, *Comparison of Methods to Quantitate 18F-FDG Uptake with PET During Experimental Acute Lung Injury.* Journal of Nuclear Medicine, 2004. **45**(9): p. 1583-1590.

230. Vera, P., et al., *Does chemotherapy influence the quantification of SUV when contrast-enhanced CT is used in PET/CT in lymphoma?* Eur J Nucl Med Mol Imaging, 2007. **34**(12): p. 1943-52.

231. Gotway, M.B., M.M. Freemer, and T.E. King, Jr., *Challenges in pulmonary fibrosis. 1: Use of high resolution CT scanning of the lung for the evaluation of patients with idiopathic interstitial pneumonias.* Thorax, 2007. **62**(6): p. 546-53.

232. Flaherty, K.R., et al., *Clinical significance of histological classification of idiopathic interstitial pneumonia.* Eur Respir J, 2002. **19**(2): p. 275-83.

233. OJ, D., *Clinical review: idiopathic pulmonary fibrosis—past, present and future.* Respir Med, 2006. **100**: p. 1871–1885.

234. Zhang, K., et al., *Myofibroblasts and their role in lung collagen gene expression during pulmonary fibrosis. A combined immunohistochemical and in situ hybridization study.* The American Journal of Pathology, 1994. **145**(1): p. 114-125.

235. Nusair, S., et al., *Positron emission tomography in interstitial lung disease.* Respirology, 2007. **12**(6): p. 843-847.

236. Wallace, W.E., et al., *Cis-4-[18F]Fluoro-l-Proline PET Imaging of Pulmonary Fibrosis in a Rabbit Model.* Journal of Nuclear Medicine, 2002. **43**(3): p. 413-420.

237. Groves, A.M., et al., *Idiopathic pulmonary fibrosis and diffuse parenchymal lung disease: implications from initial experience with 18F-FDG PET/CT.* Journal of Nuclear Medicine, 2009. **50**(4): p. 538-45.

238. Matsusaka, Y., et al., *(18)F-FDG-labeled red blood cell PET for blood-pool imaging: preclinical evaluation in rats.* EJNMMI Research, 2017. **7**: p. 19.

239. Meissner, H.-H.a., et al., *Idiopathic Pulmonary Fibrosis: Evaluation with Positron Emission Tomography.* Respiration, 2006. **73**(2): p. 197-202.

240. Maher, T.M., A.U. Wells, and G.J. Laurent, *Idiopathic pulmonary fibrosis: multiple causes and multiple mechanisms?* Eur Respir J, 2007. **30**(5): p. 835-9.

241. Davnall, F., et al., *Assessment of tumor heterogeneity: an emerging imaging tool for clinical practice?* Insights Imaging, 2012. **3**(6): p. 573-89.

242. Orlhac, F., et al., *Multiscale Texture Analysis: From 18F-FDG PET Images to Histologic Images.* J Nucl Med, 2016. **57**(11): p. 1823-1828.

243. Larson, S.M. and L.H. Schwartz, *18F-FDG PET as a Candidate for "Qualified Biomarker": Functional Assessment of Treatment Response in Oncology.* Journal of Nuclear Medicine, 2006. **47**(6): p. 901-903.

244. Mankoff, D.A., D.A. Pryma, and A.S. Clark, *Molecular Imaging Biomarkers for Oncology Clinical Trials.* Journal of Nuclear Medicine, 2014. **55**(4): p. 525-528.

245. Harris, R.S., et al., *18F-FDG Uptake Rate Is a Biomarker of Eosinophilic Inflammation and Airway Response in Asthma.* Journal of Nuclear Medicine, 2011. **52**(11): p. 1713-1720.

Chapter 9 Appendices: List of Abstracts and Peer review papers

9.1 Appendix 1: Textural analysis demonstrates heterogeneous [18F]-FDG uptake in radiologically normal lung in patients with idiopathic pulmonary fibrosis.

***ERJ Express*. Published on September 27, 2018 as doi:10.1183/13993003.01138-2018**

EUROPEAN RESPIRATORY *journal*

FLAGSHIP SCIENTIFIC JOURNAL OF ERS

Early View

Research letter

Textural analysis demonstrates heterogeneous [^{18}F]-FDG uptake in radiologically normal lung in patients with idiopathic pulmonary fibrosis

Shamsuddeen A. Aliyu, Ged Avery, Christopher Cawthorne, Stephen J. Archibald, Timor Kadir, Julien M. Y. Willaime, Alyn H. Morice, Simon P. Hart, Michael G. Crooks

Please cite this article as: Aliyu SA, Avery G, Cawthorne C, *et al*. Textural analysis demonstrates heterogeneous [^{18}F]-FDG uptake in radiologically normal lung in patients with idiopathic pulmonary fibrosis. *Eur Respir J* 2018; in press (https://doi.org/10.1183/13993003.01138-2018).

Textural analysis demonstrates heterogeneous [^{18}F]-FDG uptake in radiologically normal lung in patients with idiopathic pulmonary fibrosis

Shamsuddeen A. Aliyu [1,2] Ged Avery [3] Christopher Cawthorne [2]

Stephen J. Archibald [2] Timor Kadir [4] Julien M. Y. Willaime [5] Alyn H. Morice [1] *Simon P. Hart [1] Michael G. Crooks [1]

1. Respiratory Research Group, Hull York Medical School, Castle Hill Hospital, Cottingham, HU16 5JQ
2. PET Research Centre, University of Hull, Cottingham Road, Hull, HU6 7RX
3. Hull and East Yorkshire Hospitals NHS Trust, Castle Hill Hospital, Cottingham, East Yorkshire, HU16 5JQ
4. Optellum Ltd, Oxford Centre for Innovation, Oxford, OX1 1BY
5. Mirada Medical Ltd, Oxford Centre for Innovation, New Road, Oxford, UK

*corresponding author: s.hart@hull.ac.uk

250 character statement for @ERSpublications

Textural analysis demonstrates increased heterogeneity of [18F]-FDG uptake in normal lung (on CT) in patients with IPF. Molecular imaging of the lungs using PET can be used to study early disease in IPF before CT abnormalities are apparent.

ABSTRACT

Positron Emission Tomography (PET) scanning in idiopathic pulmonary fibrosis (IPF) has revealed increased [^{18}F]-fluorodeoxyglucose ([^{18}F]-FDG) uptake in areas of the lungs that appear normal on high resolution computed tomography (HRCT). We hypothesised that 'microscopic' disease identified using PET would be heterogeneous because IPF is characterised histologically by patchy fibrosis. We applied textural analysis to PET scans to evaluate heterogeneity of [^{18}F]-FDG uptake in lung regions that appeared normal on HRCT. We identified six textural features that demonstrated significantly more heterogeneous [^{18}F]-FDG uptake in radiologically normal lung in IPF patients compared with controls. Textural analysis of lung PET-

CT imaging is a novel approach to study early changes in IPF before HRCT abnormalities are apparent.

INTRODUCTION

Recently, Positron Emission Tomography-Computerised Tomography (PET-CT) imaging in IPF has revealed increased [^{18}F]-fluorodeoxyglucose ([^{18}F]-FDG) uptake both in fibrotic lung and areas of lung with normal radiological appearance on HRCT [1 2]. IPF is characterised by heterogeneous fibrosis at the tissue level, so to gain insight into the early 'microscopic' disease process we used established textural features [3 4] to evaluate heterogeneity of [^{18}F]-FDG uptake in radiologically normal lung in patients with IPF.

METHODS

Patients with IPF diagnosed according to international guidelines and who had undergone PET-CT imaging for concomitant cancer diagnosis or staging were identified retrospectively in a single interstitial lung disease (ILD) tertiary referral centre. Controls comprised patients without ILD who had undergone PET-CT imaging for lung cancer (control group 1) or extra-thoracic malignancy (control group 2).

PET-CT images were analysed by two experienced radiologists. Four 10mm diameter regions of interest (ROIs) were placed manually in areas of lung with normal CT appearance, confirmed by measuring lung density. ROIs were placed away from areas of high FDG uptake (concomitant tumour, mediastinum, diaphragm) to avoid spill-over. [^{18}F]-FDG uptake (standardized uptake values (SUV)) and textural features were extracted within each ROI using XD™ (Mirada Medical Ltd, UK) and proprietary software [5]. Mean and maximum SUV were normalised using body weight. Twenty textural features were extracted from each ROI, including First Order Statistics (FOS) derived from the grey-level intensity distribution, a measure of grey-level uniformity derived from the Laplacian of Gaussian (LoG) technique for a range of filter sizes (mm), and Laws Texture features using two dimensional convolution masks [3-5]. Paired t-tests were used to compare fibrotic and normal lung in IPF patients. Unpaired t-tests were used to compare normal lung in IPF and controls, using a Bonferronicorrected alpha of .0025 (.05/20). Results are expressed as mean (SD).

RESULTS

Forty-nine PET-CT scans were identified from 16 patients with IPF (13 men, 3 women; mean (SD) age 74.1 (10.2); percent predicted FVC 87 (12); percent predicted TLco 46 (14)), 17 lung cancer controls (10 men, 7 women; age 61.3 (16.4)), and 16 extra-thoracic malignancy controls (9 men, 7 women; age 64.5 (12.4)). Lung cancer was the most common reason for PET-CT imaging in IPF patients (11/16). Most extra-thoracic malignancy controls had lymphoma or melanoma (11/16).

Areas of radiologically established fibrosis in IPF patients exhibited higher SUV compared to radiologically normal lung in the same patient (maximum SUV 2.1 (0.5) vs 1.0 (0.3), p<.001; mean SUV 1.3 (0.4) vs 0.8 (0.3), p<.001).

Radiologically normal lung on CT was confirmed by measuring lung density, showing identical Hounsfield units in IPF and controls (data not shown). There were no differences between the two control groups in maximum or minimum SUV in radiologically normal lung. On PET imaging, the SUV in radiologically normal lung in IPF patients was significantly higher than normal lung in pooled controls (maximum SUV 1.0 (0.3) vs 0.7 (0.2) respectively, p=.002; mean SUV 0.8 (0.3) vs 0.6 (0.2), p=.001).

We found significant differences in heterogeneity of the PET [^{18}F]-FDG signal in normal lung between IPF patients and controls in six textural features (Figure 1): LoG Uniformity with a 3.84mm filter (0.77 (0.12) vs 0.92 (0.10) respectively, p<.0001); LoG Uniformity with a 6.19mm filter (0.87 (0.12), 0.98 (0.05), p<.0001);

Laws Tex L5E5 mean (5.9 (2.8) x10^4, 2.8 (1.4) x10^4, p<.0001); LawsTex L5L5 standard deviation (std) (2.3 (1.5) x10^6, 1.1 (0.6) x10^6, p<.001); Laws Tex L5E5 std (2.1 (1.2) x10^4, 1.0 (0.52) x10^4, p<.0001); FOS std (310 (199), 139 (77), p<.0001). These textural features indicate higher variability in signal intensities within the ROIs in radiologically normal lung in IPF.

DISCUSSION

IPF is a patchy disease at the tissue level, with areas of new and established fibrosis interspersed with histologically normal lung. As IPF progresses over time, fibrosis spreads to involve previously unaffected lung. Increased [^{18}F]-

FDG uptake in radiologically normal lung in patients with IPF [2] has been proposed to reflect increased metabolism in inflammatory cells, erythrocytes, or fibroblasts in early injury or fibrosis before structural lung changes become apparent on HRCT [6 7 8]. Our finding of heterogeneous [^{18}F]-FDG uptake demonstrated by textural analysis in radiologically normal lung in IPF patients supports use of PET imaging to non-invasively identify early 'microscopic' disease. We cannot say whether the heterogeneous [^{18}F]-FDG signal represents early injury, inflammation, fibrosis, or other processes which would require histological correlation. Redistribution of pulmonary blood flow to normal lung is an unlikely explanation for our findings because there was no increase in CT density, the IPF patients did not have severe disease, and we would not expect blood flow to generate a heterogeneous PET signal. A limitation of the present study was the relatively small (10mm) ROIs which were necessary to avoid spill-over effect and to target only lung that was normal on CT. Our results require confirmation in other populations with early pulmonary fibrosis, including patients with rheumatological disease or subjects in CT screening studies with 'interstitial lung abnormalities'. Textural features derived from [^{18}F]-FDG PET are increasingly applied in oncology, and tumour heterogeneity is associated with response to therapy [4]. Textural analysis of lung PET-CT imaging is a novel approach that could be used to study early events in IPF pathogenesis, identify early disease, aid prognostication, or predict response to therapy.

References

1. Win T, Lambrou T, Hutton B, et al. 18F-Fluorodeoxyglucose positron emission tomography pulmonary imaging in idiopathic pulmonary fibrosis is reproducible: implications for future clinical trials. European journal of nuclear medicine and molecular imaging 2012;**39**(3):52128.
2. Win T, Thomas B, Lambrou T, et al. Areas of normal pulmonary parenchyma on HRCT exhibit increased FDG PET signal in IPF patients. European journal of nuclear medicine and molecular imaging 2014;**41**(2):337-42.

3. Chicklore S, Goh V, Siddique M, et al. Quantifying tumour heterogeneity in 18F-FDG PET/CT imaging by texture analysis. European journal of nuclear medicine and molecular imaging 2013;**40**(1):133-40.
4. Hatt M, Tixier F, Pierce L, et al. Characterization of PET/CT images using texture analysis: the past, the present… any future? European journal of nuclear medicine and molecular imaging 2017;**44**(1):151-65.
5. Willaime JMY PL, Boukerroui D et al. Impact of segmentation techniques on the performance of a CT texture-based lung nodule classification system. ECR 2016(poster no. B-0436).
6. Bondue B, Sherer F, Van Simaeys G, et al. PET/CT with 18F-FDG– and 18F-FBEM–Labeled Leukocytes for Metabolic Activity and Leukocyte Recruitment Monitoring in a Mouse Model of Pulmonary Fibrosis. Journal of Nuclear Medicine 2015;**56**(1):127-32.
7. Amara N, Goven D, Prost F, et al. NOX4/NADPH oxidase expression is increased in pulmonary fibroblasts from patients with idiopathic pulmonary fibrosis and mediates TGF-β1-induced fibroblast differentiation into myofibroblasts. Thorax 2010;**65**(8):733-38.
8. Matsusaka Y, Nakahara T, Takahashi K, et al. (18)F-FDG-labeled red blood cell PET for blood-pool imaging: preclinical evaluation in rats. EJNMMI Research 2017;**7**:19.

Figure legend

Figure 1. Textural analysis of PET [^{18}F]-FDG signals from normal lung in IPF patients and two control groups. Four examples showing significant differences in textural features: A) Laplacian of Gaussian (LoG) Uniformity with a 3.84mm filter ($p<0.0001$, IPF vs pooled controls), B) Laws Tex L5E5 mean ($p<.0001$), C) Laws Tex L5E5 std ($p<.0001$), D) First Order Statistics (FOS) std ($p<.0001$).

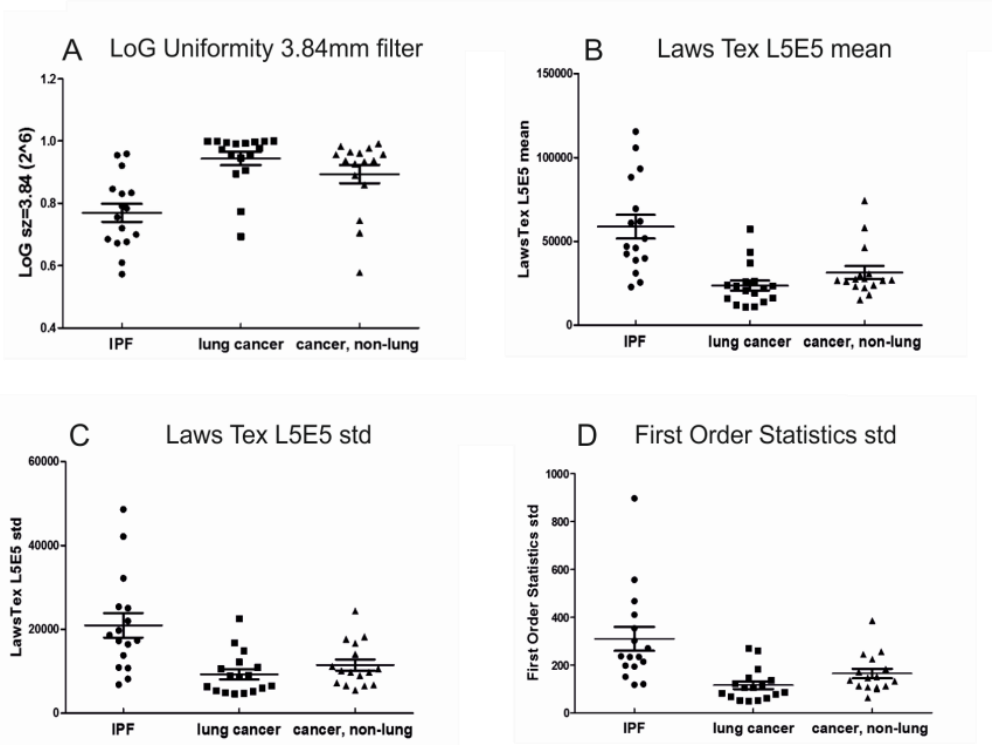
A
LoG Uniformity 3.84mm filter
LoG sz=3.84 (2^6)
1.2
1.0
0.8
0.6
0.4
IPF
lung cancer
cancer, non-lung
B
Laws Tex L5E5 mean
LawsTex L5E5 mean
150000
100000
50000
0
IPF
lung cancer
cancer, non-lung
C
Laws Tex L5E5 std
LawsTex L5E5 std
60000
40000
20000
0
IPF
lung cancer
cancer, non-lung
D
First Order Statistics std
First Order Statistics std
1000
800
600
400
200
0
IPF
lung cancer
cancer, non-lung

9.2 Appendix 2: Increased FDG uptake in areas of 'normal' lung in idiopathic pulmonary fibrosis

Thorax: first published as 10.1136/thoraxjnl-2016-209333.185 on 15 November 2016

1. SA Aliyu[1],
2. G Avery[2],
3. AH Morice[1],
4. SP Hart[1],
5. MG Crooks[2]

Background Idiopathic pulmonary fibrosis (IPF) has a variable disease course and we lack biomarkers that accurately predict prognosis or treatment response. Positron Emission Tomography-Computed Tomography (PET-CT) provides structural and functional information about the lung. A study of 25 IPF patients reported increased 18[F]-FDG uptake in areas of normal lung compared to controls.[1] If confirmed, this raises the possibility that PET-CT can identify 'microscopic fibrosis' with prognostic implications. We assess 18[F]-FDG uptake in areas of lung with normal CT appearance in a second IPF cohort.

Methods PET-CT scans undertaken for cancer staging at an interstitial lung disease tertiary referral centre were reviewed. IPF patients and controls without lung disease were identified. 18[F]-FDG uptake was assessed using manual region of interest (ROI) placement in areas of lung with normal CT appearance in IPF patients and controls. ROI were placed away from the mediastinum and concomitant tumours. 18[F]-FDG uptake within ROI was expressed as maximum and mean standardised uptake values (SUV) normalised using body weight. Mean Hounsfield Units (HU) were evaluated to assess for subtle differences in radiodensity within ROI. Data are presented as mean ± SD. Unpaired, 2-tailed T-tests were used to compare between group differences with a P value < 0.05 considered significant.

Results Forty-five subjects were included in this study (15 IPF and 30 controls). Lung cancer was the most common concomitant malignancy in both groups.

There was no difference in mean HU within ROI between IPF and controls (−719 ± 79 HU in IPF and −723 ± 147 HU in controls. P = 0.92). Areas of normal lung in IPF patients exhibited increased 18[F]-FDG uptake compared to controls measured by maximum SUV (0.98 ± 0.32 in IPF and 0.70 ± 0.20 in controls, P <0.01) and mean SUV (0.80 ± 0.29 in IPF and 0.57 ± 0.18 in controls, P < 0.01).

Conclusions We confirm that in IPF, areas of normal appearing lung exhibit increased 18[F]-FDG uptake compared with corresponding areas in controls. A longitudinal study is required to establish the relationship between 18[F]-FDG uptake, disease progression and treatment response.

Reference

1. Win T, Thomas BA, Lambrou T, *et al*. Areas of normal pulmonary parenchyma on HRCT exhibit increased FDG PET signal in IPF patients. *Eur J Nucl Med Mol Imaging* 2013;**41**(2):337–42.